

6-25-2010

Macro and nanocreep of self-consolidating concrete

Aaron Reinhardt

Follow this and additional works at: https://digitalrepository.unm.edu/ce_etds

Recommended Citation

Reinhardt, Aaron. "Macro and nanocreep of self-consolidating concrete." (2010). https://digitalrepository.unm.edu/ce_etds/28

This Thesis is brought to you for free and open access by the Engineering ETDs at UNM Digital Repository. It has been accepted for inclusion in Civil Engineering ETDs by an authorized administrator of UNM Digital Repository. For more information, please contact disc@unm.edu.

Aaron Reinhardt

Candidate

Civil Engineering

Department

This thesis is approved, and it is acceptable in quality and form for publication:

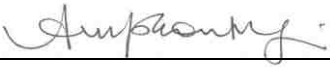
Approved by the Thesis Committee:



Dr. Mahmoud Reda Taha , Chairperson



Dr. Marwan Al-Haik



Dr. Arup Maji

**MACRO AND NANOSCALE CREEP OF SELF-CONSOLIDATING
CONCRETE**

BY

AARON REINHARDT

B.S. CIVIL ENGINEERING, UNIVERSITY OF NEW MEXICO, 2007

THESIS

Submitted in Partial Fulfillment of the
Requirements for the Degree of

Master of Science

Civil Engineering

The University of New Mexico
Albuquerque, New Mexico

May, 2010

©2010, Aaron Reinhardt

DEDICATION

I dedicate this work to my family, Dad, Mom, and Larrisa. Thank you for all your love and support. None of my accomplishments would be possible without you three in my life.

I hope I can continue to make you proud. I love each of you very much.

ACKNOWLEDGMENTS

First and foremost, I want to extend the upmost gratitude to my Master's thesis advisor and committee chair Dr. Mahmoud Reda Taha, without your encouragement and support completing this research would not have been possible. I would also like to thank you for pushing me to complete outstanding work, I am sure to use the skills I gained from this experience for the rest of my life. I want to thank my committee members Dr. Marwan Al-Haik and Dr. Arup Maji for their guidance and support throughout my work as a graduate student.

A special thank you to Kenny Martinez for helping me set up my macrocreep experiments, Mehran Tehrani for help with the nanoindentation experiments and Dr. Jung Joong Kim for helping me with the statistical deconvolution analysis presented in this thesis. I further want to recognize Andrew Garner and Eslam Soliman for their time spent helping me cast large volumes of concrete. Thank you Bernardo Farfan for your formatting guidance and wisdom, you saved me many hours of formatting this thesis.

Lastly, I want to acknowledge the Defence Threat Reduction Agency (DTRA) for funding my assistantship and this research.

**MACRO AND NANOSCALE CREEP OF SELF-CONSOLIDATING
CONCRETE**

BY

AARON REINHARDT

ABSTRACT OF THESIS

Submitted in Partial Fulfillment of the
Requirements for the Degree of

Master of Science

Civil Engineering

The University of New Mexico
Albuquerque, New Mexico

May, 2010

MACRO AND NANOSCALE CREEP OF SELF-CONSOLIDATING CONCRETE

by

Aaron Reinhardt

B.S., Civil Engineering, University of New Mexico, 2007

ABSTRACT

Self-consolidating concrete (SCC) is a concrete that can flow under its own weight, easily filling forms with highly congested reinforcement. Due to its fresh properties, there has been growing interest in using SCC in precast and prestressed applications. These applications are known to be sensitive to time-dependent phenomena such as creep and shrinkage. Therefore, it is important to understand the creep and shrinkage behavior of SCC compared with other types of concrete.

This research presents macro and nanoscale creep experiments used for a multiscale characterization of creep of SCC. Macrocreep experiments placed different SCC and normal vibrated concrete (NVC) mixes under sustained compressive and tensile stress to compare creep of SCC with NVC. Creep of SCC was compared with NVC that has similar water/binder ratio, volume of cement paste and ultimate compressive strength. Moreover, creep of SCC was compared to creep predicted using the ACI-209 and CEB-FIB MC90-99 models. Nanoscale creep experiments were performed using nanoindentation. Nanoindentations were made using both a Berkovich indenter tip and a spherical indenter tip. Creep compliance extracted at the nanoscale from cement pastes and concrete were used to compare nanomechanical properties and nanocreep of SCC and NVC.

Based on the experimental observations, it was found that SCC exhibits higher creep compliance than NVC at both length scales. To account for this, changes to the existing creep models are suggested. The high creep compliance of SCC should be considered during structural design of precast and prestressed concrete as SCC might show considerable prestress losses with time as a result of creep.

PUBLICATIONS AND PRESENTATIONS

The following publications and presentations have been produced during the course of study of this thesis:

Publications

Reinhardt, A.K., Adam, I.A., Reda Taha, M.M. “Total and Basic Creep and Shrinkage of Self-Consolidating Concrete”. *CD Proc. Third North American Conference on the Design and Use of Self-Consolidating Concrete 2008*, Chicago, IL

Reinhardt, A.K., Tehrani, M., Al-Haik, M., Reda Taha, M. M. “Nano Scale Characterization of Self-Consolidating Concrete”. *CD Proc. Third North American Conference on the Design and Use of Self-Consolidating Concrete 2008*, Chicago, IL

Reda Taha M. M., Al-Haik, M., Adam, I.A., Tehrani, M., Reinhardt, A. “Nano Versus Macro Creep Compliance of Concrete”. *Proc. of the Eighth International Conference on Creep, Shrinkage, and Durability of Concrete and Concrete Structures 2008*, Ise-Shima, Japan

Reinhardt, A.K., Taha, M.M.R., Al-Haik, and M., Tehrani, M., “Experimental and Numerical Investigation of Nanoindentation of Self-Consolidating Concrete”. *CD Proc. of the 2009 SEM Annual Conference on Experimental and Applied Mechanics 2009*, Albuquerque, NM

Reda Taha, M., Soliman, E., Sheyka, M., Reinhardt, A., and Al-Haik, M., “Fracture Toughness of Hydrated Cement Paste Using Nanoindentation”. *Proc. of the 7th International Conference on Fracture Mechanics of Concrete and Concrete Structures 2010*, Jeju, Korea

Reinhardt, A.K., Sheyka, M.P., Garner, A.P., Al-Haik, M., and Taha, M. R., “Experimental and Numerical Characterization of Two Phases in Concrete”, *International Journal of Mechanics and Materials in Design*, Vol. 4, No. 4, 2008, pp. 407–418

Reinhardt, A.K., Adam, I., Al-Haik, M., and Reda Taha, M.M., “Correlating Nano and Macro Creep Compliance of Cementitious Composites”, *Journal of Time Dependant Materials Special Publication: In Review*, Submitted August 2009.

Public Presentations

Comparative Creep Compliance of Two Types of Concrete using Nanoindentation, American Concrete Institute (ACI) Fall Convention, November 2009, New Orleans, LA

Nano-Creep of Cementitious Based Composites: An Experimental Investigation: Society of Experimental Mechanics (SEM) Conference, June 2009, Albuquerque, NM

Experimental and Numerical Nano-Characterization of Ultra High Performance Concrete: DTRA Poster Presentation, November 2008, Washington, D.C.

Nanoindentation of Cement-Based Composites, American Concrete Institute (ACI) Spring Convention, March 2008, Los Angeles, CA

Total and Basic Creep and Shrinkage of Self-Consolidating Concrete, Third North American Conference on the Design and Use of Self-Consolidating Concrete, March 2008, Chicago, IL

Nano Scale Characterization of Self-Consolidating Concrete, Third North American Conference on the Design and Use of Self-Consolidating Concrete, March 2008, Chicago, IL

CONTENTS

LIST OF FIGURES.....	xiv
LIST OF TABLES.....	xxi
CHAPTER 1. INTRODUCTION	1
1.1 NECESSITY OF CHARACTERIZING SELF-CONSOLIDATING CONCRETE	1
1.2 OBJECTIVE AND OVERVIEW OF THE RESEARCH	3
1.3 OUTLINE OF THE THESIS.....	4
CHAPTER 2. LITERATURE REVIEW	6
2.1 INTRODUCTION	6
2.2 SELF-CONSOLIDATING CONCRETE	7
2.3 CREEP.....	22
2.4 NANOSCALE CHARACTERIZATION OF CEMENTITIOUS MATERIALS	30
CHAPTER 3. MACROCREEP	35
3.1 INTRODUCTION	35
3.2 MATERIALS.....	36
3.3 COMPRESSION CREEP	38
3.3.1 MIX PROPORTIONS	38
3.3.2 EXPERIMENTAL METHODS.....	39
3.3.3 ANALYSIS OF EXPERIMENTAL DATA.....	54

3.3.4	COMPRESSION CREEP MODELING.....	56
3.3.5	RESULTS AND DISCUSSION.....	64
3.4	TENSION CREEP EXPERIMENTS	84
3.4.1	MATERIALS AND MIX PROPORTIONS.....	84
3.4.2	EXPERIMENTAL METHODS.....	84
3.4.3	ANALYSIS OF EXPERIMENTAL DATA.....	96
3.4.4	RESULTS AND DISCUSSION.....	97
CHAPTER 4. NANOSCALE CHARACTERIZATION OF SCC		105
4.1	INTRODUCTION	105
4.2	MATERIALS AND MIX PROPORTIONS.....	106
4.3	EXPERIMENTAL METHODS.....	108
4.3.1	SAMPLES.....	108
4.3.2	SAMPLE PREPARATION	108
4.3.3	NANOINDENTER.....	109
4.3.4	NANOINDENTATION EXPERIMENTS.....	111
4.4	ANALYSIS METHODS	122
4.4.1	BERKOVICH INDENTATION ANALYSIS	122
4.4.2	SPHERICAL INDENTATION ANALYSIS.....	127
4.4.3	STATISTICAL ANALYSIS	131
4.5	RESULTS AND DISCUSSION	133
4.5.1	NANOINDENTATION EXPERIMENTAL PROGRAM N1	133
4.5.2	NANOINDENTATION EXPERIMENTAL PROGRAM N2	141
4.5.3	NANOINDENTATION EXPERIMENTAL PROGRAM N3	159
4.5.4	NANOINDENTATION EXPERIMENTAL PROGRAM N4	164

CHAPTER 5. CONCLUSIONS	175
5.1 MACROSCALE CREEP OF SCC	176
5.1.1 CREEP UNDER COMPRESSIVE STRESSES	176
5.1.2 CREEP UNDER TENSILE STRESSES	177
5.2 NANOSCALE CHARACTERIZATION OF SCC.....	179
5.3 FUTURE WORK.....	181
REFERENCES	182

LIST OF FIGURES

Figure 2.1. (a) Mechanism of blockage (b) Mechanism of self-compactability.....	9
Figure 2.2. Set up of slump flow test showing required measurements	12
Figure 2.3. L-box test apparatus with three-rebar obstacle.....	15
Figure 2.4. General strain vs. time curve of a material exhibiting creep.....	23
Figure 2.5. Stress vs. time curve of concrete exhibiting total creep and shrinkage.....	26
Figure 2.6. Probability of indenting phases (HD and LD C-S-H) vs. number of indentations	33
Figure 3.1. Coarse and fine aggregate gradation curves.....	36
Figure 3.2. Mixing of fresh concrete	39
Figure 3.3. Measuring diameter of fresh SCC after slump flow test	41
Figure 3.4. Measuring height of horizontal section of fresh SCC after L-box test.....	42
Figure 3.5. Compression creep specimen form	43
Figure 3.6. Curing of Concrete Specimens.....	44
Figure 3.7. Sealing of sealed specimens with aluminium tape	45
Figure 3.8. Schematic of DEMEC disk placement.....	46
Figure 3.9. (a) Mechanical caliper used to gather creep and shrinkage displacements (b) Close up of sharp conical reading point placed into DEMEC disk.....	47
Figure 3.10. Schematic of compression creep specimen	50
Figure 3.11. (a) Force transfer schematic (b) Loading of creep specimens.....	51
Figure 3.12. (a) Storage of compression creep specimens (b) Storage of shrinkage specimens	53
Figure 3.13. General creep strain vs. time curve	56

Figure 3.14. Total shrinkage of SCC compression creep mixes.....	65
Figure 3.15. Shrinkage strains of all SCC and NVC compression creep mixes.....	66
Figure 3.16. Basic shrinkage strains of all SCC mixes used in compression creep experiments.....	67
Figure 3.17. Basic shrinkage curves for all compression creep mixes.....	68
Figure 3.18. Total creep compliance curves for NVC60, SCC40, SCC30, and SCC 20..	69
Figure 3.19. Ultimate creep compliance versus fly ash replacement.....	70
Figure 3.20. Total creep compliance curves for NVC30 and SCC30.....	71
Figure 3.21. Total creep compliance curves for NVC15 and SCC 20.....	72
Figure 3.22. Basic creep compliance curves for NVC60, SCC40, SCC30, and SCC 20.	73
Figure 3.23. Basic creep compliance curves for NVC30 and SCC30.....	74
Figure 3.24. Basic creep compliance curves for NVC15 and SCC20.....	74
Figure 3.25. Total creep compliance development rate at 28 days after loading.....	76
Figure 3.26. Basic creep compliance development rate at 28 days after loading.....	76
Figure 3.27. Prediction of creep coefficient of SCC40 using ACI-209 model.....	78
Figure 3.28. Prediction of creep coefficient of SCC30 using ACI-209 model.....	78
Figure 3.29. Prediction of creep coefficient of SCC20 using ACI-209 model.....	79
Figure 3.30. Prediction of creep coefficient of SCC40 using modified ACI-209 model.	80
Figure 3.31. Prediction of creep coefficient of SCC30 using modified ACI-209 model.	80
Figure 3.32. Prediction of creep coefficient of SCC20 using modified ACI-209 model.	81
Figure 3.33. CEB-FIP prediction model of creep coefficient for SCC40.....	82
Figure 3.34. CEB-FIP prediction model of creep coefficient for SCC30.....	83
Figure 3.35. CEB-FIP prediction model of creep coefficient for SCC20.....	83

Figure 3.36. Tension creep specimen forms	85
Figure 3.37. Curing of epoxy with applied pressure using c-clamps.....	86
Figure 3.38. Schematic of DEMEC disk placement for tension creep specimens	87
Figure 3.39. Direct tension test with fractured specimen after Kim et al.	89
Figure 3.40. Schematic drawing of tension creep experimental setup	91
Figure 3.41. Schematic of steel frame used in tension creep test	92
Figure 3.42. Attachment of tensile creep specimen to cantilever beam used to apply load	93
Figure 3.43. Steel chain anchored to the ground angle iron counter weights.....	94
Figure 3.44. Storage of tension test specimens.....	95
Figure 3.45. Shrinkage strains of SCC2.0, SCC1.5, NVC2.4, and NVC1.3	98
Figure 3.46. Weight loss percentage of SCC2.0, SCC1.5, NVC2.4, and NVC1.3.....	99
Figure 3.47. Basic shrinkage strains of SCC2.0, SCC1.5, NVC2.4, and NVC1.3	100
Figure 3.48. Total tension creep compliance of SCC2.0, SCC1.5, NVC2.4, and NVC1.3	101
Figure 3.49. Total tension creep compliance of SCC2.2 and NVC2.4.....	102
Figure 3.50. Total tension creep compliance of SCC1.5 and NVC1.3	102
Figure 3.51. Basic tension creep compliance of SCC1.5, NVC2.4, and NVC1.3	103
Figure 3.52. Basic tension creep compliance of SCC1.5, NVC2.4, and NVC1.3	104
Figure 4.1. Grinding of nanoindentation sample	109
Figure 4.2. Schematic of NanoTest TM 600 system	110
Figure 4.3. Schematic of indentations made on SCC30 and NVC00 cement pastes.....	112

Figure 4.4. Loading cycles for three loads used to indent cement pastes of SCC30 and NVC00.....	113
Figure 4.5. Schematic of indentations made on SCC30 and NVC00 cement pastes.....	114
Figure 4.6. Schematic of wet stage indentation experiments.....	115
Figure 4.7. Loading cycles for three loads used to indent cement pastes of SCC30 and NVC30.....	116
Figure 4.8. Schematic of concrete indentation made along a line using Berkovich indenter	117
Figure 4.9. (a) Schematic of concrete indentation made along a line using spherical indenter (b) Spacing between adjacent indentations	120
Figure 4.10. Loading cycle indentations made on SCC17 and UHPC165	121
Figure 4.11. Parameters of the Oliver and Pharr method	122
Figure 4.12. Schematic of parameters for spherical indenter	128
Figure 4.13. Comparison of maximum indentation depth between SCC30 and NVC00 at 1mN load	134
Figure 4.14 Comparison of hardness between SCC30 and NVC00 at 0.5 mN load	134
Figure 4.15. Comparison of reduced modulus between SCC30 and NVC00 at 0.5 mN load	136
Figure 4.16. Experimental and theoretical PDFs of LD and HD C-S-H for SCC30 and NVC00 at 0.5 mN load.....	138
Figure 4.17. Experimental and theoretical PDFs of LD and HD C-S-H for SCC30 and NVC00 at 0.5 mN load.....	138

Figure 4.18. Representative load-indentation curves of SCC30 and NVC30 LD and HD C-S-H indented at 0.5 mN load.....	139
Figure 4.19. Representative load-indentation curves of SCC30 and NVC30 LD and HD C-S-H indented at 1.0 mN load.....	140
Figure 4.20. Representative curves of indentations made on SCC30 at loads of 0.5 mN, 1.0 mN and 1.5 mN.....	141
Figure 4.21. Representative curves of indentations made on NVC30 at loads of 0.5 mN, 1.0 mN and 1.5 mN.....	141
Figure 4.22. Comparison of maximum indentation depth between SCC30 and NVC30 at 0.5mN load.....	142
Figure 4.23. Comparison of maximum indentation depth between SCC30 and NVC30 at 1.0 mN load.....	143
Figure 4.24. Comparison of maximum indentation depth between SCC30 and NVC30 at 1.5 mN load.....	143
Figure 4.25. Comparison of reduced modulus between SCC30 and NVC30 at 0.5 mN load.....	144
Figure 4.26. Comparison of reduced modulus between SCC30 and NVC30 at 1.0 mN load.....	145
Figure 4.27. Comparison of reduced modulus between SCC30 and NVC30 at 1.5 mN load.....	145
Figure 4.28. Zero depth reduced modulus for SCC30	147
Figure 4.29. Zero depth reduced modulus for NVC30	147
Figure 4.30. Comparison of hardness between SCC30 and NVC00 at 0.5 mN load	148

Figure 4.31. Comparison of hardness between SCC30 and NVC00 at 1.0 mN load	149
Figure 4.32. Comparison of hardness between SCC30 and NVC00 at 1.5 mN load	149
Figure 4.33. (a) SCC30 representative nano creep compliance curve (b) NVC30 representative nano creep compliance curve	151
Figure 4.34. Comparison of ultimate creep compliance between SCC30 and NVC30 at 0.5 mN load.....	152
Figure 4.35. Comparison of ultimate creep compliance between SCC30 and NVC30 at 1 mN load.....	152
Figure 4.36. Comparison of ultimate creep compliance between SCC30 and NVC30 at 1.5 mN load.....	153
Figure 4.37. Representative load indentation curves for SCC30 cement paste under wet and dry conditions at a load of 0.5 mN.....	155
Figure 4.38. (a) SCC30 dry representative nano creep compliance curve (b) NVC30 wet representative nano creep compliance curve	157
Figure 4.39. Comparison of ultimate creep compliance between SCC30 wet and dry indentations at 1mN load	158
Figure 4.40. Micrograph of SCC40 concrete sample showing the line of indentation...	160
Figure 4.41. Spatial distribution of hardness on SCC40 concrete mix.....	161
Figure 4.42. Spatial distribution of reduced modulus on SCC40 concrete mix	161
Figure 4.43. Load-indentation curves of aggregate, C-S-H, and ITZ for SCC40.....	162
Figure 4.44. Micrograph showing indented area of UHPC165	164
Figure 4.45. Micrograph showing indented are of SCC17	164
Figure 4.46. Representative load-indentation curves of UHPC165 and SCC17	165

Figure 4.47. Spatial distribution of reduced modulus of SCC17 and UHPC165	167
Figure 4.48. Comparison of reduced modulus between SCC17 and UHPC164	168
Figure 4.49. Comparison of maximum indentation depth between SCC17 and UHPC165	169
Figure 4.50. Comparison of maximum indentation depth between SCC17 and UHPC165	169
Figure 4.51. (a) SCC17 dry representative nano creep compliance curve (b) UHPC165 wet representative nano creep compliance curve.....	171
Figure 4.52. (a) Histogram of ultimate creep compliance observe along given line on SCC17 (b) Histogram of ultimate creep compliance observe along given line on UHPC165.....	172

LIST OF TABLES

Table 2.1. Reduced modulus and surface fractions of different cement paste phases reported by Constantinides et al. [10]	33
Table 2.2. Reduced modulus values reported by Mondal et al. [8]	34
Table 3.1. Physical properties of coarse and fine aggregate	37
Table 3.2. Mix proportions of concrete mixes used in compression experiments.....	38
Table 3.3. Properties of the cement paste for SCC40, SCC30, SCC20, NVC60, NVC30, and NVC15.....	39
Table 3.4. Fresh properties of concrete mixes used in compression experiments	41
Table 3.5. Mean and standard deviation of 7 and 28 days compressive strength and 7 day elastic modulus of SCC and NVC mixes	49
Table 3.6. Creep compliance development rate for compression creep experiments.....	75
Table 3.7. Mix proportions of concrete mixes used in tension experiments	84
Table 3.8. Properties of the cement paste for SCC2.2, SCC1.5, NVC2.4, and NVC1.3..	84
Table 3.9. Fresh properties of mixes used in tensile creep experiments.....	85
Table 3.10. Mean and standard deviation of 7 and 28 day compressive strength of tension creep specimens.....	88
Table 3.11. Mean and standard deviation of 7 and 28 day tensile strength	90
Table 4.1. Mix proportions and compressive strength of concrete mixes	107
Table 4.2. Mean, standard deviation of reduced modulus and surface fraction of LD and HD C-S-H for SCC30 and NVC00	139
Table 4.3. Nanomechanical properties for indented phases	162
Table 4.4. Nanomechanical properties of SCC17 and UHPC165	166
Table 4.5. Results from Hymostruc TM model	173

CHAPTER 1. INTRODUCTION

Concrete is the most widely used construction material in the world. Over the past few years researchers have made many innovations in concrete technology in the form of the development of new high performance concretes (HPC) and ultra high performance concretes (UHPC). One particular innovation in the field of concrete technology is the development of a HPC known as self-consolidating (or self-compacting) concrete (SCC). SCC is known for its ability to fill forms with highly congested reinforcement while flowing under its own weight without significant segregation. This reduces the efforts during concrete casting by eliminating the need for compaction and vibration, producing homogenous and non-honeycombed concrete in congested forms. Self-consolidation has made SCC an attractive alternative for precast and prestressed applications. The objective of this thesis is to characterize the time-dependent behavior of SCC. The following sections discuss the necessity and objective of this research.

1.1 NECESSITY OF CHARACTERIZING SELF-CONSOLIDATING CONCRETE

There has been a growing interest for the use of SCC in precast and prestressed concrete applications. These applications are known to be sensitive to time-dependent phenomena such as creep and shrinkage. Therefore, it is important to understand the creep and shrinkage behavior of SCC compared with other types of concrete. Existing literature reports present contradicting information about creep and shrinkage of SCC in comparison with normal vibrated concrete (NVC) [1-7]. Such conflicting information by researchers fails to provide clear information to the designers of structures involving the

use of SCC. There has been growing evidence of increased creep strains of SCC. If this proves to be true, designers will need to consider prestress losses to ensure safe designs. However, current available knowledge of these aspects of SCC is still limited and there are many opportunities for addressing these questions with further investigations and research. In this research investigation experiments to evaluate creep and shrinkage of SCC under sustained compressive and tensile stresses were developed.

Due to the difference between the microstructure of SCC and NVC, it was deemed necessary to investigate the mechanical properties at various length scales. Researchers believe that to improve macroscale properties, the material properties at the nanoscale and their correlation to macroscale properties must be understood [8]. Furthermore, an understanding of the mechanical behavior at the nanoscale and how different phases contribute to macroscale properties allows for more accurate modeling of the macroscale behavior. There has been a growing interest in the use of nanoindentation to extract mechanical properties of cementitious materials. Nanoindentation has been shown effective for extracting different nanomechanical properties of microstructural phases such as calcium silicate hydrate (C-S-H), calcium hydroxide (CH), and the interfacial transition zone (ITZ) [8-13]. Researchers have also shown that it is possible to extract the viscoelastic properties of materials through the use of nanoindentation [14].

Experimental investigations to extract viscoelastic behavior of concrete and cement paste have been produced for this investigation. Comparisons between macro and nanoscale observations are also reported.

1.2 OBJECTIVE AND OVERVIEW OF THE RESEARCH

The objective of this study is to investigate and characterize the long-term time-dependant behavior of SCC mixes at the macro and nanoscales. Moreover, time-dependant behavior of SCC is compared with time-dependant behavior of NVC. Two different sets of experiments were performed to investigate the long-term behavior of SCC at the macroscale. The first experiment involved measuring creep and shrinkage strains of specimens loaded with a sustained compressive stress for one year via prestressed compression creep frames. The second experiment utilized tension creep frames to measure creep and shrinkage strains of specimens subjected to sustained tensile stresses for 90 days.

Macrocreep tests were performed on different SCC and NVC mixes in both tension and compression. The choices of mixes were made to examine the different factors affecting creep of concrete. SCC and NVC mixes of similar water to cementitious material (binder) ratio and compressive strength were examined under compression creep. Furthermore, the compressive creep behavior of SCC specimens with varied amounts of fly ash was also examined. SCC and NVC mixes of similar tensile strength at time of loading were examined under sustained tensile stresses. The shrinkage strains of all specimens were also recorded, allowing for the comparison of SCC and NVC mixes and SCC mixes with variable amounts of fly ash. Compression creep results of SCC mixes were compared to estimated creep models provided by the American Concrete Institute (ACI) and the International Federation for Structural Concrete (CEB-FIP) [15]. This provided an indication of the need to update these models for predicting creep and shrinkage of SCC.

Nanoindentation tests were performed to characterize the behavior of concrete mixes at the nanoscale. Specimens were subjected to sustained loads during nanoindentation allowing for the extraction of the materials time-dependant response at the nanoscale. The nanoscale tests were performed on both cement paste and concrete specimens. The nanoindentation tests were broken up into four different test regiments. These regiments included comparing the response of SCC and NVC cement pastes at 7 days of age, SCC and NVC cement pastes of similar strength at 11 days under wet and dry conditions, an SCC sample at 150 days of age, and SCC and UHPC samples indented at 14 days of age. These different regiments provided insights on the response of the different concrete phases at the nanoscale. This characterization is important because obtaining the creep response of the different phases is necessary for development of constituent concrete models. Coupling these experiments with the macrocreep experiments allowed for examining trends and correlations between material behavior at the macro and nanoscales.

1.3 OUTLINE OF THE THESIS

Chapter 2 of this thesis presents the background information and the literature review. This includes an overview of SCC development, test methods to quantify SCC's rheological behavior, hardened properties of SCC and research findings on time dependant behavior of SCC. The literature review also provides background on research studies characterizing creep of concrete and the major factors affecting creep in concrete. Finally, Chapter 2 describes other research efforts for characterizing cementitious materials using nanoindentation.

Chapter 3 outlines the experiments used to characterize creep of SCC at the macroscale. This chapter describes materials and methods used for producing SCC and reference NVC mixes. The chapter also provides details on compression creep experiments comparing 3 SCC mixes and 3 NVC mixes of similar strength. The findings of these tests and possible factors influencing the findings are reported. The results of the creep tests performed on SCC specimens are also compared with the ACI and CEB-FIP models for creep of concrete. Chapter 3 finally outlines an effort to characterize tensile creep of 2 SCC mixes and 2 NVC mixes of similar tensile strength under sustained tensile stresses. The experimental findings and the possible factors affecting the results are described.

Chapter 4 outlines experiments used to characterize the behavior of SCC mixes using nanoindentation. This chapter begins by reporting on materials and mix proportions of SCC, NVC, and UHPC mixes used for comparison. The chapter then describes four different test regiments used to characterize cement pastes and concrete mixes at the nanoscale. The results of the nanoscale indentation experiments are also discussed at the end of Chapter 4.

Chapter 5 presents the conclusions of this study. The major trends found through the experiments are reported in two sections representing findings at the macro and nanoscales. Proposals for future work and extended research are presented at the end of Chapter 5.

CHAPTER 2. LITERATURE REVIEW

2.1 INTRODUCTION

In this chapter a literature review covering self-consolidating concrete (SCC), creep, and nanoscale characterization of cementitious materials is presented. The chapter starts by detailing the development of SCC, different methods used to produce SCC and how properties of SCC compared to normal vibrated concrete (NVC) mixes. The chapter then presents an overview of creep including: different creep mechanisms and different techniques used to model creep. This section ends with a discussion on creep of concrete under tensile stresses. The final section of this chapter presents an overview of nanoscale characterization of cementitious materials. This section details the significance of nanoscale research, an introduction to nanoindentation and a review of efforts towards nanoscale characterization. Finally, techniques for extracting time-dependent properties of materials at the nanoscale are described.

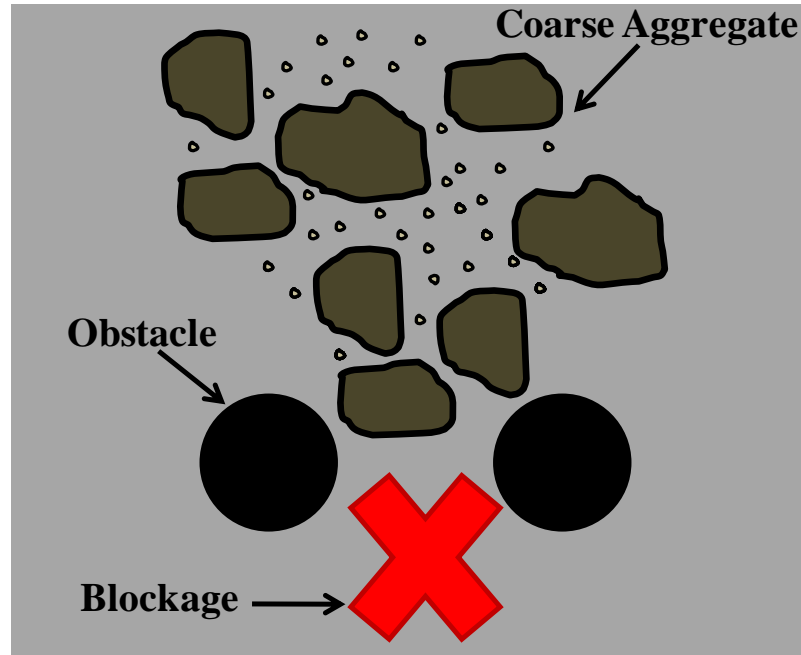
2.2 SELF-CONSOLIDATING CONCRETE

Self-consolidating concrete (SCC) also referenced as “self-compacting concrete” is a relatively new, innovative type of high performance concrete. Development of SCC dates back to the mid-1980s with the first fully developed prototype mix completed in 1988 in Japan by Ozawa et al [16]. Since then, SCC has gained significant momentum and has been used successfully in numerous bridges and structures [17]. SCC is defined by the ability to flow under its own weight without aggregate segregation or bleeding maintaining a constant moderate viscosity. This allows for placing SCC without any mechanical consolidation. Furthermore, SCC can flow through tight sections and areas with highly congested reinforcement filling all corners of formwork without any separation of its constituent materials. Therefore, the development of SCC represents one of the most outstanding advances in concrete technology.

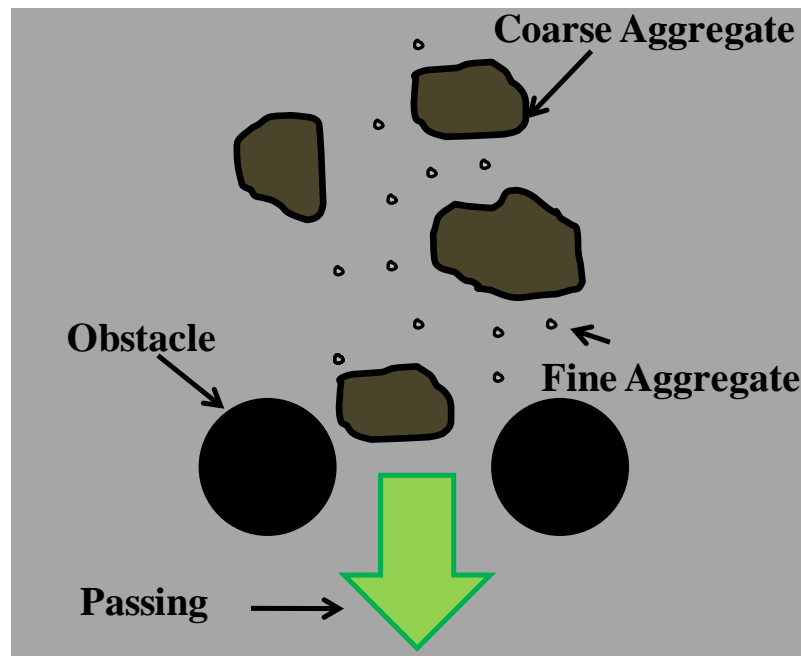
The cost of materials to produce SCC can be considerably high compared with normal concrete mixes, and this has hindered the large scale implementation of SCC. The increased material cost is attributed to the requirement of additional admixtures and/or increased amount of cementitious materials. Researchers have reported the cost of SCC mixes can range from 20% to 50% higher than normal concrete mixes [18-19]. To reduce SCC cost, researchers have proposed a “sandwich” construction method which involves casting structural elements in layers of SCC and normal concrete [20]. Although SCC has higher materials cost, this could be somewhat offset by reduction in construction cost because SCC has the ability to be set in place without mechanical consolidation. Some believe that with the reduction of construction costs the total cost of placing SCC will actually be up to 10% less than normal concrete. Other construction benefits of the use of

SCC include shorter construction periods, ensure the compaction in confined zones of the structure and the elimination of noise at construction sites due to mechanical vibrators [21].

SCC is typically produced using one of two different methods which can result in different hardened properties. The two types can be classified as powder type and viscosity modifying admixture (VMA) type. The first type uses superplasticizers, a low water to cementitious materials (binder) ratio and a limited aggregate content. Limiting the coarse aggregate content reduces the frequency of collisions and contact between coarse aggregate particles. A high frequency of contact and collisions results in increasing internal stress and friction when the concrete is deformed resulting in the blockage of aggregate particles near obstacles. By limiting the amount of fine aggregate present in the mix, the pressure transfer between coarse aggregate particles is reduced. A highly viscous paste also reduces incidents of increases in local internal stress when coarse aggregates approach obstacles. Thus, a very low water/binder ratio is needed to increase the viscosity of the cement paste. Keeping the water cementitious ratio low and the degree of deformity high requires the use of superplasticizers [21]. Figure 2.1 shows both the mechanisms of blockage and self-compactability of concretes flowing under their own weight. To compensate for less aggregate and to reduce cost, large amounts of cementitious fillers such as silica fume, fly ash, slag and limestone powder are typically used.



(a)



(b)

Figure 2.1. (a) Mechanism of blockage (b) Mechanism of self-compaction

The second type of SCC is developed by incorporating viscosity modifying agents (VMA) (also referenced as viscosity enhancing admixtures (VEA)). VMAs modify the concrete's cohesion, while allowing the mix to retain fluidity [22]. VMAs decrease the flow and kinetic energy of the concrete by increasing viscosity eliminating the need for having a low water/binder ratio. Adding more water exponentially reduces the viscosity making it advantageous to add VMAs. Since adding small amount of water drastically effects viscosity, it is sometimes difficult to separate the low water/binder mixes from mixes produced with VMA [23].

Khayat [24] showed that an optimal combination of superplasticizer and VMA produces a fluid mix with resistance to washout (segregation). It has been further shown that for SCC mixes, the incorporation of a VMA results in an increase in filling capacity while also resulting in the reduction of surface settlement and washout mass. Furthermore, Khayat reported that the usage of VMAs enhance the stability of highly flowable SCC. He showed that increasing the VMA content from 0.025% to 0.075% (by weight) in mixes containing silica fume and fly ash resulted in a substantial reduction in settlement even though both mixes had similar flowability. It has also been reported that concrete mixes with a high percentage of VMA showed up to a 61% increase in filling capacity [24].

SCC mixes are most defined by their fresh state properties. The fresh characteristics that define SCC mixes include:

- **Flowability** – ability of fresh concrete to flow under its own weight.
- **Viscosity** – the resistance to flow once fluidity has been initiated.
- **Passing Ability** – ability of the concrete to flow under its own weight through tightly spaced formwork and/or rebar without segregation or blocking.
- **Segregation Resistance** – ability of the concrete to sustain a homogenous composition in a fresh state.

Several different techniques to determine the behavior of SCC mixes in the fresh state have been developed. To measure flowability a slump flow test is commonly used. The slump flow test requires the use of the same equipment required for a typical slump test except it requires no consolidation (no rod compaction) [25]. The fresh concrete is filled to the top of the cone with no mechanical consolidation, while resting on a large moist base plate placed on level ground. The cone is then removed and the concrete is allowed to flow. The largest diameter and a diameter at a right angle to the largest diameter are then measured and the mean of these values is considered the slump flow. Slump flow is a strong measure of the concrete's flowability. Figure 2.2 shows a set up of a typical slump flow test with the two required measurements. This value describes the ability of the concrete to flow under unconstrained conditions [22, 26-27].

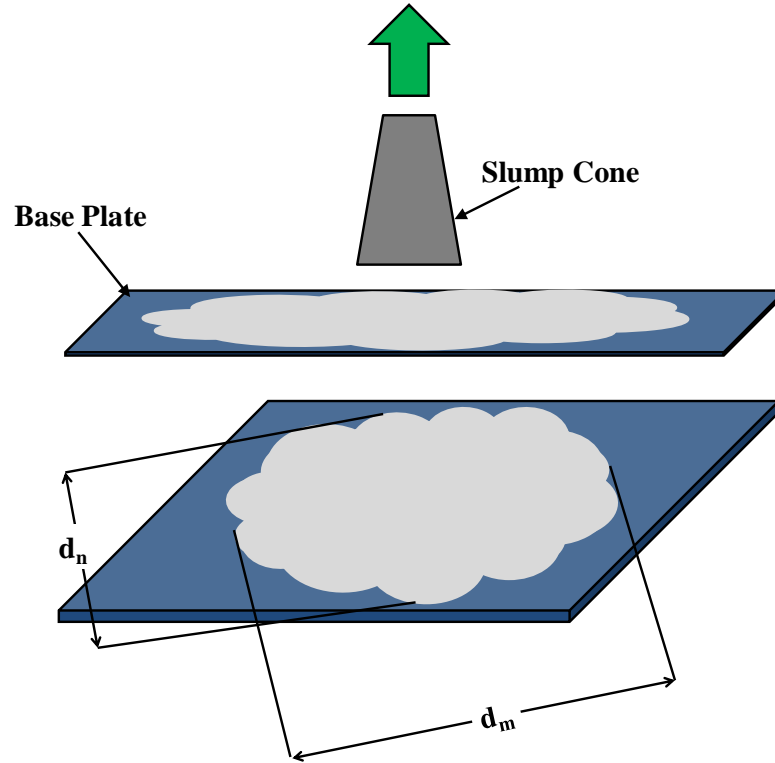


Figure 2.2. Set up of slump flow test showing required measurements

There are three classification ranges of slump flow: SF1, SF2 and SF3 [22]. The SF1 range of slump flow is between 550 mm and 650 mm. The typical applications of SF1 mixes include concrete structures with slight or no reinforcement, pump injecting systems and small enough sections to prevent horizontal flow. The next classification SF2 describes mixes with a slump flow in the range of 660 mm to 750 mm. This range works for most normal applications including walls and columns. Finally, the SF3 classification describes concrete mixes with a slump flow range between 760 mm and 850 mm. Concretes in this classification are used in situations with highly congested rebar or structures with complex shapes. Mixes of this classification typically perform better than SF2 classified mixes, especially in vertical applications where these mixes give a better

finish. However, segregation is much more difficult to control for these mix designs. For some special cases, mixes with a slump flow of over 850 mm are used, but in these situations special attention must be given to ensure the mixes do not exhibit too much segregation [22].

The next rheological property defining SCC mixes is viscosity. Common tests that are used to measure viscosity include the T_{500} flow time, funnel flow tests and the Orimet test. The T_{500} flow time test is performed in conjunction with the slump flow test. In this test a 500 mm circle is marked on the base plate used in the slump flow test. The slump cone is placed in the middle of the circle and filled with concrete as described in the slump flow test. The time that it takes for the flowing concrete to reach the circle is recorded as the T_{500} . This value is related to the viscosity because it describes the rate of flow. For example, low viscosity concretes will flow very quickly at the onset then stop flowing after only a short period of time. The T_{500} test results can be placed into two categories low (VS1) or high (VS2). The VS1 represents concretes with a flow time of less than two seconds and the VS2 represents concretes with a flow time greater than two seconds. VS1 mixes should work well for applications with highly congested reinforcement and usually result in the best surface finish; however, these mixes are highly prone to high segregation. The VS2 mixes have a higher resistance to segregation than VS1 mixes, but might result in producing a less than perfect surface finish [22].

Two different types of funnels are typically used for the funnel flow test including the o-shaped funnel and the v-shaped funnel. In a funnel flow test the concrete is filled to the top of the funnel and then a water tight hinged gate at the bottom of the funnel is opened releasing the concrete. The time required for the concrete to fully vacate the funnel is

then measured. The time it takes for the concrete to flow out of the funnel gives an indication to the level of its viscosity by correlating the flow rate to viscosity [22, 28-37]. The v-shaped funnel flow test can be categorized into high and low viscosity categories corresponding to the T_{500} classifications. The low viscosity classification or VF1 represents concretes with a funnel flow of less than 8 seconds. The high viscosity classification (VF2) represents v-funnel flow times within a range of 9 and 25 seconds [22].

Another defining fresh property of SCC is passability. Common tests to measure the passability of SCC include the J-ring, U-box, and L-box tests. The J-ring test must be used in conjunction with the Abram's cone or the Orimet test setup. In this test, a ring with variable spaced rebar simulating the reinforcement configuration is placed over the outside of the cone. The cone is raised and the concrete flows from the inside of the ring to the outside of the ring. The concrete spreads, with and without the presence of the ring, are measured and the difference between measurements represents the level of passability [22, 28, 33, 36, 38-39]. The U-box test involves constructing a u-shaped box divided by an obstacle fitted with a gate. Concrete is filled into one side of the box and the gate is released allowing the concrete to flow through the obstacle. The difference in height of the concrete on the two sides of the box represents the passability [28, 37-40].

The L-box test uses the same principles of the U-box test except the apparatus has an L-shape. The L-box test has two variations, one with a two-rebar obstacle and one with a three-rebar obstacle representing a highly congested situation. As in the U-box test, concrete is filled into the vertical section of the test apparatus and a gate is opened releasing the concrete through the rebar obstacle. A mean height of the concrete in the

vertical section (H1) and a mean height of the concrete in the horizontal section (H2) are found from measurements at three positions. The ratio of these two mean heights, H1 and H2, represent the measure of passability [22, 29, 33, 35-37, 39, 41-44]. Figure 2.3 shows a schematic of the L-box apparatus with a three bar obstacle representing a highly congested situation. The passability ratios are classified as either PA1 or PA2. PA1 represents concrete with an L-box ratio of 0.8 and above for tests performed with a two-rebar obstacles and PA2 represents concrete with a ratio of 0.8 and above for tests with a three-rebar obstacle .

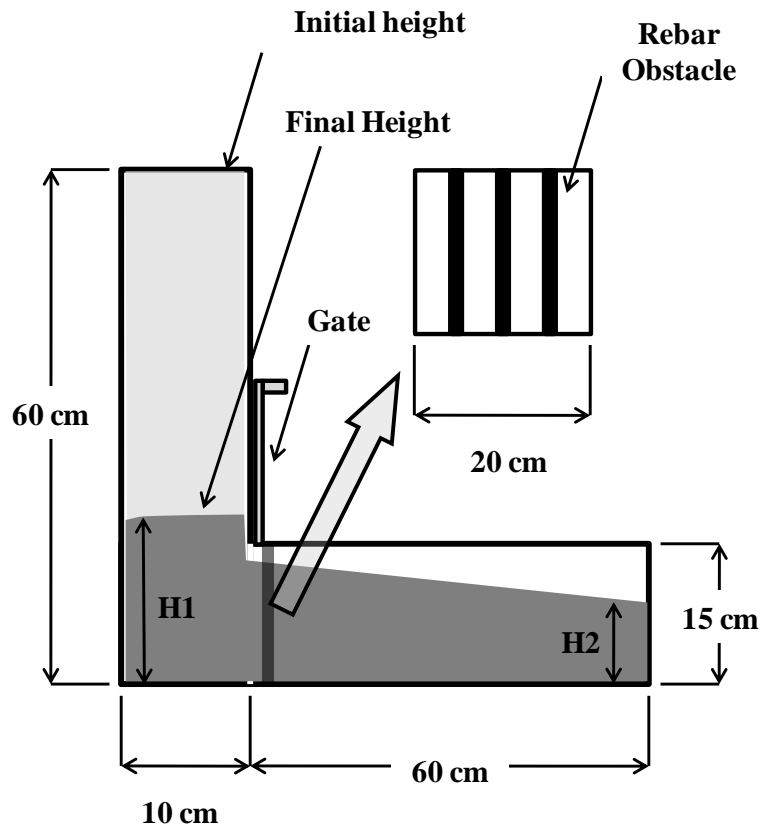


Figure 2.3. L-box test apparatus with three-rebar obstacle

Segregation resistance of the fresh concrete mixes can be measured through penetration tests, a settlement column test or a sieve segregation test. The sieve segregation test involves pouring concrete over a 5 mm sieve and measuring the amount of mortar passing through in a two minute period. The percentage of mortar passing through the sieve represents the measure of segregation resistance [37-38, 40]. The segregation resistance classes are SR1 for a segregation percentage less than or equal to 20% and SR2 for a segregation percentage less than or equal to 15%. SR1 is appropriate for applications with a confinement gap of less than 5 m and a flow distance of more than 80 mm. On the other hand, the SR2 mixes are applicable for situations with a confinement gap of more than 5 m and a flow distance of less than 80 mm [22].

Due to the vast differences in constituent materials and fresh properties SCC's hardened properties are typically expected to differ from those of NVC. SCC mixes also show high variations in hardened properties because of the wide range of material and mix proportions used for achieving SCC [45]. Moreover, SCC mixes are expected to have a different microstructure in comparison with NVC mixes. Quantitative analyses with optical and scanning electron microscopes (SEM) showed NVC to have a larger more porous interfacial transition zone (ITZ) compared with SCC. Furthermore, it was shown that SCC mixes have a lower oxygen permeability [46-47] and a lower sorptivity [47] in comparison with NVC mixes. One reason for the stronger ITZ and less porous microstructure might be the reduction in internal bleeding of fresh SCC [48].

The enhancement in SCC microstructure is reflected in improved properties such as strength, bond to steel reinforcement and durability. Researchers found an improvement in strength, particularly in powder type SCC mixes. It was shown that SCC mixes

containing limestone and chalk powder had a significant increase in compressive strength at early ages in comparison with NVC mixes with similar water to cementitious ratios [49]. Moreover, SCC showed an enhanced bond to steel reinforcement compared with NVC mixes [45, 50-52]. SCC mixes were also shown to be less vulnerable to top bar effect in comparison with NVC mixes [50-51].

Existing literature reports contradict information regarding creep and shrinkage of SCC compared with NVC [1-7, 53-56]. Such conflicting reports make it difficult for structural designers to accurately consider time-dependent deformations when SCC is used for prestressed concrete elements. Rols et al. [57] found that SCC mixes incorporating starch and precipitated silica as VMAs exhibited drying shrinkage strains 50% higher than NVC mixes with similar cement content. This was attributed to the fact that SCC contains a higher volume of mortar compared with typical NVC mixes. These findings showed the necessity to provide good field curing of SCC to prevent cracking [57]. Turcry and Loukili [58] also recommend careful field curing of SCC due to its vulnerability to early shrinkage cracks [58-59]. Researchers further confirmed shrinkage in SCC to increase as the volume of cement paste increased [56, 60]. Shrinkage of SCC was shown to be a function of the fly ash content.

Other researchers found shrinkage of SCC to be similar to shrinkage of NVC. Bouzoubaâ and Lachemi [61] investigated SCC mixes with a constant cementitious content and water/binder ratios ranging from 0.35 to 0.45. The mixes incorporated Class F fly ash as a partial replacement for cement (40%, 50%, and 60%). Concrete samples were cured in lime-saturated water for 7 days. Drying shrinkage of strain of these mixes was found not to exceed 600 microstrain after 224 days [61]. Furthermore, drying

shrinkage of these SCC mixes did not differ significantly from the drying shrinkage of a control air-entrained NVC mix containing no fly ash. Sahmaran et al. [42] showed SCC mixes with a high volume of low-lime and high-lime fly ash exhibited a lower shrinkage strain at 365 days in comparison with a control mix containing no fly ash. This was attributed to the matrix densification due to fly ash addition, which could have prevented internal moisture losses [42].

Shi and Wu [62] compared lightweight SCC mixes containing Class F fly ash and glass powder as filler materials used for enhancing fresh properties. Incorporating glass powder was found to increase the drying shrinkage strain in comparison with SCC mixes containing fly ash. Turkmen and Kantarci [63] reported a reduction in drying shrinkage when introducing expanded perlite aggregate into SCC mixes. Furthermore, as the moisture content of the perlite aggregate increased the drying shrinkage decreased.

Using a database including drying shrinkage test results 93 SCC mixes found in the literature, Fernandez-Gomez and Landsberger [64] evaluated the ability of popular shrinkage models (CEB-FIP 1990, EHE, ACI 209R, B3, and GL2000) to predict shrinkage of SCC. Using statistical methods it was found that the ACI 209R and B3 gave the best estimates for predicting shrinkage of SCC. The CEB-FIP 1990, EHE, and GL2000 typically underestimated shrinkage of SCC, however the models estimated shrinkage better for mixes with strengths less than 45MPa (6525psi). Heirman et al. [65] suggested a modification to the CEB-FIP MC-90 model to accurately predict drying shrinkage for limestone type SCC [65].

Similarly, researchers presented conflicting findings on creep of SCC [1-7, 55]. Persson [1] examined the creep of four SCC and four NVC mixes with water/binder ratios varying between 0.24 and 0.80. Specimens were loaded at stress to strength levels of 0.20, 0.40, 0.55, and 0.70 at ages which varied between 2 and 90 days using traditional spring loading devices. From these experiments it was found that the SCC mixes, both young and mature at the time loading, performed creep similar to that of NVC mixes when the strength was held constant. Furthermore, it was found that creep of both SCC and NVC mixes increased similarly when the specimens were loaded at a young age. Moreover, Persson [2] reported creep of a high-performance SCC to be similar to that of NVC.

Heirman et al. [65] investigated creep of powder type SCC mixes made with readily available materials incorporating a limestone powder as mineral filler. After 28 days of standard curing, specimens were loaded with creep frames incorporating a flat hydraulic jack to stress to strength levels ranging from 0.28 to 0.37. These test revealed that the SCC mixes experienced higher creep deformations in comparison with a control NVC mix. The CEB-FIP Model Code (MC-90) was shown to be able to predict SCC creep accurately. On the contrary, Sukumar et al. [66] reported SCC incorporating fly ash and VMA to experience less total creep strain in comparison with NVC specimens.

Seng and Shima [67] compared creep of SCC mixes with varying limestone filler contents to a control NVC mix. Specimens were air-cured at a relative humidity of $60 \pm 5\%$ for four days and were loaded at 40% of the compressive strength. While creep was shown to increase with increasing limestone content, creep of SCC was reported to be comparable to NVC. Similar findings were reported by Collepari et al. [68] for SCC

mixes containing limestone powder. However, Collepari et al. also reported SCC mix containing fly ash exhibited higher creep in comparison. This was attributed to unreacted fly ash, which was thought to be deformed upon specimen loading.

Lowke and Schießl [69] investigated the effect of powder content and VMAs on the creep and shrinkage of SCC mixes. Creep and shrinkage of SCC were not significantly affected by the VMAs used. It was shown that an increase in air voids due to adding air-entrainment increased creep and shrinkage of SCC significantly. It was also found that the SCC mixes with the lower limestone powder content exhibited higher creep in comparison with the SCC mixes containing high limestone content. The reduction of limestone powder also resulted in a coarser pore structure which appeared to favor creep and shrinkage [69].

Mazzotti and Ceccoli [70] investigated creep and shrinkage of four SCC mixes with different types and amounts of cement. A fixed dosage of a combine super plasticizer and VMA was used. Three mixes were cured in water for 2 days and stored in a relative humidity of 60% until the time of testing, while one mix was moist cured until one day before testing. Specimens were loaded at 7 and 28 days to 36% and 55% of compressive strength at time of loading. Shrinkage tests indicated that increasing the cement content resulted in significantly higher total shrinkage. The CEB-FIP MC90 creep model was reported to underestimate creep by about 30 to 60%. A modification factor based on cement to lime stone powder ratio was suggested for accurate creep modeling.

Maia et al. [71] investigated creep and shrinkage of SCC mixes containing high, medium and low paste contents. All three SCC mixes contained Portland cement,

limestone filler, superplasticizer, two types (fine and coarse) of siliceous sand and coarse crushed stone granite. It was reported that SCCs with low paste contents exhibited the highest creep when loaded at 24 hours. However, the different mixes did not exhibit a significant difference in creep from the control specimens when loaded at 3 and 7 days. Furthermore, shrinkage strains were shown to be directly correlated to the cement paste volume in SCC.

Wustholz and Reinhardt [72] examined the deformation behavior of three SCC mixes of different compressive strengths under direct tensile loading. These test revealed that SCC exposed to direct tensile stress can experience a phenomena coined stress-induced shrinkage. In fact, shrinkage strains observed on loaded specimens were higher than that of drying shrinkage specimens.

Turcry and Loukili [59] examined cracking tendency of SCC under restrained shrinkage. Restrained shrinkage ring tests revealed that SCC mixes exhibited an equivalent cracking tendency in comparison with NVC mixes of similar compressive strength. Moreover, Hwang and Khayat [73] investigated the effects of the inclusion of fibers in SCC mixes used for repair applications. Synthetic chopped fibers were shown able reduce the cracking potential of SCC regardless of fiber type. An increase of 0.25% in synthetic fiber volume resulted in a 40% increase in the time it took to develop restrained shrinkage cracks.

The current knowledge available on creep and shrinkage of SCC is still limited and there are many remaining questions that require further investigation and research.

2.3 CREEP

Viscoelasticity represents material stress and strain variations with time that remain within elastic limits. Examples of viscoelasticity include stress relaxation and elastic creep. Stress relaxation represents the decrease in elastic stress occurring in materials subjected to prolonged constant deformation. On the other hand, elastic creep represents deformation occurring over a time when a material is subjected to a constant stress within elastic limits. Materials such as concrete and masonry exhibit creep, while materials like steel experience stress relaxation.

Creep in concrete presents significant structural implications such as excessive structural deformations and stress redistributions that can result in cracking and loss of prestressing forces in prestressed concrete bridges. These issues have raised interest in modeling creep and its structural implications to ensure reliability of concrete structures [74-76]. Moreover, over the last sixty years research investigations have shown concrete to exhibit considerably high creep strains under sustained stresses [77-82]. It is important to note here that most of the interest of concrete creep has been within the framework of viscoelasticity. This is because of the fact that in almost all structural applications the sustained stress is less than the elastic limit of concrete. Therefore, we will limit our discussion to viscoelasticity and to creep within elastic limits. This may not be possible when addressing creep at the nanoscale due to the development of high stresses under nanoindentation loading.

Figure 2.4 shows a schematic of the general strain vs. time curve for a material exhibiting creep. At the onset of loading, the strain is primarily elastic but may exhibit some plasticity. After the initial load is applied, creep strain can be divided into three

distinct stages including primary creep, secondary creep and tertiary creep. Primary creep represents the range of creep where the rate of creep is high initially and then decreases with time. The material then reaches the secondary creep stage, where creep remains at a steady state. Depending on the material type and stress level, a third stage referred to as tertiary creep might be observed. In this stage an increase in strain rate leads to failure of the material. For normal workings of concrete, no distinction is made between the first two creep stages and the third stage is rarely observed as the sustained stresses are typically lower than the elastic limit [80].

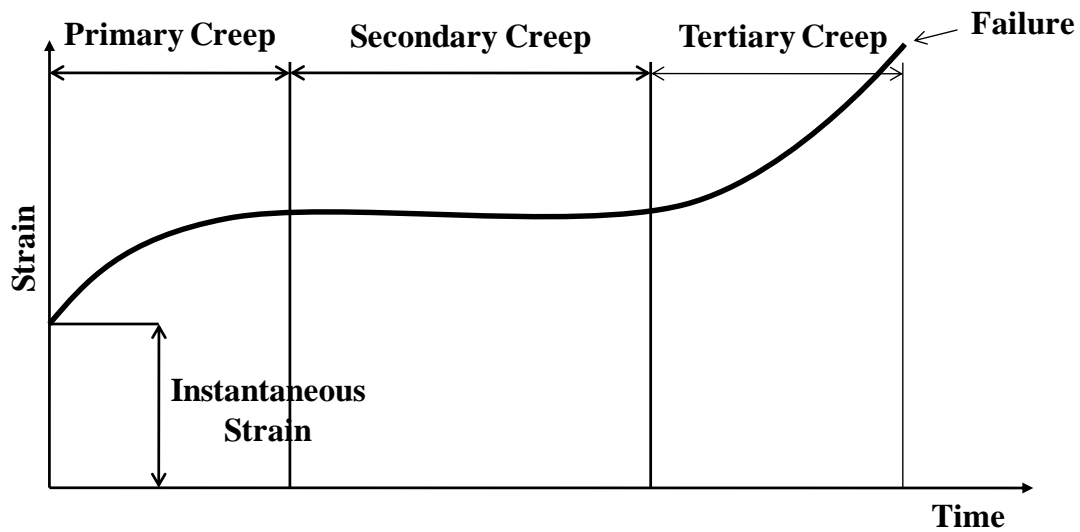


Figure 2.4. General strain vs. time curve of a material exhibiting creep

To model materials exhibiting creep behavior a number of rheological models were developed. These models include the Kelvin, Maxwell and Burgers models as well as many other models that strive to repeat the creep phenomena. Each model uses different mechanical devices to idealize the viscoelastic behaviour exhibited by materials. These

elements include the Hookean solid, Newtonian liquid and St. Venant body which represent a spring, dashpot, and friction element respectively. The major difference between the models involves assumptions for the relation between instant, delayed, and total deformations [80]. Equations (2.1), (2.2), and (2.3) represent the Kelvin, Maxwell, and Burgers models respectively.

$$\epsilon(t) = \frac{1}{k} \sigma(t) \quad (2.1)$$

$$\epsilon(t) = \frac{\sigma(t)}{k} (1 - e^{-\frac{k}{\eta} t}) \quad (2.2)$$

$$\epsilon(t) = \frac{\sigma(t)}{k_1} (1 - e^{-\frac{k_2}{\eta} t}) + \frac{1}{k_3} \sigma(t) \quad (2.3)$$

In each equation, $\epsilon(t)$ represents the strain at a given time t , k represents the stiffness of a spring, σ represents the applied stress, k_{1-3} coefficients represent spring constants and the η_{1-2} coefficients represent dashpot constants [80].

To fully understand creep one must first understand the underlying mechanics that affect creep. Several different theories have been developed to explain the underlying creep mechanisms in concrete. These theories include microcracking, viscoelastic theory, plastic theory, solid solution theory, seepage theory, etc. [80, 83]. For example, viscoelastic theory represents flow in a material and plastic theory deals with the region of plastic deformation.

Since concrete is a quasi-brittle material, an in-depth explanation of creep of brittle materials is necessary. For brittle materials, microcracking theory usually takes hold. The

type of crack typically considered in microcracking theory is the bond crack. These cracks are induced immediately after the application of load. Research has shown that the upper limit between the proportions between creep and stress lies within the region bond cracks begin to increase. When this limit is overcome, strains due to bond microcracking increase the creep at a higher rate. Microcracking only represents a portion of the deformation under sustained load and this portion is irreversible [80].

Typically the cement paste is considered the major contributing factor for why creep in concrete occurs. Creep in the cement paste occurs due to loss of physically absorbed water from calcium silicate hydrate (C-S-H). When a hydrated cement paste is exposed to ambient humidity conditions that are less than ideal (saturation) water escapes from C-S-H resulting in shrinkage strains. Likewise, when hydrated cement is exposed to constant stresses, water is forced from C-S-H and the paste shows creep strains (seepage theory). However, this water loss in the cement paste only explains a portion of creep of concrete. At sustained stress levels greater than 30 to 40 percent of ultimate stress, microcracks at the ITZ clearly contribute to the overall creep of concrete. This relates back to the explanation of the microcracking creep mechanism. Moreover, a delayed elastic response in the aggregate also adds to the total creep and is a function of the type of aggregate used in the concrete. For example, it is well documented that light weight aggregate increases concrete creep. The cement paste and aggregate are bonded by a weak phase (the ITZ), so when stresses are transferred from the paste to the aggregate a delayed elastic deformation occurs in the aggregate adding to the total creep deformation [83].

Due to different causes of creep in concrete two different types have creep have been realized including basic creep and drying creep. Basic creep is defined as creep of sealed

concrete specimens that cannot be attributed to loss of water due to drying. Drying creep is defined as the additional creep that can only be observed under less than saturated drying conditions. Drying creep is higher than basic creep because loss of water (drying shrinkage) leads to increased cracking which leads to higher creep deformations. Thus concrete specimens exposed to a sustained stress at less than saturated conditions are exposed to basic creep and shrinkage along with additional components due to drying creep and shrinkage [83]. Figure 2.5 shows a strain vs. time curve showing total creep and shrinkage. Research has shown difficulty in accurately separating the basic and drying creep components and further difficulty in separating drying creep from shrinkage strains [84].

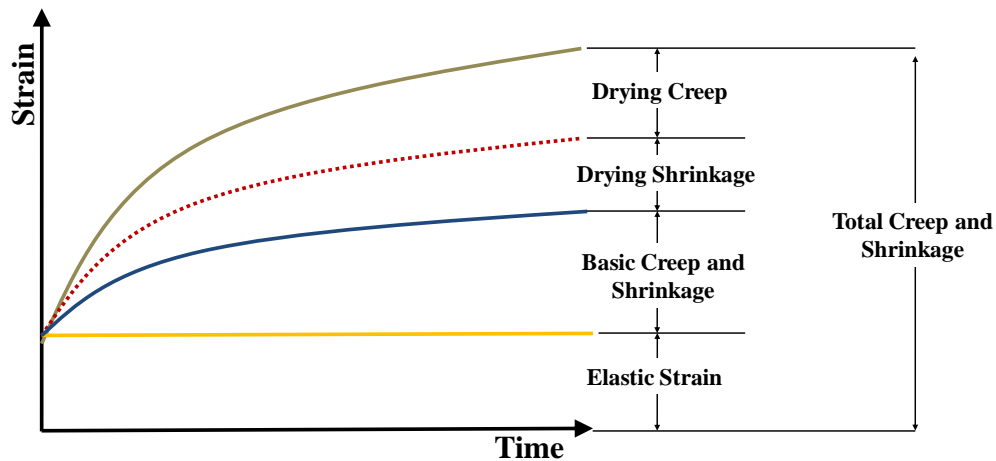


Figure 2.5. Stress vs. time curve of concrete exhibiting total creep and shrinkage

Many different factors simultaneously interact to influence creep in concrete. As mentioned earlier, the cement paste is a major contributing factor in creep of concrete, so the volume of the cement paste is typically considered a major influencing factor. Likewise, many attempts have been made to obtain expressions correlating creep strain

with the volume fraction of the cement paste. Another contributing factor to creep in concrete is the amount, shape, size and texture of the aggregate. While the amount of aggregate reduces the volume of the cement paste, the other characteristics affect the modulus of elasticity of the concrete. Changing the modulus of elasticity of the concrete directly relates to a change in the initial creep compliance. Moreover, time and relative humidity have a major influence on creep. Studies of various concrete mixes under different conditions have shown a similar time dependency. These various mixes exposed to the different conditions showed on average only 50% of a total 10 year creep strain realized after 100 days. Increases in relative humidity slow the effects of drying and also the effects of creep. Other factors influencing creep include geometry of the concrete element (or more specifically the volume to surface ratio), curing history, temperature of exposure, compressive strength and the applied stress to strength ratio [15, 83].

The American Concrete Institute (ACI) Committee 209 recognizes four different models for predicting creep and shrinkage of concrete. These models include the ACI-209R-92, Bažant-Baweja B3, CEB MC90-99, and GL2000 models [15]. For this work we will only consider the ACI-209R-92 and CEB MC90-99 models both which output creep coefficient ($\epsilon_c(t, t_0)$) not creep compliance. Creep coefficient represents a dimensionless multiplier where:

$$\epsilon_c(t, t_0) = \epsilon_{ci}(t_0) [1 + \mu(t, t_0)] \quad (2.4)$$

$$\epsilon_c(t, t_0) = \epsilon_{ci}(t_0) \mu(t, t_0) \quad (2.5)$$

In the equations above $\varepsilon(t_0)$ represents elastic strain, $\varepsilon(t, t_0)$ represents the total strain developed with time and $\varepsilon_{cr}(t, t_0)$ represents the creep strain developed with time. The ACI 209 model outputs a hyperbolic curve that trends towards an asymptotic ultimate value. At the most basic level, the shape of the curve is a factor of the age of concrete at the onset of drying and loading, curing method, ambient relative humidity, volume to surface ratio and cement type. Advantages of this model include simplicity and ease of fit by adjusting only the maximum creep value. Disadvantages of the model include a limited accuracy in comparison to other models and the fact that it is empirically based and does not model the creep phenomenon [15].

The CEB-FIP MC90-99 model is similar to the ACI model in that it outputs a hyperbolic curve that tends towards an ultimate creep value. However, unlike the ACI model this model has been developed for normal and high performance concretes. The major factors used for creep prediction include age of concrete at the onset of drying, loading age, mean compressive strength at 28 days, relative humidity, volume to surface ratio and cement type. Structural research on creep and shrinkage sensitive structures showed the CEB-FIP model to yield more accurate predictions than the ACI model [15]. Again this model is based on empirical data and not physical phenomena. Further discussions of both the ACI and CEB models are presented in the subsequent chapter.

Researchers have also shown the ability to model creep of cementitious composites using principles of linear viscoelasticity described by rheological models [85]. Success of linear viscoelasticity to estimate concrete creep can be attributed to the relatively low level of sustained stresses in concrete structures (typically lower than 40% of elastic limits) and the insignificance of temperature variation in real structures on creep behavior

[80]. However, for accurate prediction at early age where significant interaction between creep, shrinkage and temperature variation due to continuous cement hydration takes place, a comprehensive approach such as microprestress-solidification theory or crack plane frame analysis might be necessary to consider [86]. The significance of concrete shrinkage (both drying and self-desiccation) strains necessitates coupling creep and shrinkage measurements in cementitious composites [15, 87].

The majority of the research in creep of concrete is done under sustained compressive stresses. In fact, only a few researchers have examined creep of concrete under sustained direct tensile stresses [88-90]. However, the manner in which concrete behaves under tensile stresses is extremely important especially for applications with restrained shrinkage [88]. In the small amount of work that has been done, researchers showed concrete creep in tension to increase significantly under drying conditions with creep coefficients up to 6.2, which is drastically higher than creep coefficients in compression [88]. Furthermore, creep experiments performed by on SCC mixes under sustained tensile stress showed specimens loaded at 75% of their 28 day tensile strength failed at ages between 6 and 19 days [90]. Researchers have also commented on a phenomena known as “stress-induced” shrinkage, where specimens under direct tensile stresses show higher shrinkage than unloaded specimens. This is expected to occur because direct tensile stresses directly open crack surfaces causing increased water loss [90].

2.4 NANOSCALE CHARACTERIZATION OF CEMENTITIOUS MATERIALS

Nanotechnology has taken the scientific community by storm, allowing for many new and exciting advances in many different fields. Nanotechnology represents any technology where the dimensions and tolerances are within the range of 0.1 to 100 nm [91]. Many researchers believe that to improve macroscale properties, the material properties at the nanoscale and their correlation to the macroscale must be understood [8]. Advances in nanotechnology will hopefully allow for bottom up construction techniques where design starts at the nano or atomic scale. This could one day lead to extremely strong and durable structures that drastically reduce the cost of construction without sacrificing safety [91].

Significant effort has been reported in the last two decades in nanocharacterization of single phase materials such as ceramics (e.g. carbides) and metals such as aluminum [92]. Considerable work has also been devoted to probe polymer materials such as epoxy [93-94]. The significance of external environments due to thermal effects [95] and magnetic field effects [96] on material performance have also attracted researchers. Relatively limited work has been performed on composite materials with two phase composites where one phase material (e.g. epoxy) is strengthened by another phase material (e.g. carbon nanotubes). Special attention has been directed in such case to understand how the two-phase composite differs at the nanoscale from the single phase material. Efforts have also been directed to understand layered composites. It has been shown that the heterogeneity of the layered composite has a significant effect on stress evolution during nanoindentation [97].

There has been a growing interest in the use of nanoindentation to extract mechanical properties of materials. Nanoindentation essentially involves contacting a material with known surface properties to materials with unknown surface properties, while penetrating at a depth in the range of a few hundred nanometers. Indentation testing at this length scale is made possible by high precision depth sensing techniques. Typical nanoindenters used a depth transducer (parallel plate capacitor) to achieve these extremely small measurements. Generally, nanoindentation is used to gather properties such as reduced modulus and hardness. However, nanoindentation can also extract information on impact behaviour, energy absorption and time-dependant behavior. The different tips used for nanoindentation include spherical, conical, Vickers and Berkovich [98].

Considerable interest has been directed to apply principles of nanoindentation to cementitious composites including concrete and its many microstructural phases [8-13, 99-107]. In a pioneering research effort, Velez et al. [107] performed nanoindentation experiments on pure Portland cement clinker constituents reporting modulus and hardness values for C_3S , C_2S , C_3A , C_4AF , alite and belite. The authors further showed that the elastic moduli found through nanoindentation experiments were in close agreement with the elastic moduli found at the macroscale (by interpolation at zero porosity).

For quite some time now, researchers have realized different types of C-S-H (with varying densities) are formed during cement hydration [108]. Nanoindentation experiments have been directed to understand the microstructure of cement paste and have helped in recognizing two different types of C-S-H (high density (HD) and low density (LD)) [109]. Researchers believe that the microstructural phases such as calcium

hydroxide CH, HD and LD C-S-H have intrinsic material properties of hardness and modulus. Hence, the volume fractions of C-S-H and CH change from material to material (accounting for differences between mixes) but the values of hardness and stiffness remain the same [9].

In mechanically classifying HD and LD C-S-H Constantinides et al. [9] showed that as the number of indentations increase the probability of indenting each phase converges to the volume fraction of the individual phases (Figure 2.6). In order to identify different microstructural phases in cementitious composites, researchers perform many nanoindentations (up to 300) on the substrate (cement paste) using a Berkovich indenter tip. Then to determine the mechanical properties of the microstructural phases, researchers use statistical deconvolution analysis (further discussion presented in Section 4.4.3) [9] or mapping techniques [12] to distinguish between different microstructural phases. Table 2.1 presents the indentation modulus and surface fraction of pores, CH, HD C-S-H and LD C-S-H as reported by Constantinides et al.[10].

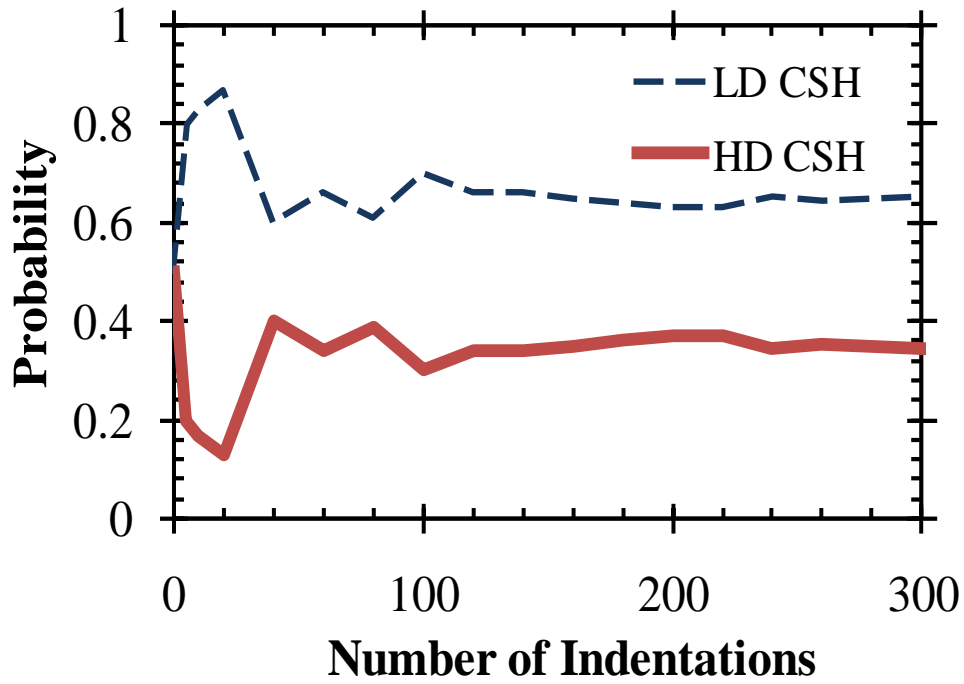


Figure 2.6. Probability of indenting phases (HD and LD C-S-H) vs. number of indentations

Table 2.1. Reduced modulus and surface fractions of different cement paste phases reported by Constantinides et al. [10]

Phase	E_r (GPa)	Surface Fraction
Pores	8.1 ± 1.70	6.0%
LD C-S-H	18.2 ± 4.19	51.0%
HD C-S-H	29.1 ± 4.07	27.0%
CH	40.3 ± 4.03	11.0%

With the use of a Hysitron Triboindenter, Mondal et al.[8] reported on the mechanical properties of unhydrated cement particles and three types of C-S-H including: high

stiffness (HS) , medium stiffness (MS) and low stiffness (LS). The reduced moduli (E_r) of the different phases investigated in this study are presented in Table 2.2. Mondal et al. [11] also reported a decrease in the reduced modulus of C-S-H as the distance from an unhydrated cement particle increased. In this work, indentations made in the ITZ showed the ITZ phases to have a mean reduced modulus of 18 GPa.

Table 2.2. Reduced modulus values reported by Mondal et al. [8]

Phase	E_r (GPa)
LS C-S-H	22.89 ± 0.76
MS C-S-H	31.16 ± 2.51
HS C-S-H	41.45 ± 1.75
Unhydrated cement particles	122.2 ± 7.85

Experiments on cement-based composites using nanoindentation have led to the realization of the distribution of reduced elastic modulus, hardness, fracture toughness and energy absorption of the different phases in cementitious composites [8, 11, 13, 99-100, 111]. However, little information has been reported on creep compliance of concrete and cement paste at the nanoscale [112-114]. Such information is crucial in characterizing the long-term performance of concrete. However, considerable efforts have been reported recently for analyzing creep behavior of other materials (e.g. polymers) at the nanoscale [14]. Three indentation tips are typically used for analyzing the creep behavior which include the flat-punch indenter [115], the spherical indenter [116] and the Berkovich indenter [96].

CHAPTER 3. MACROCREEP

3.1 INTRODUCTION

This chapter describes the macroscale creep experiments performed for this research. The chapter begins by detailing the specifications of the materials used in testing. Then a description of the compression creep experiments is presented, where self-consolidating concrete (SCC) and normal vibrated concrete (NVC) mixes are tested under sustained compressive stresses for 364 days. These experiments were used to compare the creep compliance of SCC and NVC mixes of similar cement paste volume and similar compressive strength at loading. This is followed by a description of the tension creep experiments performed on both SCC and NVC mixes. For tension creep, mixes with a similar direct tensile strength at loading were tested for 98 days to compare SCC and NVC creep behavior under direct tensile stresses.

3.2 MATERIALS

For all concrete mixes produced for macro-scale experiments ordinary Portland cement (ASTM Type I-II) and fly ash (ASTM Class F) were used as cementitious materials. Washed concrete sand with a fineness modulus of 2.71 and natural siliceous gravel with a nominal maximum size of 9.5 mm were used as fine and coarse aggregates, respectively. Gradation of both aggregates fell within ASTM grading requirements [117]. Figure 3.1 shows the gradation curves for the coarse and fine aggregates as well as minimum and maximum ASTM requirements. Moreover, Table 3.1 shows the unit weight, voids percentage, specific gravity and absorption percentage of the coarse and fine aggregates obtaining using tests performed according to ASTM Standards [118-119].

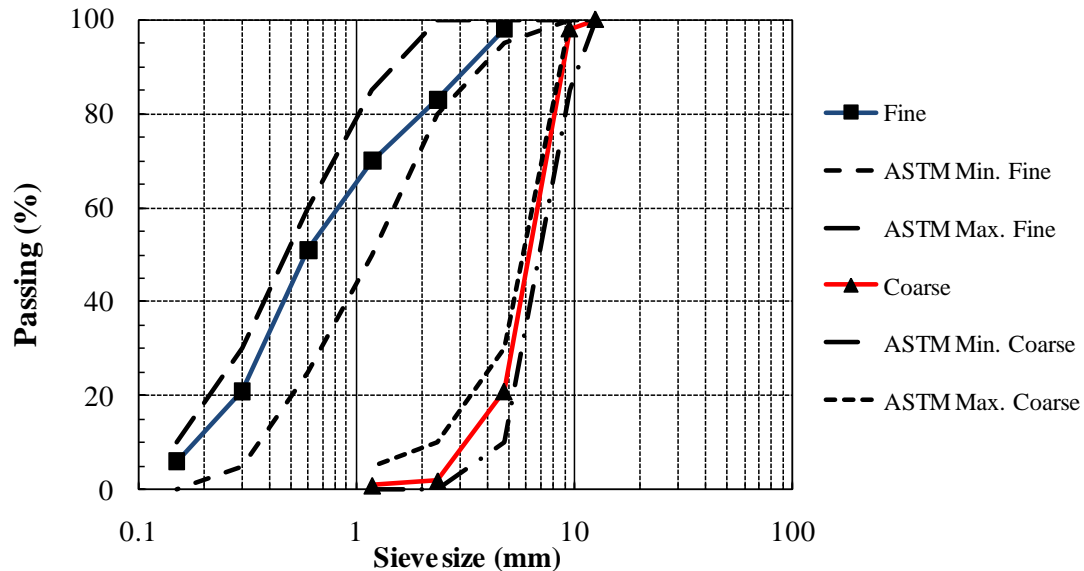


Figure 3.1. Coarse and fine aggregate gradation curves

Table 3.1. Physical properties of coarse and fine aggregate

	Unit weight kg/m³	Voids %	Specific gravity	Absorption %
Fine aggregate	1660	34.5	2.57	1.3
Coarse aggregate	1620	35.2	2.55	1.9

To enhance flowability and workability of fresh concrete mixes, a polycarboxylate based superplasticizer (Glenium3030NS™, BASF Inc) was incorporated in both NVC and SCC mixes. Due to the high amounts of superplasticizer required to produce SCC a viscosity modifying admixture (VMA362, BASF Inc.) was also added to control both segregation and bleeding of fresh SCC mixes. Due to the absence of a widely accepted mix proportioning methods for SCC, many trial batches guided by reported literature were created to verify properties of initial mix compositions [110, 120]. Adjustments were made to the final admixtures content as well as mixing sequence time based on the performance of fresh concrete produced in trial mixes. This enabled the production of flowable SCC mixes without the occurrence bleeding or segregation.

3.3 COMPRESSION CREEP

3.3.1 MIX PROPORTIONS

Three SCC mixes incorporating fly ash as a partial replacement for cement content were prepared. The fly ash contents were 20%, 40%, and 60%, by mass, of the total cementitious materials. Superplasticizer and viscosity modifying admixture (VMA) doses were adjusted in order to maintain the same amount of flowability for each of the three SCC mixes. The water/binder (cement plus fly ash) ratios of the SCC mixes were kept constant at 0.33 and the total cementitious content was kept at fixed at 450 kg/m^3 . In addition to the three SCC mixes, three NVC mixes were made for comparative purposes. One of the NVC mixes (NVC60) contained the same water/binder ratio at 0.33 and contained a total binder content of 420 kg/m^3 , within the range of the SCC mixes. The NVC30 and NVC15 mixes were designed to have a similar compressive strength at time loading as the SCC30 and SCC20 mixes. The mix proportions of the six concrete mixes are summarized in Table 3.2 and the properties of the cement paste of the different mixes are presented in Table 3.3.

Table 3.2. Mix proportions of concrete mixes used in compression experiments

	Weight per unit volume, kg/m^3					mL/m^3	
	Water	Cement	Fly Ash	Fine Aggregate	Coarse Aggregate	SP*	VMA**
SCC40	150	360	90	920	809	7650	4140
SCC30	150	270	180	902	794	4050	1800
SCC20	150	180	270	886	779	4500	1800
NVC60	139	420	0	637	1173	4050	0
NVC30	185	289	97	700	1143	1570	0
NVC15	192	236	79	700	1143	4700	0

Table 3.3. Properties of the cement paste for SCC40, SCC30, SCC20, NVC60, NVC30, and NVC15

	Fly Ash replacement (%)	Volume of Cement Paste (%)	Water Cement Ratio	Water Binder Ratio
SCC40	20	31	0.42	0.33
SCC30	40	32	0.56	0.33
SCC20	60	33	0.83	0.33
NVC60	0	29	0.33	0.33
NVC30	25	32	0.64	0.48
NVC15	33	36	0.81	0.61

3.3.2 EXPERIMENTAL METHODS

3.3.2.1 MIXING PROCEDURE



Figure 3.2. Mixing of fresh concrete

All concrete mixes were mixed according to a specific mixing procedure in a standard concrete mixer (Figure 3.2). This procedure included:

1. Mixing all dry materials for 30 seconds
2. Adding water and mixing for 2 minutes
3. Adding superplasticizer and mixing for 30 seconds
4. Adding VMA and mixing all materials (concrete) for 1 minute

**Total mixing time of 4 minutes

3.3.2.2 *FRESH PROPERTIES*

Upon completion of the mixing procedure, fresh concrete properties were evaluated. For NVC the standard slump tests were performed [25]. For SCC, concrete flowability and passability were determined using the slump flow and passing ability tests. Both tests were conducted according to European Guidelines for SCC [22]. The slump flow test was used to measure the flowability and the viscosity of SCC mixes. T_{500} represents the time it took the concrete to flow over a 500 mm diameter circle from the slump cone. The passability test was performed using a standard L-box. Table 3.4 shows the fresh properties of the six different concrete mixes.

Table 3.4. Fresh properties of concrete mixes used in compression experiments

	Slump flow (mm)	T ₅₀₀ time (s)	Passability (%)
SCC40	810	4.0	96
SCC30	710	4.0	93
SCC20	840	3	---
NVC60	150*	---	---
NVC30	250*	---	---
NVC15	245*	---	---

*Conventional Slump

It is worth mentioning that there were no visual signs of bleeding or segregation during testing of all SCC mixes in the fresh state. Moreover, aggregate particles were suspended within the mixes and were present all the way to the perimeter with no indication of mortar separation at the circumference of the concrete flow. Figure 3.3 and Figure 3.4 show testing of a fresh SCC's flowability and passability respectively.



Figure 3.3. Measuring diameter of fresh SCC after slump flow test



Figure 3.4. Measuring height of horizontal section of fresh SCC after L-box test

3.3.2.3 SPECIMENS AND SPECIMEN PREPARATION

After discerning the fresh properties the concrete was cast into a total of four compression creep (2) and shrinkage (2) prismatic specimens of 100 x 100 mm cross-section and 400 mm length. Fresh concrete was also cast into 25 cylinders, 100 mm diameter by 200 mm in length, used for obtaining concrete compressive strength with time. ASTM procedures were followed in preparing the concrete specimens [122]. Specimens for compression creep experiments were cast with a 25 mm inner diameter centrally oriented PVC pipe extruding 12 mm from the concrete top surface as shown in Figure 3.5.



Figure 3.5. Compression creep specimen form

All concrete specimens were allowed to harden for 24 hours before being removed from the molds. After being removed from the molds concrete specimens were placed in a temperature controlled (23 ± 2 °C) lime-saturated water curing bath until the day of loading following ASTM standards for curing concrete in the laboratory [122]. This is shown in Figure 3.6.



Figure 3.6. Curing of concrete specimens

At 11 days of age concrete creep specimens were removed from the curing bath and allowed to air dry until they reached a surface dry condition. Specimens used to determine basic creep and shrinkage were wrapped with a double layer of aluminum tape to prohibit the loss of moisture to the environment, as shown in Figure 3.7.



Figure 3.7. Sealing of sealed specimens with aluminium tape

Four DEMEC disks were glued to two opposite surfaces of creep and shrinkage specimens. The Aluminum tape of the sealed specimens was cut to allow placement of the DEMEC disks and resealed with epoxy after placement of the disks. The disks were placed with a placement rod which achieved an initial gauge length of 250 mm. Figure 3.8 shows a schematic of the placement of the DEMEC disks.

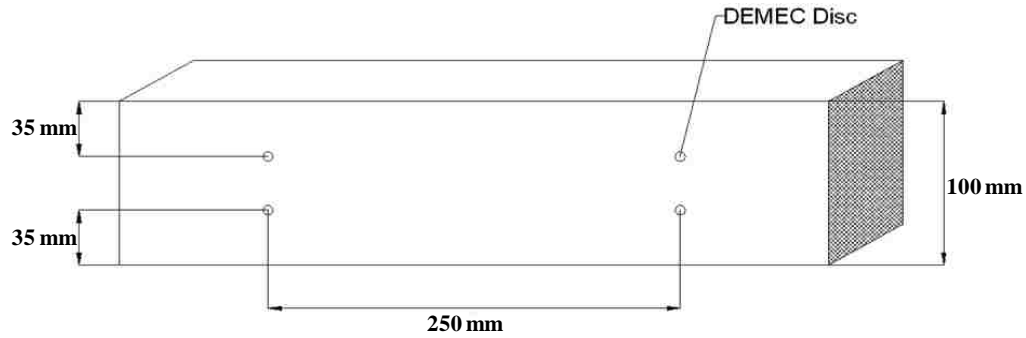


Figure 3.8. Schematic of DEMEC disk placement

3.3.2.4 MECHANICAL CALIPER

Readings were taken on all specimens using a mechanical caliper manufactured by Mayes Instruments, Co.. This caliper is fitted with sharp conical reading points that fit precisely into predrilled holes in the attached DEMEC disks. Figure 3.9 (a) shows the mechanical caliper used to obtain creep and shrinkage displacements. Figure 3.9 (b) shows a conical reading placed into a DEMEC disk. The mechanical caliper takes readings with respect to a reference bar with a gauge length of 250 mm. DEMEC disks were placed with a placement bar manufactured to precisely fit the reference bar. The gauge on the caliper reads from 0 to 2500 where each one increment represents 0.002 mm of displacement. This gives the caliper a range of 1.62 mm for compression displacement and 3.38 mm for tension displacements. The “zero” reading on the reference bar is 810 so length measurements using the caliper is represented as

$$L = (R - 810) * 0.0016 + 250 \quad (3.1)$$

R : reading taken on the mechanical caliper when inserted in mounted specimen DEMEC disks

L : distance between the DEMEC disks



(a)



(b)

Figure 3.9. (a) Mechanical caliper used to gather creep and shrinkage displacements
(b) Close up of sharp conical reading point placed into DEMEC disk

3.3.2.5 COMPRESSION EXPERIMENTS

The compressive strength of the concrete mixes was determined by testing three replicate cylinders at 7 and 28 days of age. Tests were performed using a standard compressive testing machine (Forney) at loading rates in accordance with ASTM C – 39 [123]. The compressive strength of the specimen was computed as:

$$f_c = \frac{P_c}{A} \quad (3.2)$$

P_c : Compressive failure load

A : Area of the concrete surface subjected to the compressive load ($A = 7854 \text{ mm}^2$ for 100 mm cylinder diameter)

The mean and standard deviation of the compressive strength of the different concrete was then determined.

Since it was not obtained through experiments the Young's modulus of elastic was calculated using the recommended equation (Equation (3.3)) from ACI [15].

$$E = 4734\sqrt{f'_c} \quad (3.3)$$

E : Young's modulus of elasticity

f'_c : Mean compressive strength of concrete cylinder

The 7 and 28 day mean compressive strength and 7 day computed elastic modulus of the six concrete mixes (3 SCC and 3 NVC) are shown in Table 3.5.

Table 3.5. Mean and standard deviation of 7 and 28 days compressive strength and 7 day elastic modulus of SCC and NVC mixes

	7 day Mean Compressive Strength, f'_c (MPa)	7 day Standard Deviation (MPa)	28 day Mean Compressive Strength, f'_c (MPa)	28 day Standard Deviation (MPa)	7 day Elastic Modulus (GPa)
SCC40	34.6	2.2	42.6	3.0	27.8
SCC30	13.9	2.0	28.9	8.4	17.7
SCC20	12.2	1.0	19.7	0.6	16.6
NVC60	47.9	1.4	60.8	4.5	32.8
NVC30	13.1	2.2	30.1	1.3	17.1
NVC15	11.2	3.4	14.6	0.6	15.8

3.3.2.6 COMPRESSION CREEP SETUP

Two 13 mm thick steel plates with a 25 mm diameter center bored holes were placed over the extruding PVC pipe on the specimen top surfaces. Then an 18 mm diameter threaded steel rod was passed through the PVC pipe. Another pair of 13 mm thick steel plates with 18 mm diameter holes were slid over the steel rod and attached with two loosely tightened locking nuts and one washer on each end. Figure 3.10 shows a schematic drawing of a compression creep concrete specimen used in this experimental investigation. The creep specimens were planned to be loaded in compression by tensioning the steel rods and locking them as in a concrete post-tensioning scheme.

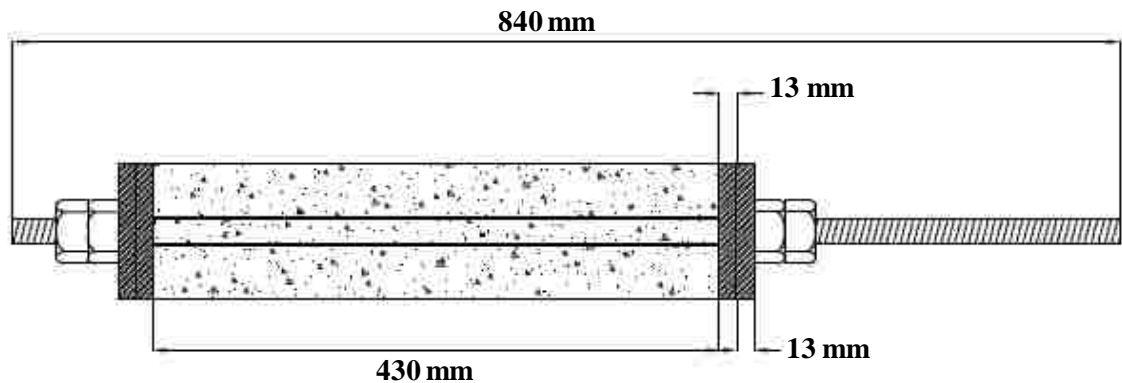


Figure 3.10. Schematic of compression creep specimen

The creep specimen was then placed in a Tinius Olsen Universal Testing Machine (UTM). Then the steel rod was pre-tensioned to the desired load as shown in Figure 3.11 (a). The load was held constant and the nuts were tightened securing the steel plates. The load was then released on the UTM transferring the load from the prestressing rod to the steel plates. This caused the steel plates to exert sustained compressive stresses on the concrete specimen. A force transfer schematic is shown in Figure 3.11 (b). All compression creep specimens were subjected to a nominal stress of 35% of the concrete compressive strength measured at 7 days of age. Immediately after loading, the initial displacements were recorded. Due to stress relaxation in the steel rod and creep of concrete all creep specimens were re-stressed to the original stress after 1, 3, 15, 25 and 51 days after initial loading and every 56 days thereafter. This procedure for producing creep specimens was used following Adam [124]. Two specimens of each concrete mix: wrapped and unwrapped were loaded to observe drying and basic creep.

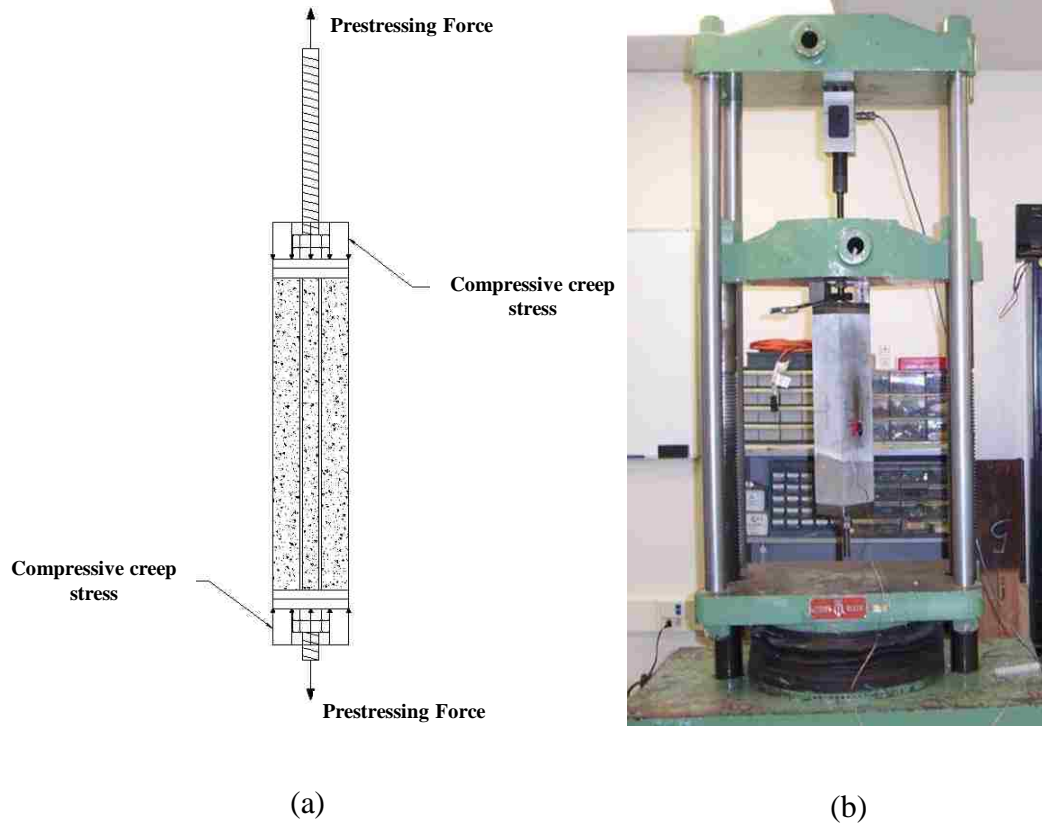


Figure 3.11. (a) Force transfer schematic (b) Loading of creep specimens

3.3.2.7 MEASUREMENTS AND SPECIMEN STORAGE

Specimens were kept in the laboratory which was automatically controlled to maintain constant temperature (23 ± 2 °C), while the relative humidity (RH) ranged from 20 to 75%. It is important to note that no thermal effects were considered in these experiments. Temperature variation within service conditions (similar to lab temperature here) of concrete proved to have insignificant effect on creep and shrinkage of concrete [80]. For each loaded (creep) specimen, an unloaded specimen was stored in the same environmental conditions for observing the shrinkage strains. Measurements of creep and shrinkage strains on sealed specimens were performed to enable separating the contribution of basic creep and shrinkage from the effect of drying creep and shrinkage,

respectively. Creep and shrinkage observations were recorded at 1, 3, 7, 10, 14, 21, 28, 35, and 42 days and every 14 days thereafter. Storage of creep and shrinkage samples is shown in Figure 3.12.



(a)



(b)

Figure 3.12. (a) Storage of compression creep specimens (b) Storage of shrinkage specimens

3.3.3 ANALYSIS OF EXPERIMENTAL DATA

Length measurements obtained from the mechanical caliper allowed for the calculation of displacement strain ϵ (Equation (3.4)).

$$\epsilon = \frac{L_t - L_{t_0}}{L_{t_0}} \quad (3.4)$$

L_t : length measurement with time

L_{t_0} : initial length measurement at time zero

Since, the elastic strain was recorded independently from the creep specimens upon loading L_{t_0} for creep specimens represents the measurement taken immediately after loading. Equations (3.5) to (3.8) present the strains measured on both unsealed and sealed specimens respectively. Equations (3.5) and (3.6) provide measurements in creep specimens while Equations (3.7) and (3.8) provide measurements on shrinkage specimens

$$\epsilon_{creep\ unsealed} = \frac{\Delta L_c}{L_{c_0}} + \frac{\Delta L_s}{L_{s_0}} \quad (3.5)$$

$$\epsilon_{creep\ sealed} = \frac{\Delta L_c}{L_{c_0}} + \frac{\Delta L_s}{L_{s_0}} \quad (3.6)$$

$$\epsilon_{shrinkage\ unsealed} = \frac{\Delta L_s}{L_{s_0}} + \frac{\Delta L_c}{L_{c_0}} \quad (3.7)$$

$$\epsilon_{shrinkage\ sealed} = \frac{\Delta L_s}{L_{s_0}} + \frac{\Delta L_c}{L_{c_0}} \quad (3.8)$$

$\epsilon_{creep\ unsealed}$: total strain obtained from unsealed creep specimens

$\varepsilon_{creep\ sealed}$: total strain obtained from sealed creep specimens

$\varepsilon_{shrinkage\ unsealed}$: total strain obtained from unsealed shrinkage specimens

$\varepsilon_{shrinkage\ sealed}$: total strain obtained from sealed shrinkage specimens

ε_{dc} : strain due to drying creep

ε_{bc} : strain due to basic creep

ε_{ds} : strain due to drying shrinkage

ε_{bs} : strain due to basic shrinkage

The use of the top four equations enabled separating all shrinkage and creep strain components. Once the drying and basic creep strains were separated, the creep coefficient $\phi(t, t_0)$ was calculated as the ratio between the creep strain developed with time and the elastic strain.

$$\phi(t, t_0) = \frac{\varepsilon_{cr}(t, t_0) - \varepsilon_{el}(t_0)}{\varepsilon_{el}(t_0)} \quad (3.9)$$

$\varepsilon(t, t_0)$: total strain observed with time (sum of elastic strain and creep strain)

$\varepsilon_{el}(t_0)$: elastic strain

Furthermore, basic and drying creep compliances were calculated from Equation 3.10.

$$J(t, t_0) = \frac{1}{E(t_0)} + \phi_{cr}(t, t_0) \quad (3.10)$$

$E(t_0)$: elastic modulus at time of loading

σ : applied stress

$\epsilon(t, t_0)$: time dependent creep strain

Figure 3.13 shows a general stress versus time curve highlighting the parameters used for the creep coefficient and creep compliance.

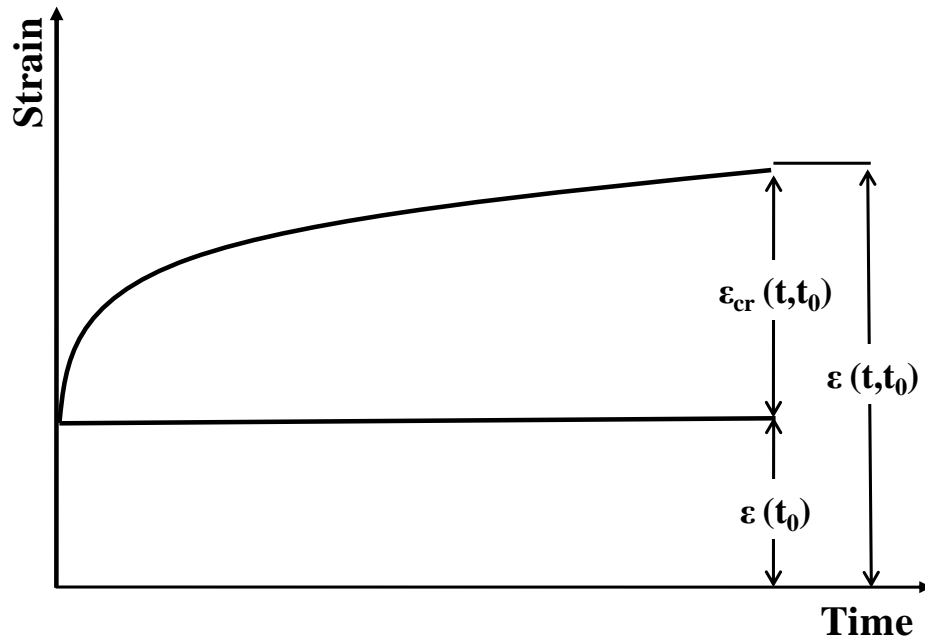


Figure 3.13. General creep strain vs. time curve

3.3.4 COMPRESSION CREEP MODELING

In an effort to relate the creep observed from SCC to that predicted by design codes for concrete's with similar strength we examine the observed creep to creep predicted by two design codes. These are the creep predictions, based on the American Concrete Institute

(ACI) model ACI 209R-2002 and that by the European code (known to be the most accurate prediction model) the CEB-FIP model MC-90-99. Our selection of the ACI-209 and CEB-FIP models is attributed to the fact that both models are the two most used models for being recommended by the ACI and for the CEB-FIP being reported to have a significantly low coefficient of variation (< 29%).

3.3.4.1 ACI 209R - 92 CREEP PREDICTION MODEL

The ACI 209R – 92 model predicts the creep coefficient, which is defined (Equation (3.9)) in the previous section. Equation (3.11) presents the ACI model for prediction of creep coefficient $\phi(t, t_0)$.

$$\phi(t, t_0) = \psi \frac{\phi_u}{d} \left(\frac{t - t_0}{t_0} \right)^u \quad (3.11)$$

t_0 : age of concrete at loading

t : time of measuring creep

ϕ_u : ultimate creep coefficient.

ψ and d : coefficients that depend on the shape and size of the member.

The shape and size of the member be completely taken accounted for by setting ψ to 1.0 and representing d by

$$d = 26.0 e^{-.42 \left(\frac{V}{S} \right)} \quad (3.12)$$

V/S : volume to surface ratio of the concrete member

For standard conditions the ACI, recommends the ultimate creep coefficient ϕ_u to be set at 2.35. For any other condition ACI recommends ϕ_u be modified by a series of correction factors and be replaced with Equation (3.13).

$$\phi_u = 2.35 \gamma_c \quad (3.13)$$

Where γ_c (defined in Equation (3.14)) is the cumulative product of a series of correction factors based on curing duration, relative humidity, volume to surface ratio, slump, ratio of fine to total aggregate and air content.

$$\gamma_c = \gamma_{c,t_0} \gamma_{c,RH} \gamma_{c,v_s} \gamma_{c,s} \gamma_{c,\psi} \gamma_{c,\alpha} \quad (3.14)$$

For time of load applications greater than 7 days γ_{c,t_0} for adjusting the ultimate creep is defined by

$$\gamma_{c,t_0} = 1.25 t_0^{-0.118} \quad (3.15)$$

t_0 : age of concrete loading in days

The factor to correct for relative humidity $\gamma_{c,RH}$ is defined as

$$\gamma_{c,RH} = 1.27 h^{-0.67} \quad (3.16)$$

h : relative humidity in decimals greater than 0.40 (ACI 209 recommends using a value of greater than 1 for a relative humidity less than 0.40)

To correct for differences in volume to surface ratio Equation (3.17) is used.

$$\gamma_{c,vs} = 1.13e^{-0.0213(V/S)} \quad (3.17)$$

V/S : Volume to surface ratio represented in mm

The correction factor for the slump $\gamma_{c,s}$ is define as

$$\gamma_{c,s} = 0.82e^{-0.00264s} \quad (3.18)$$

s : slump of the concrete represented in mm

The ratio of fine aggregate to total aggregate is corrected for with $\gamma_{c,\omega}$ which is defined by Equation (3.19).

$$\gamma_{c,\omega} = 0.88e^{-0.0024\omega} \quad (3.19)$$

ω : the ratio of fine aggregate to total aggregate as a percentage

Lastly, Equation (3.20) shows the air content factor $\gamma_{c,\alpha}$

$$\gamma_{c,\alpha} = 0.46e^{-0.09\alpha} \quad (3.20)$$

α : air content as a percentage

There is clearly a need to modify the ACI-209 model in order to predict creep of SCC due to the model's dependence on knowing the concrete's slump (Equation (3.18)). To

predict the creep of SCC mixes using fly ash replacement, a coefficient based on the fly ash replacement percentage is proposed. We did not choose slump flow because different SCC mixes with the same slump flow can show vastly different compressive strength and creep. It should be noted here that many common parameters of the concrete mixes could be used (i.e. admixture content, water/binder ratio, volume of cement paste, etc.) however, in our case fly ash replacement had the most significant effect on compressive strength. This coefficient was found by fitting the ACI-209 model to our experimental data through optimizing the coefficient to produce the lowest root mean squared error (RMSE) between the predicted model's and the experiment's ultimate creep compliance. A relationship was then found using least squares method to relate each the modified slump coefficient found for each concrete to that concrete's fly ash replacement percentage. The result is a coefficient to replace the slump coefficient for SCC mixes. This new coefficient is defined as

$$k_{s, SCC} = \left(\frac{0.0006F^2 + 0.0015F + 0.0009}{40 + F} \right)^{0.5} \quad (3.21)$$

F : fly ash replacement ratio represented as a percentage

3.3.4.2 CEB MC90 – 99 CREEP PREDICTION MODEL

The CEB MC90 – 99 Creep model also predicts creep of concrete in terms of creep coefficient. This model does not predict creep coefficient for instances where the stress to mean concrete strength at the time of loading is more than 40%. For this model the creep coefficient $\phi_{28}(t, t_0)$ can be calculated from Equation (3.22)

$$(3.22)$$

$$\phi_{28}(t, t_o) \beta_c(t - t_o)$$

where ϕ_o is the notional creep coefficient and $\beta_c(t - t_o)$ is a coefficient that describes the development of creep with time. The notional creep coefficient ϕ_o can be determined from Equations (3.23) to (3.28).

$$\phi_o = k_{RH}(h) f_{cm28} \quad (3.23)$$

$$k_{RH}(h) = \frac{1 + h/h_o}{\sqrt[3]{0.1 [(V/S)/(V/S)_o]}} \quad (3.24)$$

$$f_{cm28} = \frac{5.3}{\sqrt{f_{cm28}/f_{cmo}}} \quad (3.25)$$

$$\beta_o = \frac{1}{0.1 (t_o/t_1)^{0.2}} \quad (3.26)$$

$$k_1 = \frac{0.5 f_{cmo}^{0.7}}{f_{cm28}} \quad (3.27)$$

$$k_2 = \frac{0.5 f_{cmo}^{0.2}}{f_{cm28}} \quad (3.28)$$

f_{cm28} : mean compressive strength of standard concrete cube at 28 days represented in MPa.

f_{cmo} : 10 MPa

h : relative humidity of the ambient environment in decimals

h_o : 1

V/S : Volume to surface ratio represented in mm

$(V/S)_o$: 50 mm

t_1 : 1 day

t_o : Age of concrete at loading adjusted by Equation (3.29)

$$t_o = t_{o,T} \left[\frac{9}{(t_{o,T}/t_{1,T})^{1.2}} \right] \quad (3.29)$$

$t_{o,T}$: Concrete age at loading for $T = 20^\circ\text{C}$ (needs to be adjusted for other temperatures)

$t_{1,T}$: 1 day

α : Coefficient depending on cement type ($\alpha = 0$ for normal cement)

The coefficient $\beta_c(t - t_o)$ that describes the development of creep with time may be determined from Equations (3.30) to (3.32).

$$\beta_c(t - t_o) = \left[\frac{(t - t_o)/t_1}{(t_{o,T} - t_o)/t_1} \right]^{0.3} \quad (3.30)$$

$$\beta_H = 50 \left[1.2 \left(\frac{h}{h_o} \right)^{18} \right] \left[\frac{V/S}{(V/S)_o} \right]^{0.3} \quad (3.31)$$

$$f_{cm28} = \frac{.5 f_{cmo}}{f_{cm28}^{0.5}} \quad (3.32)$$

$(t - t_0)$: duration of the applied load (days)

t_1 : 1day

V/S : volume to surface ratio represented in mm

$(V/S)_o$: 50 mm.

h : relative humidity of the ambient environment in decimals

h_o : 1

f_{cm28} : mean compressive strength of standard concrete cube at 28 days measured in MPa

f_{cmo} : 10 MPa

Since the compressive strength was obtained by testing cylinders f_{cm28} was calculated using Equation (3.33).

$$f_{cm28} = f'_c \quad MPa \quad (3.33)$$

f'_c : compressive strength of standard cylinder at 28 days of age

To compare the predicted results of the ACI and CEB-FIB creep prediction models, the root mean square error (*RMSE*) was found between the experimental and predicted results. *RMSE* is defined in Equation (3.34).

$$RMSE = \sqrt{\frac{\sum_{i=1}^N (EXP(i) - PRED(i))^2}{N}} \quad (3.34)$$

$EXP(i)$: i^{th} experimental data point

$PRED(i)$: i^{th} predicted (ACI or CEB-FIB model) data point

N : Number of data points

3.3.5 RESULTS AND DISCUSSION

3.3.5.1 COMPRESSION CREEP AND SHRINKAGE EXPERIMENTAL RESULTS

Figure 3.14 shows the total shrinkage curves for the SCC mixes. This figure shows that SCC30 and SCC40 displayed similar shrinkage strains over the 364 day time period. However, SCC20 had a significantly higher shrinkage strain than the other two SCC mixes. It is noted that the SCC20 mix had the highest percentage of fly ash replacement at 60% and the highest volume percentage of cement paste at 33%. Therefore, it can be generally concluded that significantly replacing cement with fly ash increases the volume of cement pasted resulting in a higher shrinkage strain of SCC. This agrees with previous reports in the literature on the significance of cement paste volume on the developed shrinkage strain.

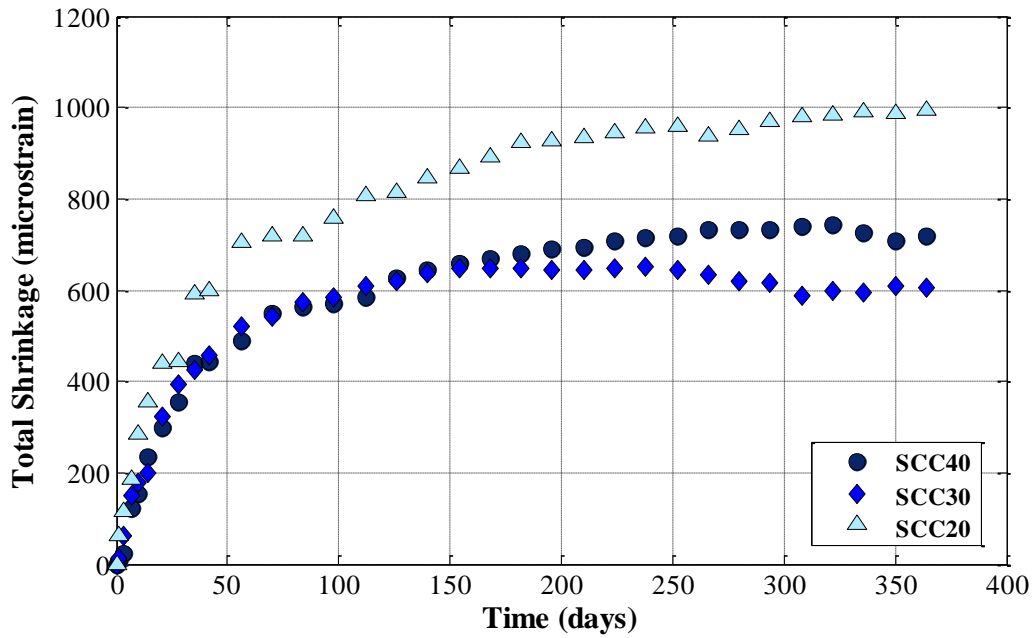


Figure 3.14. Total shrinkage of SCC compression creep mixes

Figure 3.15 shows shrinkage strains with time for all the mixes examined in the compression creep portion of this investigation. This figure shows that for the most part the SCC mixes displayed relatively similar shrinkage performances when compared with the NVC mixes. Again it is shown here that increasing the fly percentage to 60% caused the shrinkage of SCC20 to be significantly higher than the other concrete mixes.

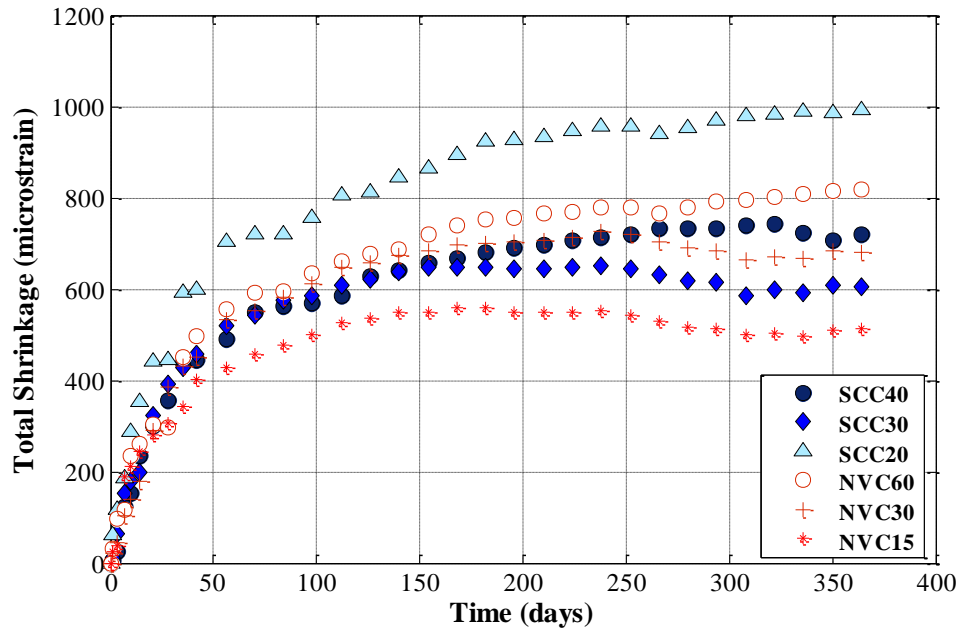


Figure 3.15. Shrinkage strains of all SCC and NVC compression creep mixes

Figure 3.16 presents the development of basic shrinkage strain (measured on sealed specimens) over time of the tested SCC mixes. Basic shrinkage of SCC40 with 20% fly ash is higher than that of the SCC mixes with 40% and 60% fly ash. This might be attributed to the significant amount of cement in the SCC40 mix. It is well known that basic shrinkage is due to the absence of water necessary to hydrate all cementitious materials. This is more pronounced with mixes with high cement content. It appears that the significance of cement on basic shrinkage (autogenous) is higher than fly ash, which might be attributed to the higher reactivity of cement compared with fly ash. The discrepancy between SCC30 and SCC20 cannot be explained using the above argument and might be related to experimental variation.

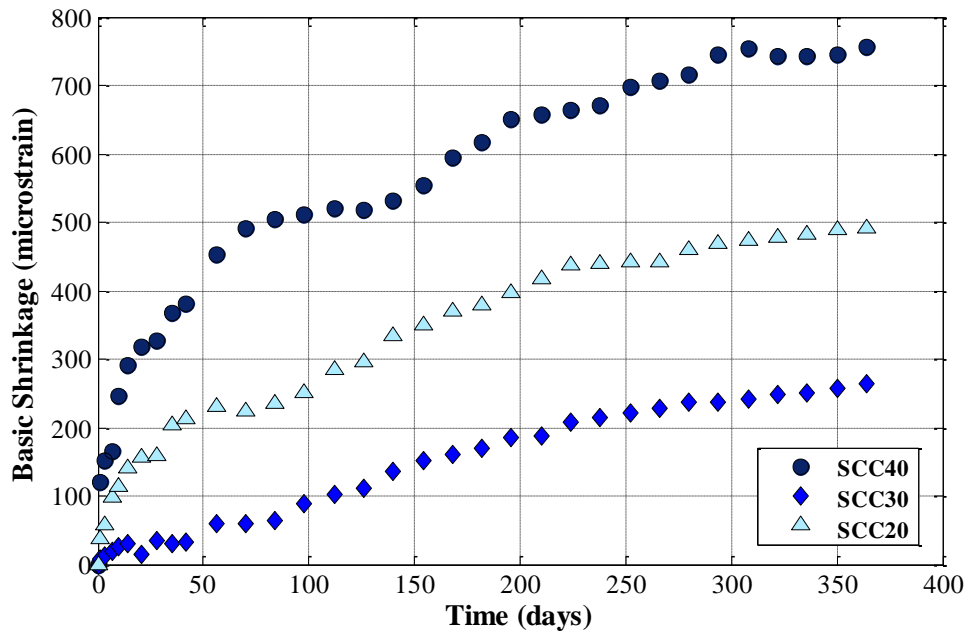


Figure 3.16. Basic shrinkage strains of all SCC mixes used in compression creep experiments

Figure 3.17 shows the development of basic shrinkage for all of the mixes. This figure again shows that increasing the fly ash content generally decreased the amount of basic shrinkage. This was observed in the NVC mixes with NVC60 having higher basic shrinkage than both NVC30 and NVC15. Accordingly, NVC60 contained no fly ash, while NVC30 and NVC15 both contained 25% fly ash by mass.

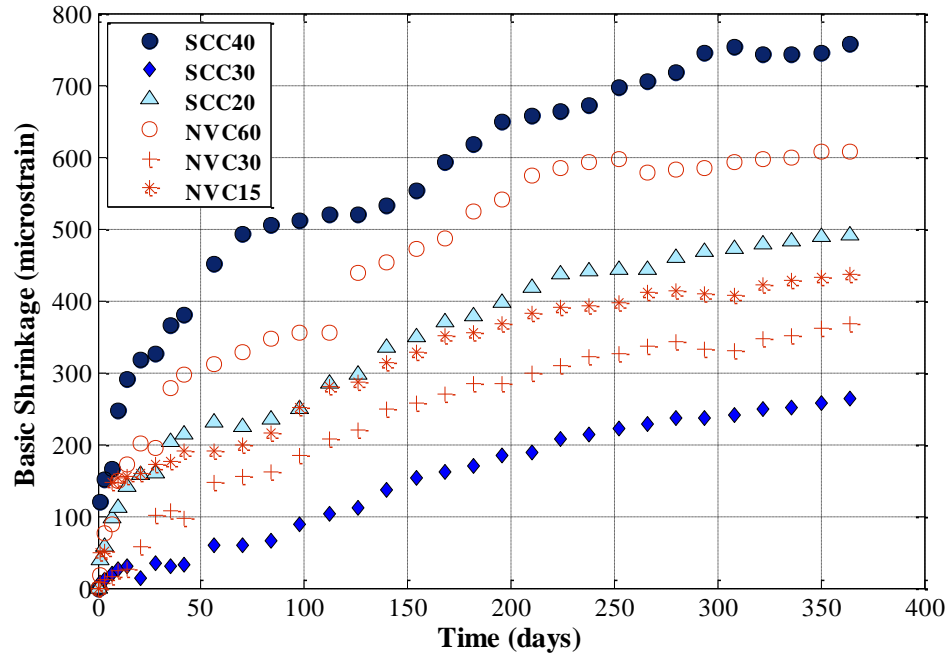


Figure 3.17. Basic shrinkage curves for all compression creep mixes

Figure 3.18 shows the compliance curves for mixes NVC60, SCC40, SCC30, and SCC 20. All of these mixes have a similar water/binder ratio and a similar cement paste volume of less than 33% of the total concrete volume. Figure 3.18 clearly shows that SCC40, SCC30, and SCC20 mixes experienced significantly higher creep compliance values compared with NVC60 over the entire test period. It is thought that higher sand-to-total aggregate ratio leads to decreased modulus of elasticity as well as increased creep and shrinkage [15, 125]. This partly explains the higher creep compliance of the examined SCC mixes with 0.53 sand-to-total aggregate ratio compared with NVC with 0.35 sand-to-total aggregate ratio. Additionally, the lower compressive strength and modulus of elasticity of SCC mixes due to the inclusion of fly ash might contribute to the higher creep compliance. Increasing fly ash content in the three SCC mixes led to remarkably higher total creep compliance. The relationship of the fly ash replacement

ratio to ultimate total creep compliance is shown in Figure 3.19. Specifically, increasing fly ash from 20% (SCC40), 40% (SCC30) to 60% (SCC20) caused the total creep compliance of SCC20 and SCC30 to be approximately double that of SCC40 at 364 days after loading. This effect is also shown in the comparison of the total creep compliance of NVC60 which contained no fly ash and the SCC mixes which all contained fly ash.

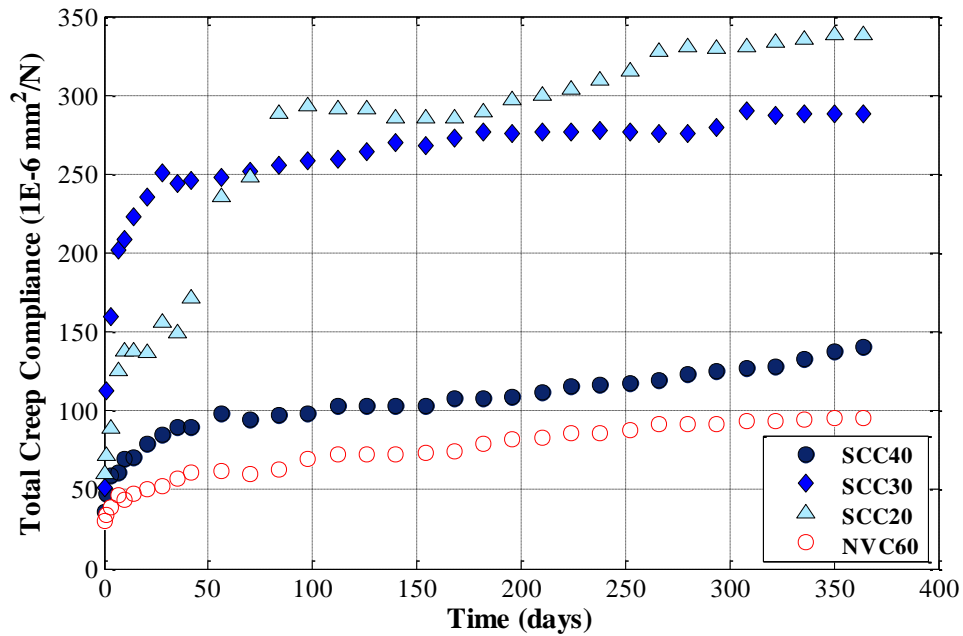


Figure 3.18. Total creep compliance curves for NVC60, SCC40, SCC30, and SCC 20

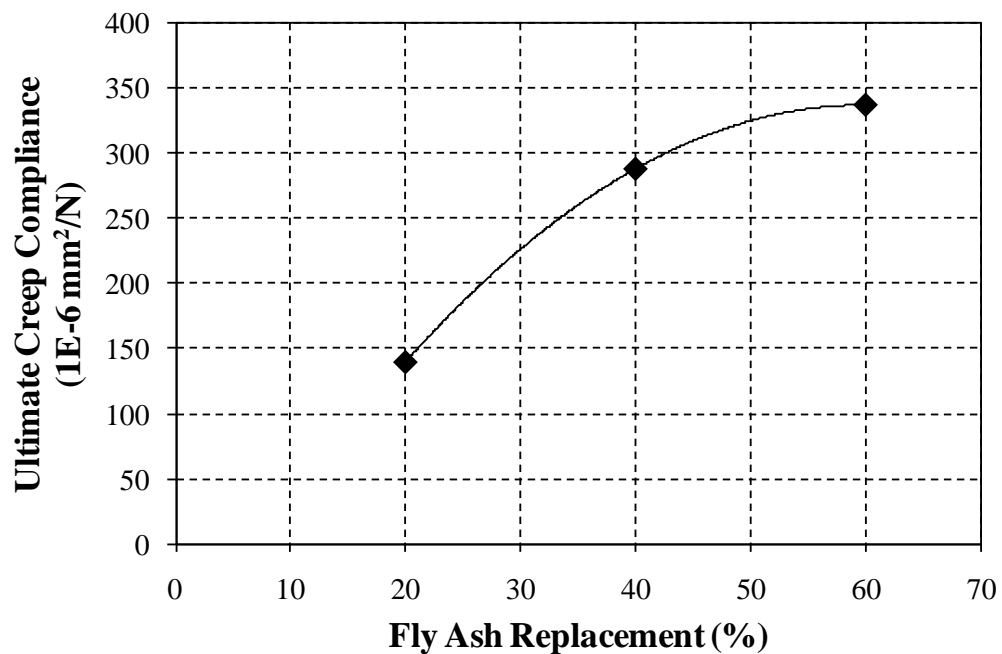


Figure 3.19. Ultimate creep compliance vs. fly ash replacement

The fact that all SCC mixes had a lower compressive strength than NVC60, could be the major factor in why they exhibited higher creep compliance. Moreover, the SCC mixes showed a clear trend of inverse correlation between strength and creep compliance compared with NVC60. Accordingly, the higher the compressive strength of an SCC mix, the lower its ultimate creep compliance.

To compare creep compliance of NVC mixes, both concretes should have similar strength. We therefore compare the SCC mixes SCC30 and SCC20 to the other mixes NVC30 and NVC15 listed in Table 3.2. These mixes exhibited a similar strength at time of loading as SCC30 and SCC20 respectively. Figures 3.20 and 3.21 show the creep compliance curves of the SCC mix and corresponding NVC mix with similar

compressive strength at time of loading. Clearly, from these results the SCC mixes exhibit higher creep compliance at all times compared with the NVC mixes of similar strength.

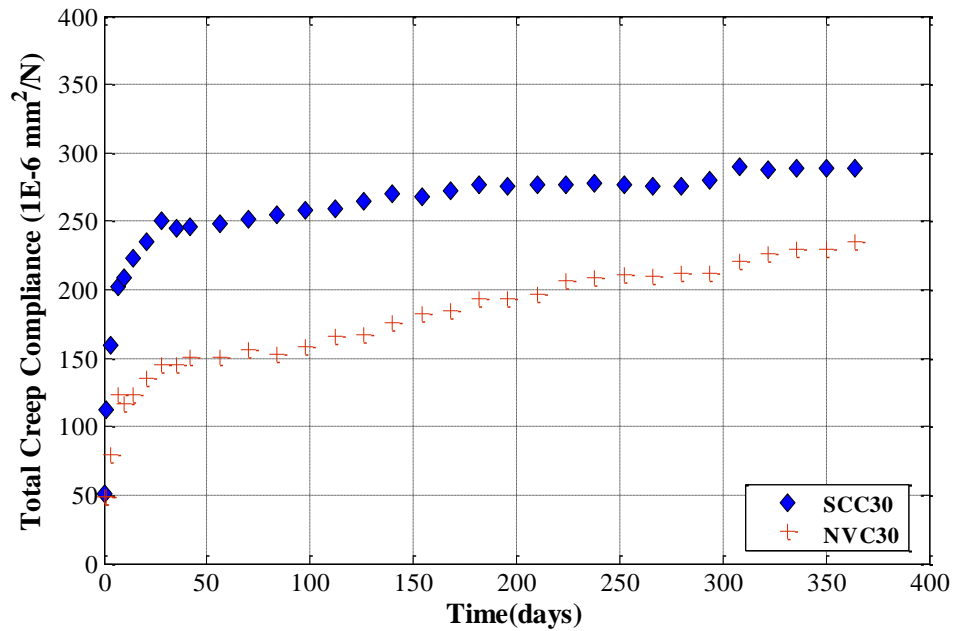


Figure 3.20. Total creep compliance curves for NVC30 and SCC30

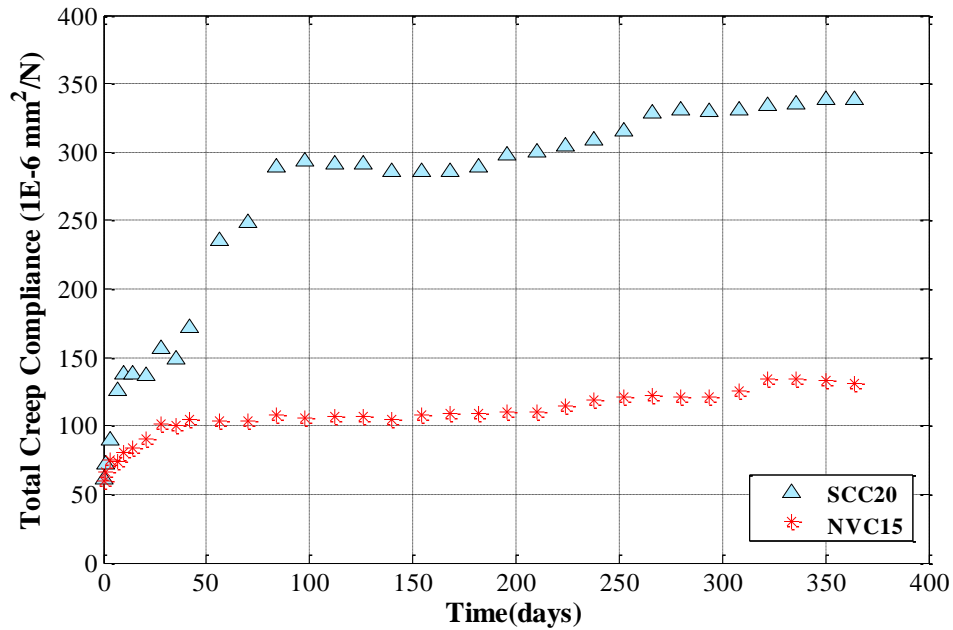


Figure 3.21. Total creep compliance curves for NVC15 and SCC 20

Moreover, a comparison of basic creep compliance curves of SCC40, SCC30, and SCC20 with NVC60 is shown in Figure 3.22. NVC60 and SCC40 showed comparable basic creep compliance over the entire test period. SCC20 and SCC30 with high fly ash contents showed higher basic creep compliance than SCC40 and NVC60. Therefore, increasing fly ash resulted in higher basic creep compliance. The influence of fly ash content on basic creep compliance is similar to its effect on total creep compliance. This observation is unexpected and opposite to the trends of basic shrinkage. Finally, SCC30 has less fly ash than SCC20 and showed a higher basic creep compliance, which may indicate some misleading information. Due to the limited number of experiments some experimental variation is expected and can account for some of these misleading trends. Therefore, further investigations are needed and recommended to explore the effect of fly ash on basic creep of SCC to support or negate these observations.

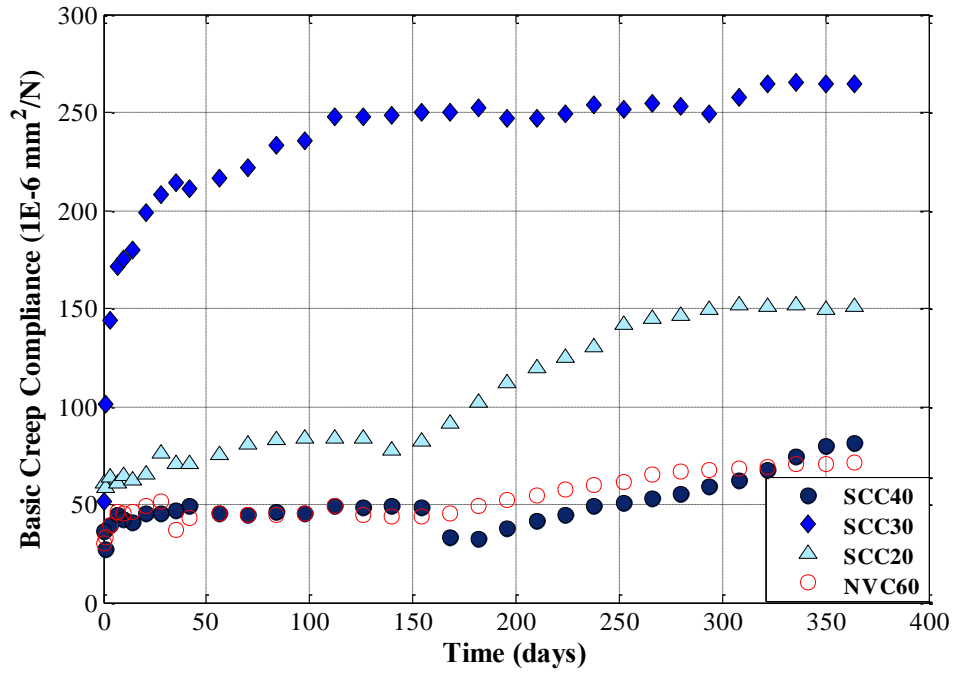


Figure 3.22. Basic creep compliance curves for NVC60, SCC40, SCC30, and SCC 20

Figure 3.23 and Figure 3.24 show the basic creep compliance of SCC and NVC mixes of similar strength. It is obvious that SCC mixes showed higher basic creep compliance when compared to NVC mixes of similar strength.

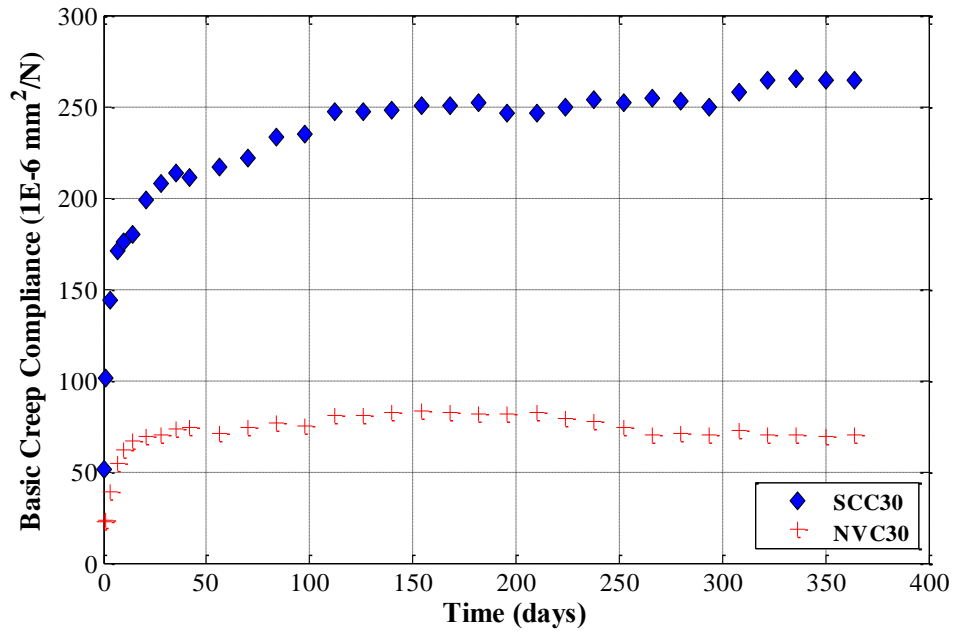


Figure 3.23. Basic creep compliance curves for NVC30 and SCC30

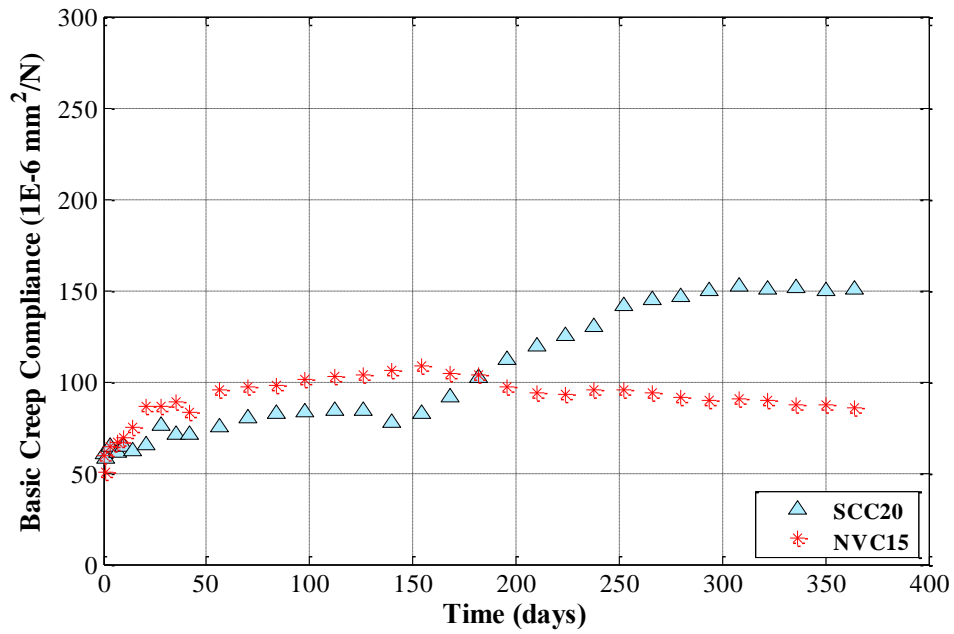


Figure 3.24. Basic creep compliance curves for NVC15 and SCC20

Table 3.6 displays the development rates at 14 and 28 days of age after loading for all of the compression creep specimens. Figure 3.25 and 3.26 show the total and basic creep compliance development rates of the six concretes at 28 days after loading respectively. It is important to notice that for the NVC mixes creep development is clearly a function of compressive strength. For the three NVC mixes a higher compressive strength related to a slower creep compliance development. Conversely, the SCC mixes showed no clear relationship between compressive strength and creep development rate. In fact, SCC showed no clear relationship between creep development rate and any pertinent concrete parameter.

Table 3.6. Creep compliance development rate for compression creep experiments

	SCC40	SCC30	SCC20	NVC60	NVC30	NVC15
Total Creep Compliance (J_C)						
J_{C14}/J_{CU}	0.50	0.77	0.40	0.49	0.52	0.64
J_{C28}/J_{CU}	0.60	0.87	0.46	0.55	0.63	0.77
Basic Creep Compliance (J_{CB})						
J_{CB14}/J_{CBU}	0.50	0.68	0.41	0.64	0.95	0.88
J_{CB28}/J_{CBU}	0.55	0.78	0.51	0.71	1.0	1.0

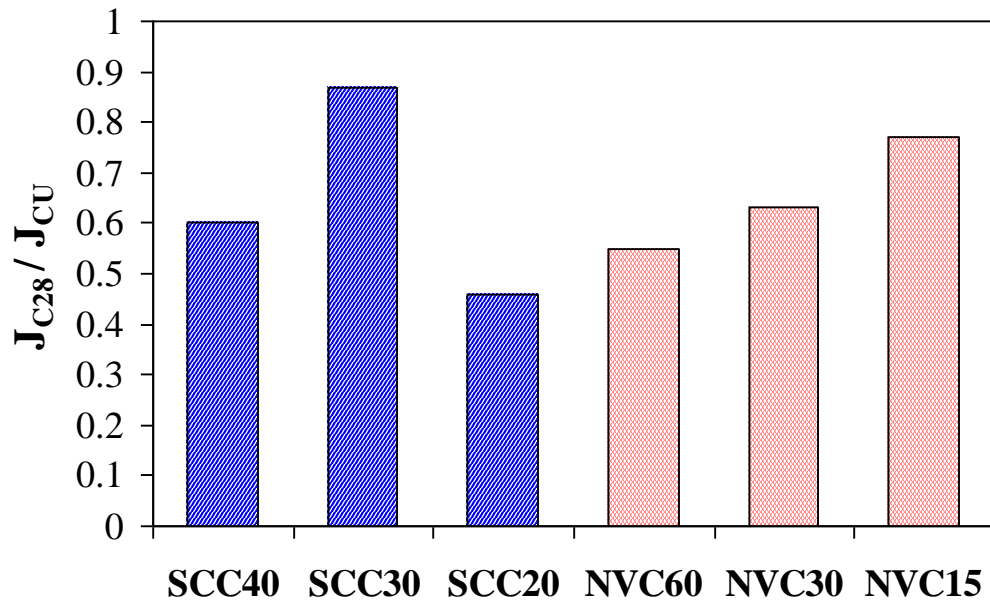


Figure 3.25. Total creep compliance development rate at 28 days after loading

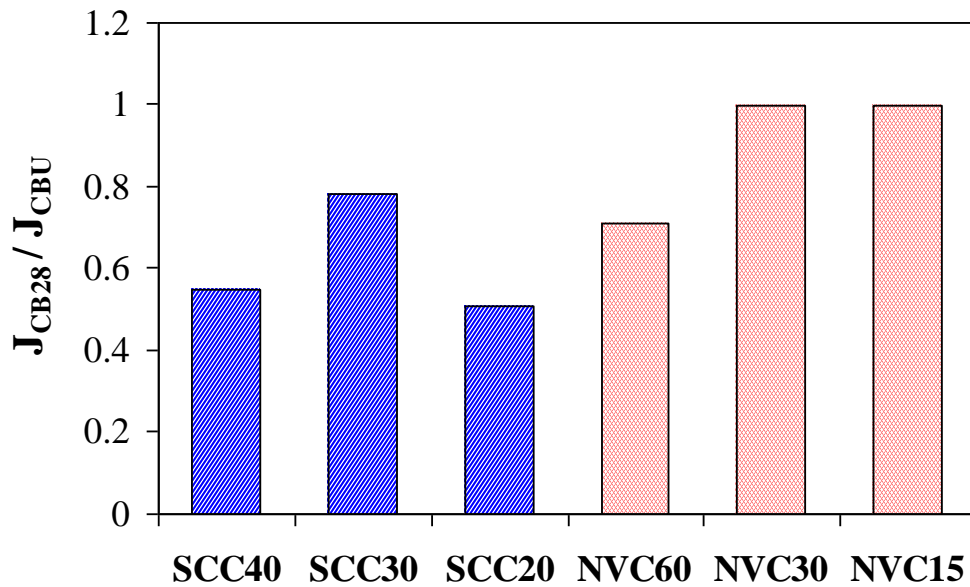


Figure 3.26. Basic creep compliance development rate at 28 days after loading

3.3.5.2 *MODELING OF SCC COMPRESSION CREEP RESULTS USING ACI 209 AND CEB-FIPMC-90*

The purpose of this work is to investigate creep and shrinkage of SCC compared with NVC. It is important to compare the SCC creep to that predicted of similar concretes using the current concrete design models. Here we compare our experimental results to the creep prediction by ACI-209 and CEB-FIP MC-90 creep models.

To attempt to model the SCC compression creep experiments with the ACI-209 model, a slump of 300 in was assumed to model all three mixes (SCC40, SCC30, and SCC20). This was done since the ACI model requires the slump height to compute creep coefficient. Figure 3.27, Figure 3.28, and Figure 3.29 present the creep prediction using the ACI 209 model along with the RMSE between the predicted and experimental values. The ACI model does not accurately predict creep coefficient of SCC with a RMSE of 1.174 and 1.183 for prediction of SCC40 and SCC30 respectively. The model prediction of SCC20 was relatively accurate with a RMSE of 0.476, however the model still slightly underestimated creep coefficient. Clearly, the dependence on slump does not allow the ACI-209 model to accurately predict the creep coefficient of SCC.

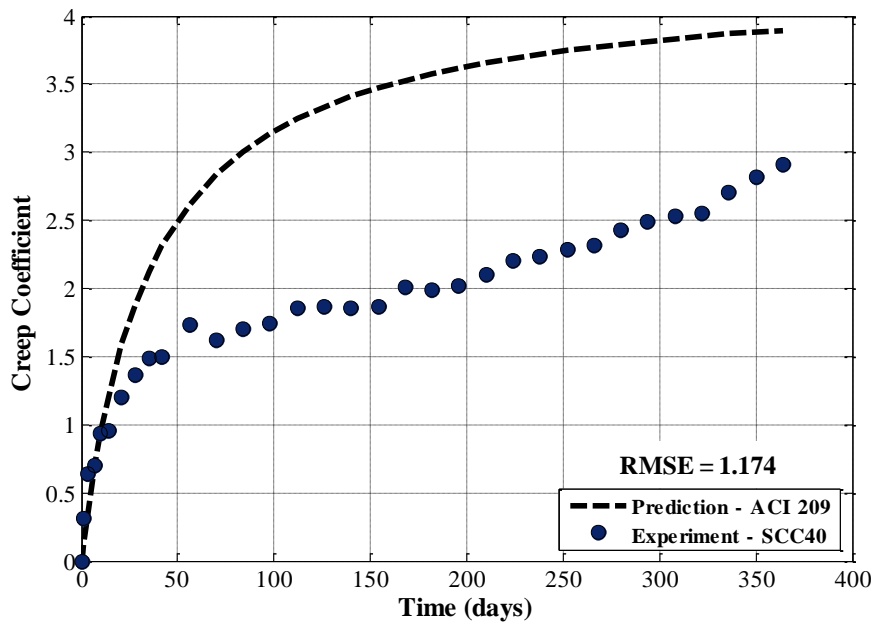


Figure 3.27. Prediction of creep coefficient of SCC40 using ACI-209 model

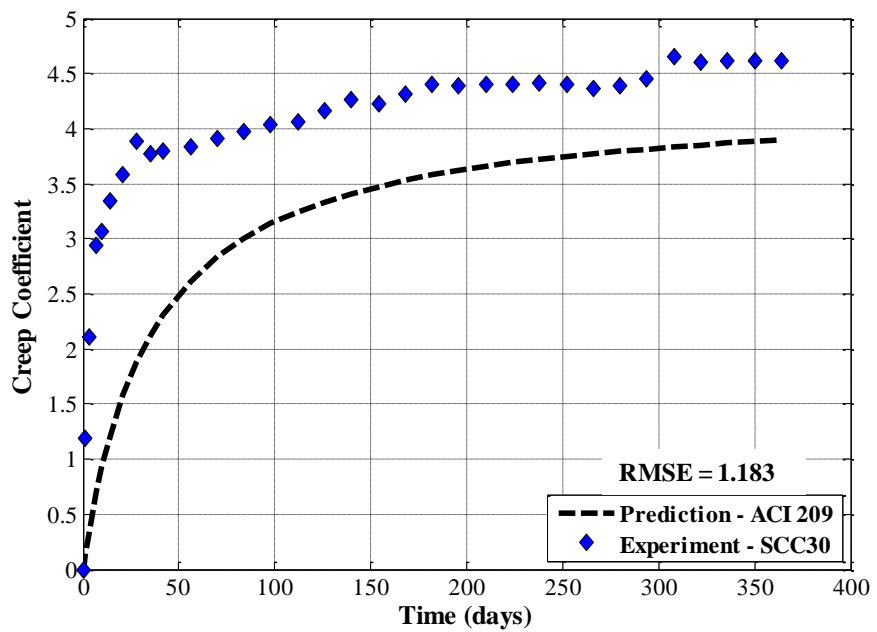


Figure 3.28. Prediction of creep coefficient of SCC30 using ACI-209 model

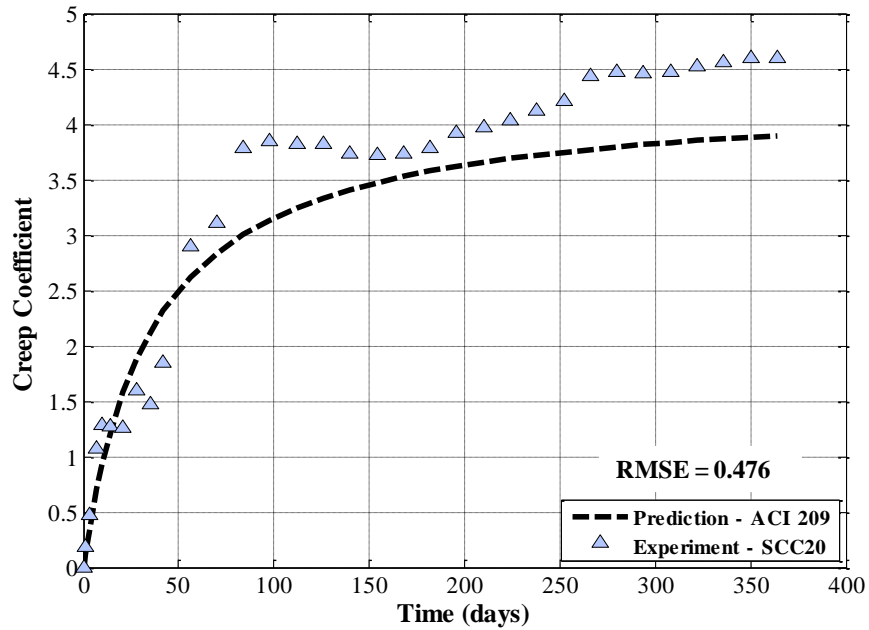


Figure 3.29. Prediction of creep coefficient of SCC20 using ACI-209 model

To account for the inaccuracy of the ACI-209 model's prediction of creep of SCC, a new coefficient was proposed to replace the slump coefficient in calculating the creep coefficient. This new coefficient was based on the fly ash replacement percentage and defined in Equation (3.21). Figure 3.30, Figure 3.31 and Figure 3.32 show the prediction of creep coefficient for the three SCC mixes based on the modified ACI model. Clearly, modifying the ACI-209 model based on fly ash percentage allows for a more accurate prediction of creep of SCC containing fly ash. The RMSE between predicted and experimental values was reduced to 0.449, 0.889, and 0.346 for SCC40, SCC30 and SCC20 respectively. It is important to note here that the ACI-209 model underestimates the early creep coefficient (first 100 days) which explains the relatively high RMSE for SCC30 using the proposed fly ash coefficient.

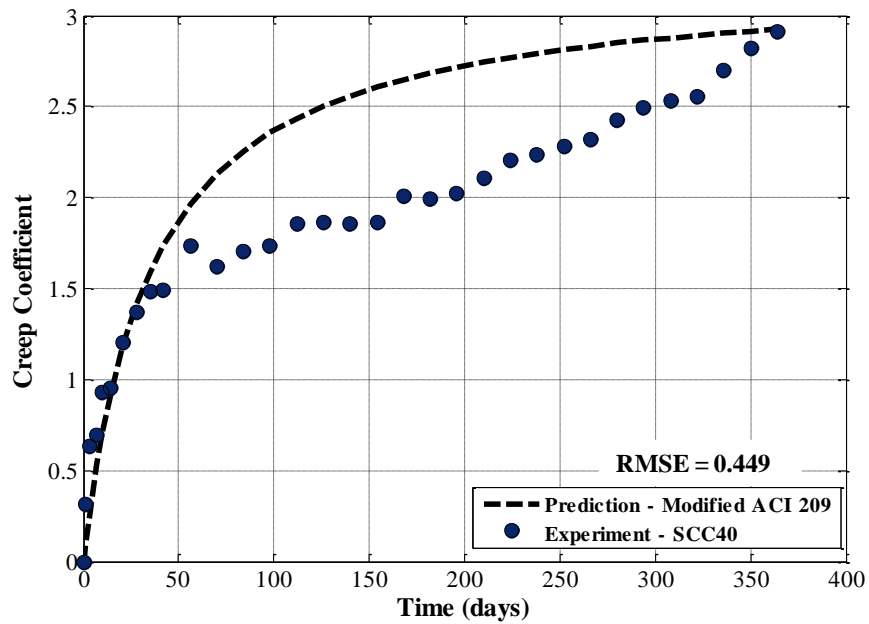


Figure 3.30. Prediction of creep coefficient of SCC40 using modified ACI-209 model

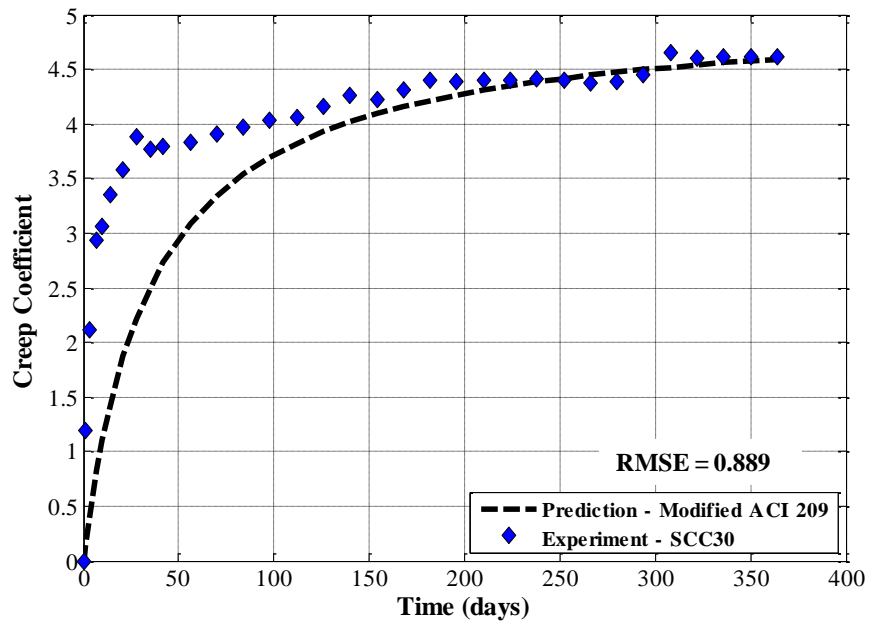


Figure 3.31. Prediction of creep coefficient of SCC30 using modified ACI-209 model

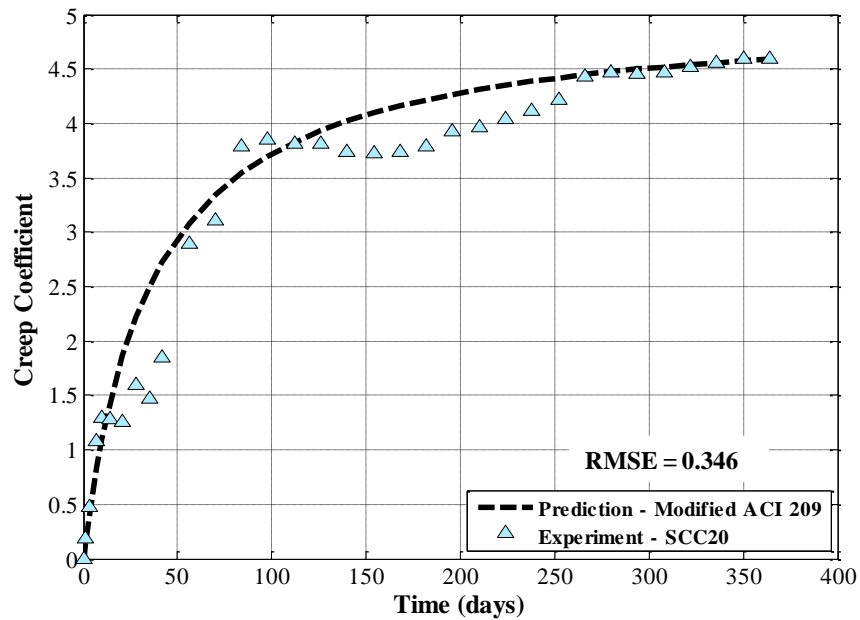


Figure 3.32. Prediction of creep coefficient of SCC20 using modified ACI-209 model

To get further insight into the creep of SCC, the experimental results were compared to the CEB –FIP MC90-99 model. Since the CEB-FIP model has been proven to be very accurate in modeling creep of concrete, a comparison with the CEB-FIP model should give a good indication of how creep of SCC compares with typical concretes. It should be noted here that CEB-FIP recommends that the model only be used for ambient relative humidity of greater than 40%. The concrete specimens experienced a variable relative humidity in the range of 20% to 75% throughout the experimental period. Since the mean relative humidity was 34% during this period, the minimum value of 40% was used in the CEB-FIP model. Using this value should have a minimal effect on prediction of the creep coefficient.

Figures 3.33 to 3.35 show the MC90 – 99 creep coefficient predictions and the creep coefficients from the compression experiments performed on the three SCC mixes. Clearly, SCC mixes exhibit a higher creep than the MC90 – 99 creep model predicts. The RMSE was found to be 0.521, 2.103 and 0.931 for SCC40, SCC30 and SCC20 respectively. The RMSE is especially high for the SCC30 mix. This might have occurred because the intermediate amount of fly ash (40%) in SCC30 did not have a significant effect on strength but changed the microstructure enough to affect viscoelastic properties. These results show that the CEB-FIP model also needs to be modified to allow for more accurate creep predictions of SCC mixes containing fly ash.

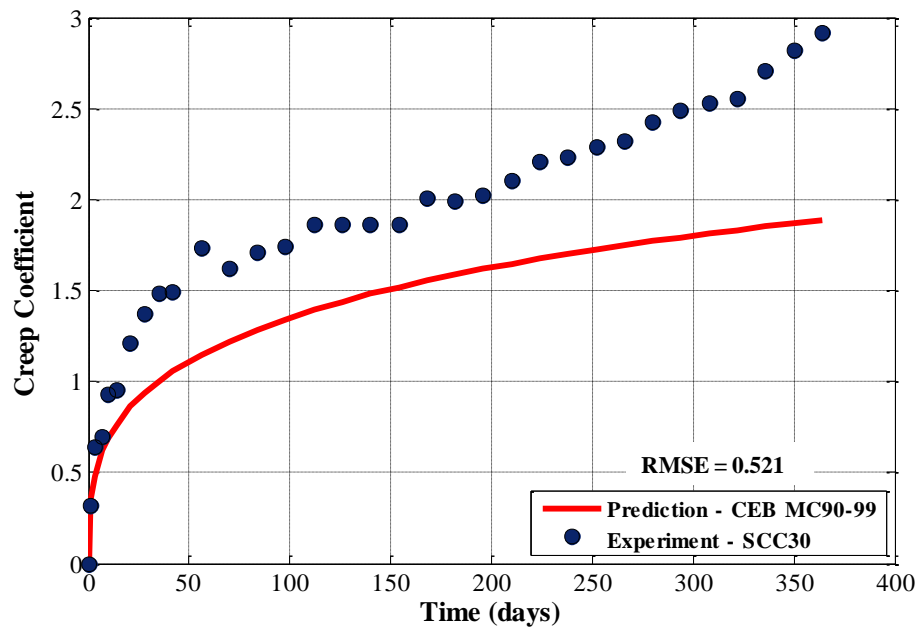


Figure 3.33. CEB-FIP prediction model of creep coefficient for SCC40

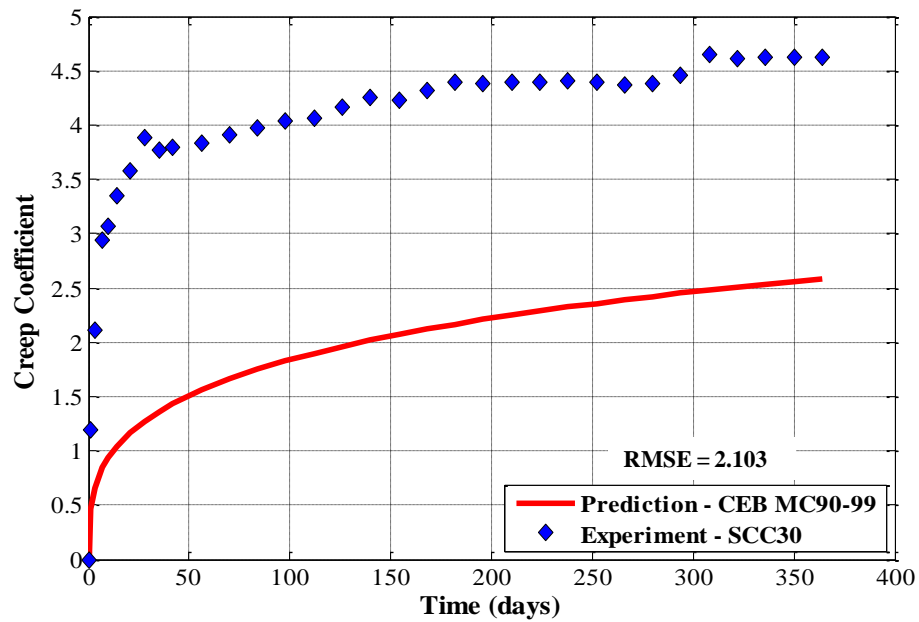


Figure 3.34. CEB-FIP prediction model of creep coefficient for SCC30

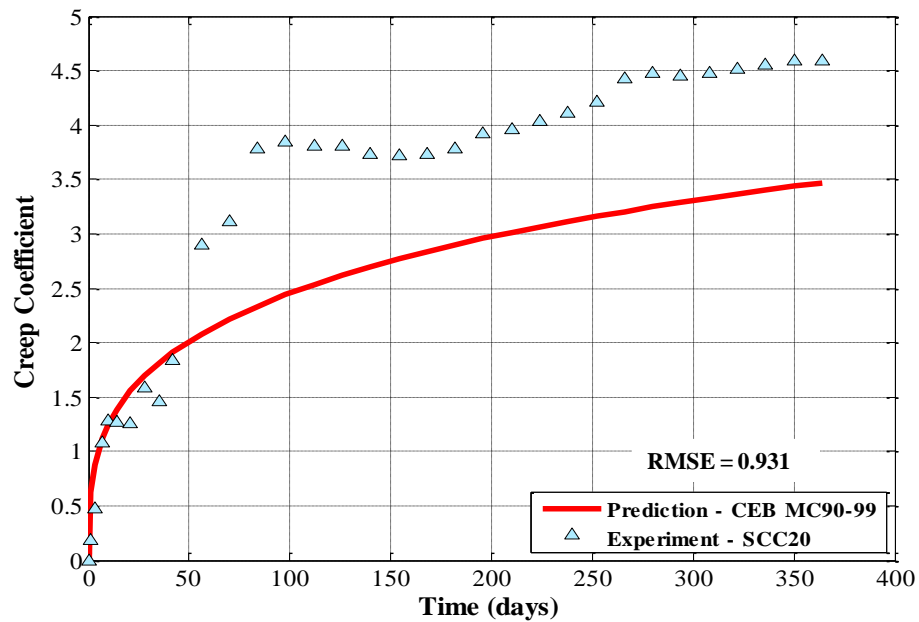


Figure 3.35. CEB-FIP prediction model of creep coefficient for SCC20

3.4 TENSION CREEP EXPERIMENTS

3.4.1 MATERIALS AND MIX PROPORTIONS

SCC and NVC mixes for tension creep experiments were designed to have a similar direct tensile strength at 7 days (time of loading). The SCC mixes used in this investigation included 40% and 55% fly ash by weight. Table 3.7 shows the proportions of the five mix designs used in this investigation. Table 3.8 shows presents the properties of the cement paste for the four mixes used in these experiments.

Table 3.7. Mix proportions of concrete mixes used in tension experiments

	Weight per unit volume, kg/m ³					mL/m ³	
	Water	Cement	Fly Ash	Fine	Coarse	SP	VMA
SCC2.2	150	270	180	902	794	4050	1800
SCC1.5	150	203	248	886	779	4500	1800
NVC2.4	185	289	97	700	1143	1570	---
NVC1.3	198	260	0	700	1143	0	---

Table 3.8. Properties of the cement paste for SCC2.2, SCC1.5, NVC2.4, and NVC1.3

	Fly Ash replacement (%)	Volume of Cement Paste (%)	Water Cement Ratio	Water Binder Ratio
SCC2.2	40	32	0.56	0.33
SCC1.5	55	33	0.74	0.33
NVC2.4	25	32	0.64	0.48
NVC1.3	0	28	0.76	0.76

3.4.2 EXPERIMENTAL METHODS

3.4.2.1 MIXING

For the tensile creep experiments, the mixing procedure outlined in Section 3.3.2.1 was followed.

3.4.2.2 FRESH PROPERTIES

To characterize the fresh SCC mixes the slump flow, T_{50} , and passing ability tests were performed in accordance to the procedure set forth in Section 3.3.2.2. As with the compression experiments all mixes met the self-consolidation criteria. The conventional slump test was again performed on the fresh NVC mixes. Table 3.9 presents the fresh properties found for the four concrete mixes.

Table 3.9. Fresh properties of mixes used in tensile creep experiments

	Slump flow (mm)	T_{50} time (s)	Passability (%)
SCC2.2	730	3.8	78
SCC1.5	720	2.9	99
NVC2.4	180*	---	---
NVC1.3	235*	---	---

*Conventional Slump

3.4.2.3 SPECIMENS

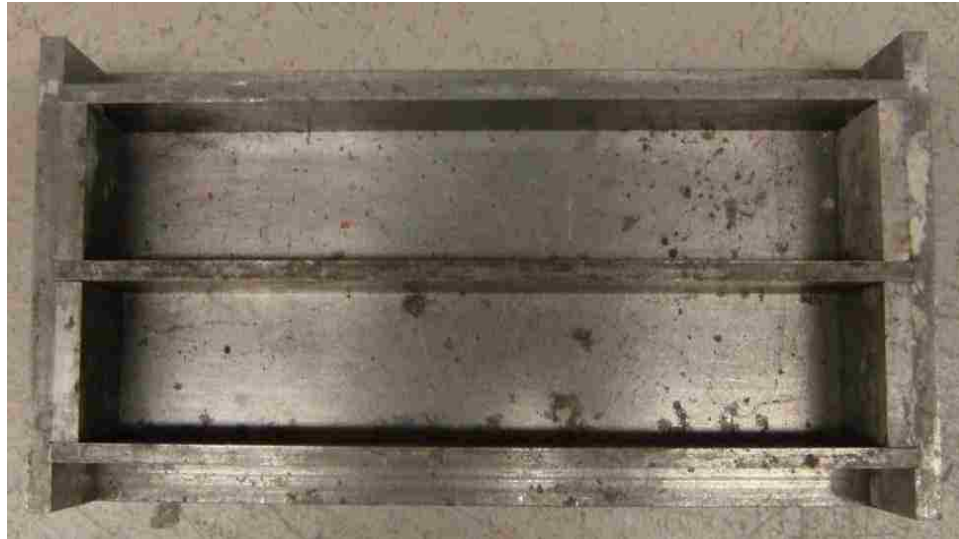


Figure 3.36. Tension creep specimen forms

Concrete was cast into prisms of 50 mm x 50 mm in cross-section and 280 mm in length, forms are shown in Figure 3.36. As in the case with compression creep experiments, identical specimens were created to discern shrinkage strains. Specimens were allowed to harden in the molds for 24 hours before being placed in a curing bath as described in Section 3.3.2.3. Creep and shrinkage specimens were taken out of the curing bath after 4 days and approximately 5 mm was cut off the top ends of the specimens with a diamond blade saw. Then specimens were allowed to air dry for 24 hours. Upon drying, two steel 50 mm x 50 mm x 25 mm end plates were attached to creep specimens with high strength epoxy adhesive. The West Systems Brand epoxy consisted of 5 parts West Systems 105 Epoxy Resin and 1 part West Systems 205 Hardener. Throughout curing, pressure was applied to the specimens and the plates using c-clamps, as shown in Figure 3.37.



Figure 3.37. Curing of epoxy with applied pressure using c-clamps

After allowing the epoxy to cure for 24 hours, the specimens to be used for basic creep and shrinkage measurements were wrapped with a double layer of aluminum tape. DEMEC disks were then attached to the specimens as with the compression specimens. The reference bar used to place the DEMEC disks gave an initial gauge length of 200 mm. Figure 3.38 shows a schematic of the placement of DEMEC disks.

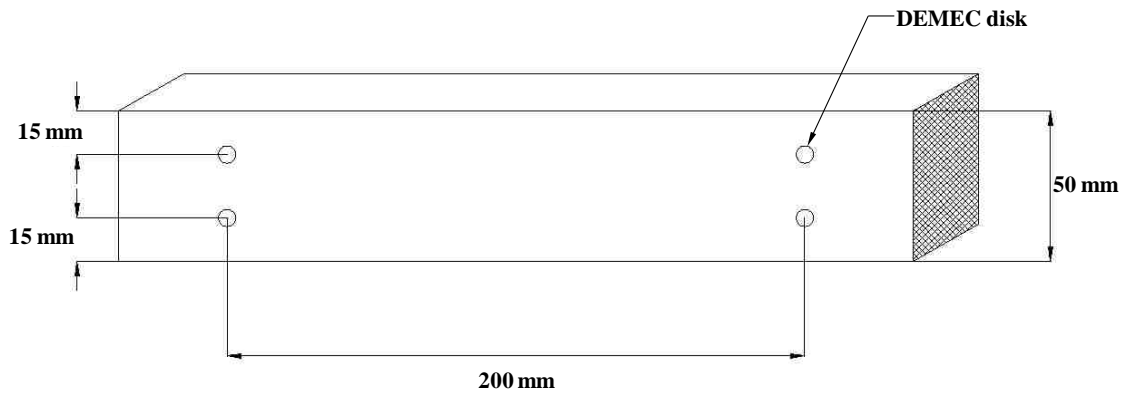


Figure 3.38. Schematic of DEMEC disk placement for tension creep specimens

3.4.2.4 MECHANICAL CALIPER

Readings were taken on all specimens using a mechanical caliper manufactured by Mayes Instruments, Co., similar to the caliper used in the compression experiments. This mechanical caliper takes readings with respect to a reference bar with a gauge length of 202 mm. DEMEC disks were placed with placement bar manufactured to fit the reference bar. The gauge on the caliper reads from 0 to 2500, where each one increment represents 0.002 mm of displacement. This gives the caliper a range of 1.62 mm for compression displacement and 3.38 mm for tension displacements. The “zero” reading on the reference bar is 810, so length measurements using the caliper are represented by Equation (3.35).

$$L \left[\frac{R}{10} \right] * 0.0016 \left[\frac{1}{0.02} \right] \quad (3.35)$$

R : reading taken on the mechanical caliper when inserted in mounted specimen DEMEC points

L : distance between DEMEC disks measured in mm

3.4.2.5 COMPRESSIVE AND DIRECT TENSILE STRENGTH

Compressive strength of the concrete mixes was determined from the method explained in Section 3.3.2.5 at 7 and 28 days of age.

Table 3.10. Mean and standard deviation of 7 and 28 day compressive strength of tension creep specimens

	7 day Mean Compressive Strength, f_c' (MPa)	7 day Standard Deviation (MPa)	28 day Mean Compressive Strength, f_c' (MPa)	28 day Standard Deviation (MPa)
SCC2.2	22.5	1.2	31.9	0.8
SCC1.5	11.0	0.3	17.4	0.1
NVC2.4	23.5	1.5	31.4	0.4
NVC 1.3	8.6	0.2	12.3	1.0

The 28 and 7 day tensile strength was determined by using direct tension test of concrete cylinders [126]. In this test setup, the ends of the concrete cylinders were attached to steel end plates using the high strength epoxy. The specimens are then placed attached to steel plates mounted to a UTM (Tinus Olsen) with steel bolts. The test setup ensures that the test ends are rotation free to ensure uniform stress distribution. Figure 3.39 shows a concrete specimen failed under direct tensile stresses using this test setup.

The specimens are pulled apart and the maximum load is recorded. The ultimate tensile strength (f_t) is then calculated as

$$f_t = \frac{P_{max}}{A} \quad (3.36)$$

P_{max} : maximum load recorded from direct tension test

A : cross-sectional area of the concrete specimen ($A = 7854 \text{ mm}^2$ for 100mm cylinder diameter)



Figure 3.39. Direct tension test with fractured specimen after Kim et al.

Table 3.11. Mean and Standard deviation of 7 and 28 day tensile strength

	7 day Mean Tensile Strength, f_t (MPa)	7 day Standard Deviation (MPa)	28 day Mean Tensile Strength, f_t (MPa)	28 day Standard Deviation (MPa)
SCC2.2	2.2	0.3	2.0	0.1
SCC1.5	1.5	0.03	1.8	0.1
NVC2.4	2.4	0.3	2.7	0.2
NVC 1.3	1.3	0.1	1.7	0.1

3.4.2.6 TENSILE CREEP EXPERIMENTAL SETUP

Figure 3.40 shows a schematic of the tension creep test setup. In this test setup tensile stresses were applied using a cantilever based load system. One end of the concrete specimens were connected with steel chain link to a steel cantilever beam resting on a roller support (pivot) attached to a steel frame. The other end of the concrete specimen was anchored to the floor by attaching another length of steel chain to anchor weights. The use of steel chain was to eliminate any bending stresses that would develop in a rigid system. To apply the desired tensile loading weights were hung on the side opposite to the specimen on the cantilever. The cantilever had a length ratio of 5.22 to 1 in relation to the roller support (pivot). This allowed for generating a load 5.22 times the weight of the loading weights hung on the cantilever. To measure the load applied, an S-beam load cell was connected in between chain links in the bottom chain length at the time of loading.

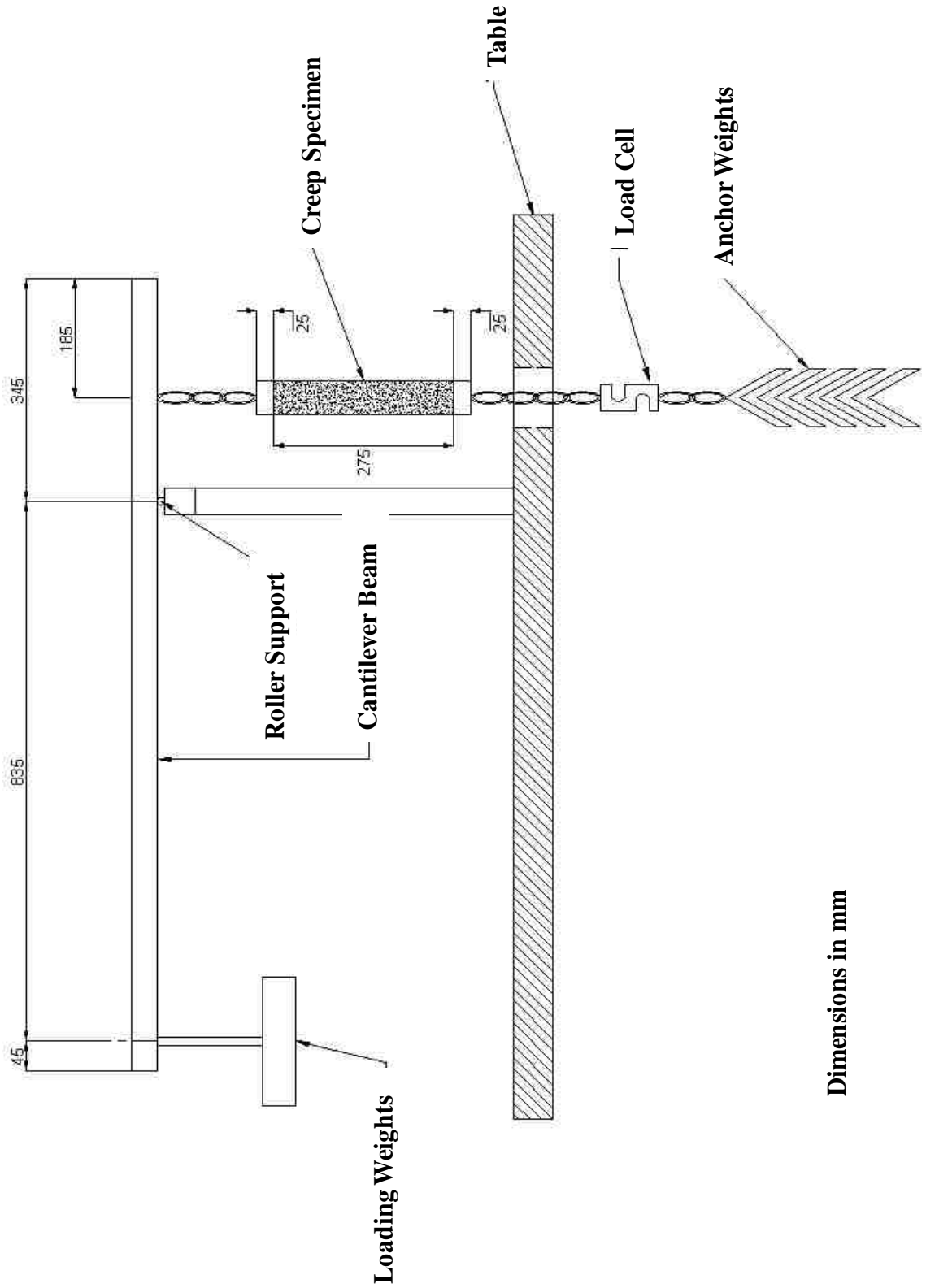


Figure 3.40. Schematic drawing of tension creep experimental setup

Each steel frame housed two cantilever beams allowing for loading two specimens per steel frame. Welded plates were used to restrict any out of plane movement of the cantilevers. Figure 3.41 shows a schematic of the steel frames used to house the cantilevers.

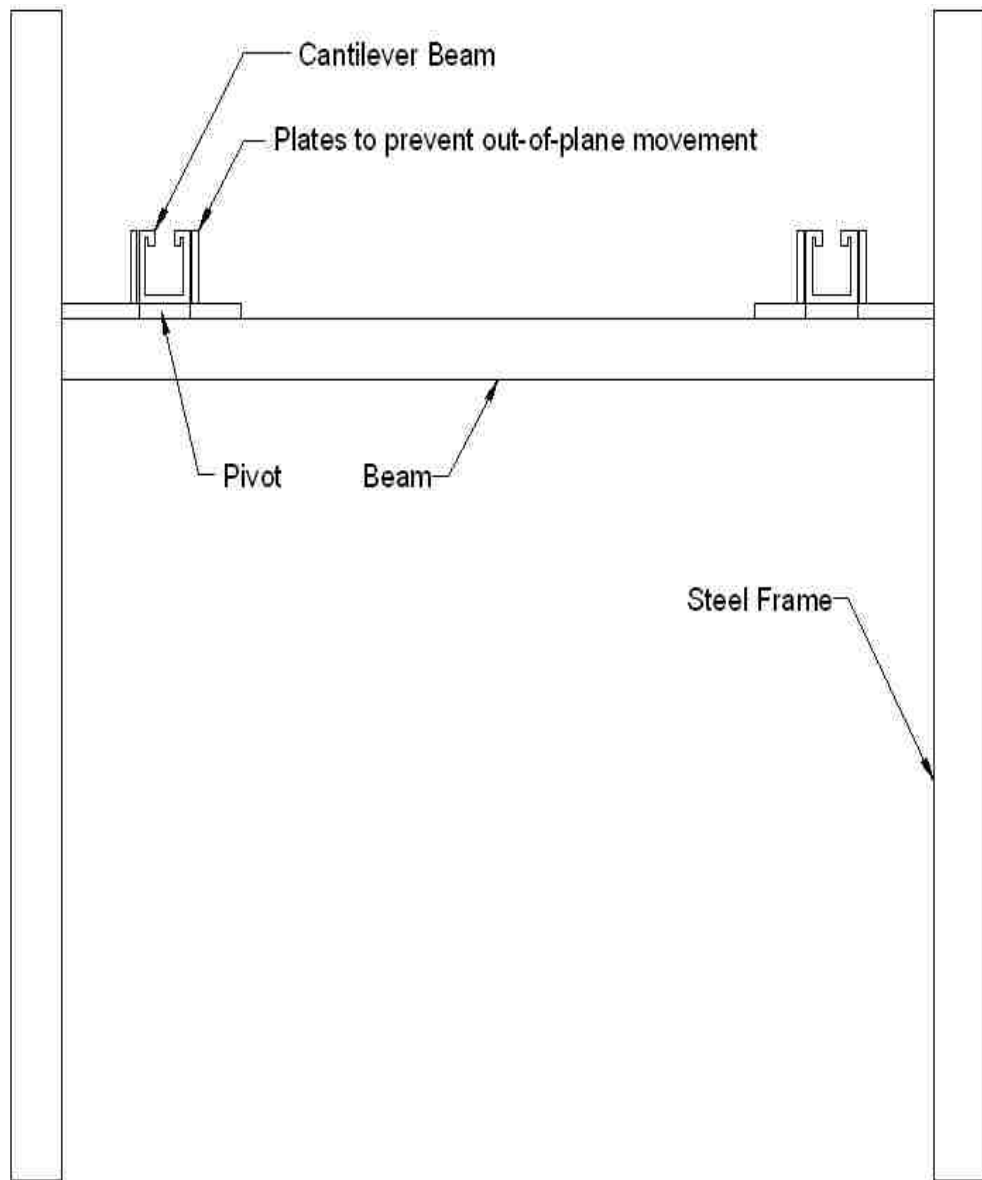


Figure 3.41. Schematic of steel frame used in tension creep test

The specimens were connected to the lengths of steel chain with eyebolts secured into pre-drilled holes in the top and bottom steel capping plates, which were pre-attached to concrete specimens with epoxy. Eyebolts were also used to connect the chain to the cantilever beams. Figure 3.42 shows a tensile creep specimen attached to a cantilever beam with a close up of the eyebolts.

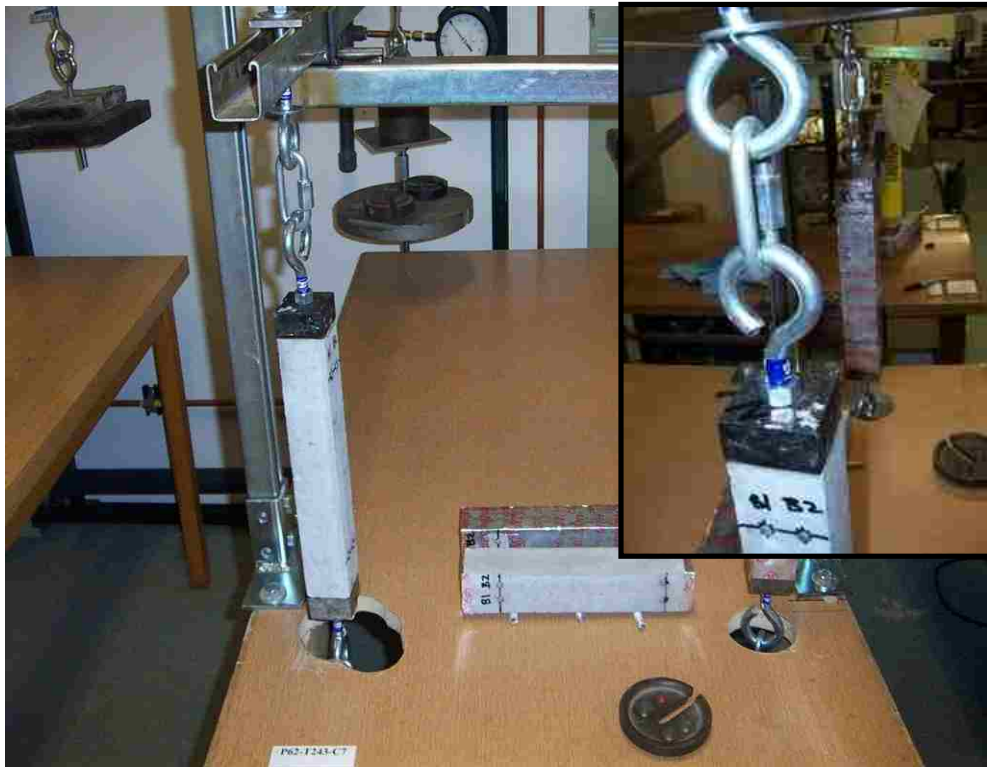


Figure 3.42. Attachment of tensile creep specimen to cantilever beam used to apply load

The bottom length of chain was attached to eyebolts secured to a beam resting on the floor. This beam was anchored to the floor with angle iron. Figure 3.43 shows the attachment of the bottom length of steel chain to the steel beam held down with anchor weights.



Figure 3.43. Steel chain anchored to the ground angle iron counter weights

Tensile creep specimens were loaded at 7 days of age. The tensile creep stress was 25% of the ultimate tensile strength found using the aforementioned direct tensile test. More pictures of the tension test setup are shown in the appendices.

3.4.2.7 MEASUREMENTS AND SPECIMEN STORAGE

Tension creep and shrinkage specimens were kept under the same environmental conditions as the previously mentioned compression specimens. Measurements of tension creep and corresponding shrinkage strains were recorded using a similar mechanical caliper at 1, 2, 3, 5, 7, 10, 14, 21, 35 and 42 days of loading time and every 14 days thereafter for the duration of 100 days.



Figure 3.44. Storage of tension test specimens

3.4.3 ANALYSIS OF EXPERIMENTAL DATA

As in the compression creep experiments length measurements were converted to strains using Equation (3.4). The elastic strain was again recorded independently to separate elastic strains from creep strains. Equations (3.37) and (3.38) represent the strains measured on both unsealed and sealed tension creep specimens, respectively. On the other hand, Equations (3.39) and (3.40) measurements from unsealed and seal shrinkage specimens respectively. Since, creep strains and shrinkage strains act in the opposite direction under tensile stress shrinkage strains were considered negative and creep strains were considered negative for superposition.

$$\epsilon_{creep\ unsealed} = \epsilon_{bc} + \epsilon_{dc} - \epsilon_{bs} - \epsilon_{ds} \quad (3.37)$$

$$\epsilon_{creep\ sealed} = \epsilon_{bc} - \epsilon_{bs} \quad (3.38)$$

$$\epsilon_{shrinkage\ unsealed} = \epsilon_{bs} - \epsilon_{ds} \quad (3.39)$$

$$\epsilon_{shrinkage\ sealed} = \epsilon_{bs} \quad (3.40)$$

$\epsilon_{creep\ unsealed}$: total strain obtained from unsealed creep specimens

$\epsilon_{creep\ sealed}$: total strain obtained from sealed creep specimens

$\epsilon_{shrinkage\ unsealed}$: total strain obtained from unsealed shrinkage specimens

$\epsilon_{shrinkage\ sealed}$: total strain obtained from sealed shrinkage specimens

ϵ_{dc} : strain due to drying creep

ε_{bc} : strain due to basic creep

ε_{ds} : strain due to drying shrinkage

ε_{bs} : strain due to basic shrinkage

The creep compliance for concrete specimens was then calculated using Equation (3.10). The elastic strain recorded after immediate loading of the specimen was used to calculate the elastic modulus at time of loading. This was done to account for the difference in elastic modulus of concrete in tension and compression.

3.4.4 RESULTS AND DISCUSSION

Figure 3.45 shows the shrinkage strains with time for both SCC and NVC mixes. There appears to be no significant difference in the shrinkage of SCC2.2, SCC1.5 and NVC2.4. This observation meets expectations since these three mixes all have a similar volume of cement paste at about 32% of the total concrete volume. It is interesting to note that SCC1.5 shows a drop in shrinkage at 42 days, this might be attributed to an increase of relative humidity in the lab at this time. Interestingly, NVC1.3 showed the highest amount of total shrinkage and had the lowest volume of cement paste at 28%. This could be attributed to the extremely high water cement ratio of this mix, which was used to achieve a low 7 day tensile strength without significantly replacing cement with fly ash.

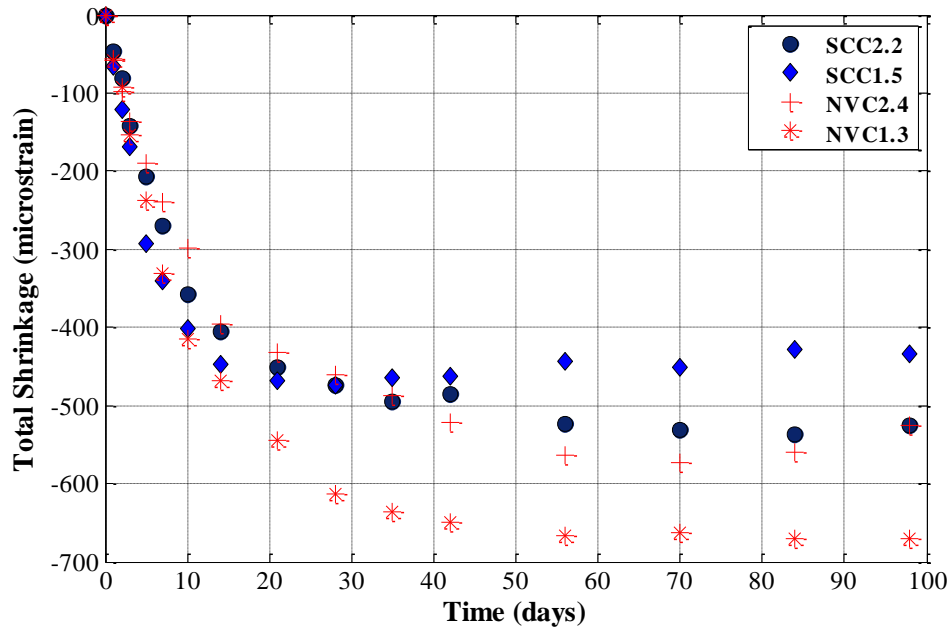


Figure 3.45. Shrinkage strains of SCC2.0, SCC1.5, NVC2.4, and NVC1.3

Figure 3.46 shows the weight loss percentage for all of the SCC and NVC mixes used for the tension creep experiments. Both SCC mixes had a higher weight loss percentage than the NVC mixes. This might be explained by the fact that SCC mixes contained more fly ash than NVC mixes, even though the mixes had a similar or higher volume of cement paste. SCC1.5 shows the highest amount of weight loss for the first 56 days. This can be related to the fact that SCC1.5 had a high amount of fly ash replacement at 55%. The drop in the weight loss of SCC1.5 might be explained by an increase in the relative humidity in the laboratory. The discrepancy between shrinkage measurements and weight loss can be attributed to the significantly low shrinkage strains and the associated difficulty in attaining them accurately.

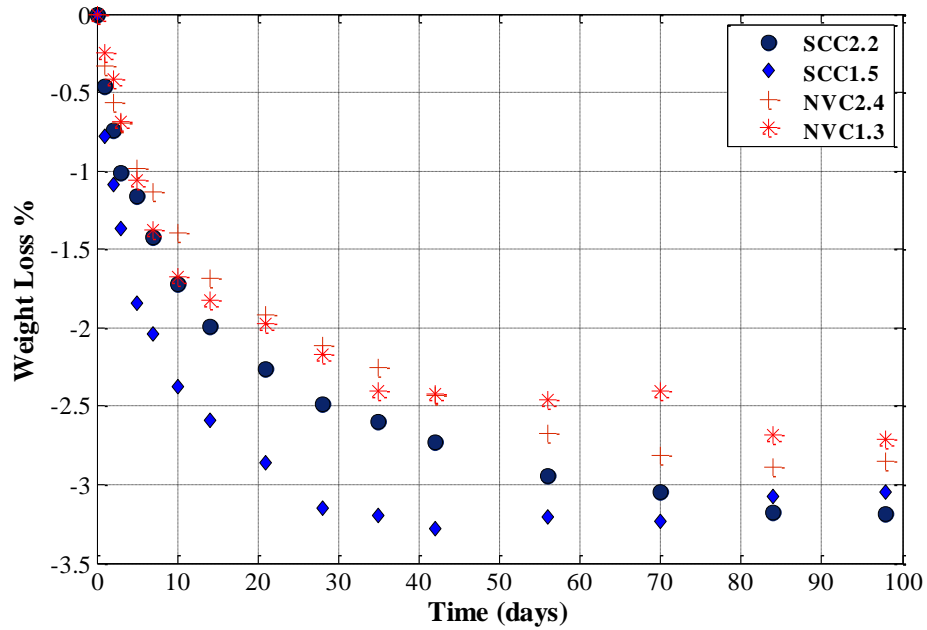


Figure 3.46. Weight loss percentage of SCC2.0, SCC1.5, NVC2.4, and NVC1.3

Figure 3.47 presents the basic shrinkage strain for all the mixes. From this figure it is shown that both SCC mixes exhibited similar basic shrinkage strains in comparison to NVC2.4. Like the total shrinkage results NVC1.3 showed the highest basic shrinkage strain. This might be attributed to the significantly higher water/binder ratio of this NVC mix compared with the other mixes. That change in water/binder ratio was intended to maintain similar strengths to account for the significant effect of strength on creep.

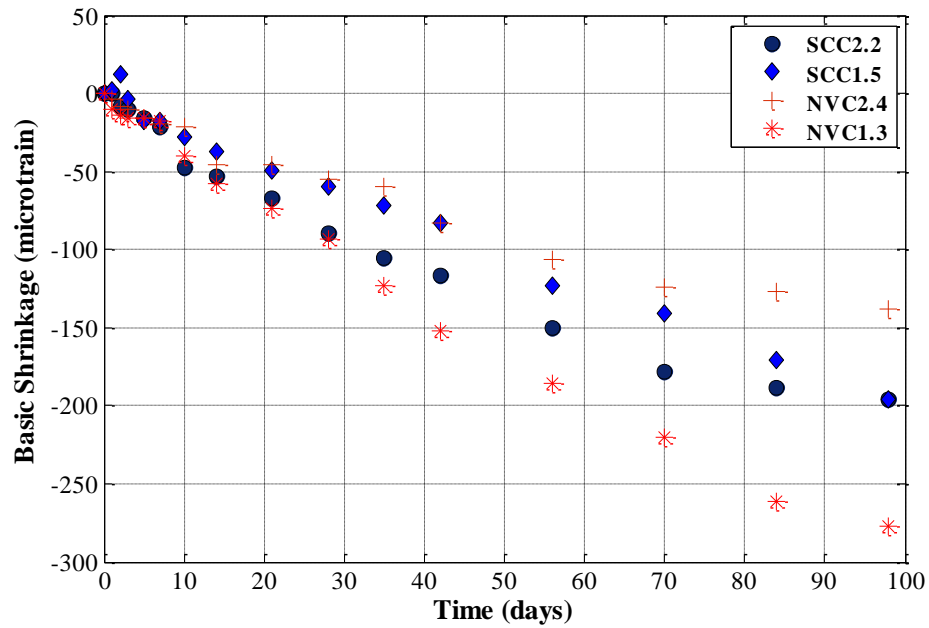


Figure 3.47. Basic shrinkage strains of SCC2.0, SCC1.5, NVC2.4, and NVC1.3

Figure 3.48 displays the total tension creep compliance with time for all SCC and NVC mixes. SCC2.2 showed slightly higher creep compliance than NVC2.4 (shown in Figure 3.49). However, NVC1.3 had higher creep compliance than SCC1.5 even though both concretes had a similar tensile strength at loading (shown in Figure 3.50). This might be attributed to the extremely high water/binder ratio used to achieve NVC1.5's target strength. NVC1.5 showed the lowest amount of weight loss. This might explain the high creep compliance because concretes experiencing lower water losses are less likely to experience stress induced shrinkage. Stress induced shrinkage represents additional shrinkage strains observed in tension stressed concrete due to extreme cracking in concrete under tensile stresses. It was shown that such cracking results in an increase of surface area of concrete to drying and therefore higher shrinkage strains. In fact,

NVC1.5 might have experienced less stress induced shrinkage rather than higher creep compliance. However, due to the possibility of significant experimental variations more experiments are needed to verify this explanation.

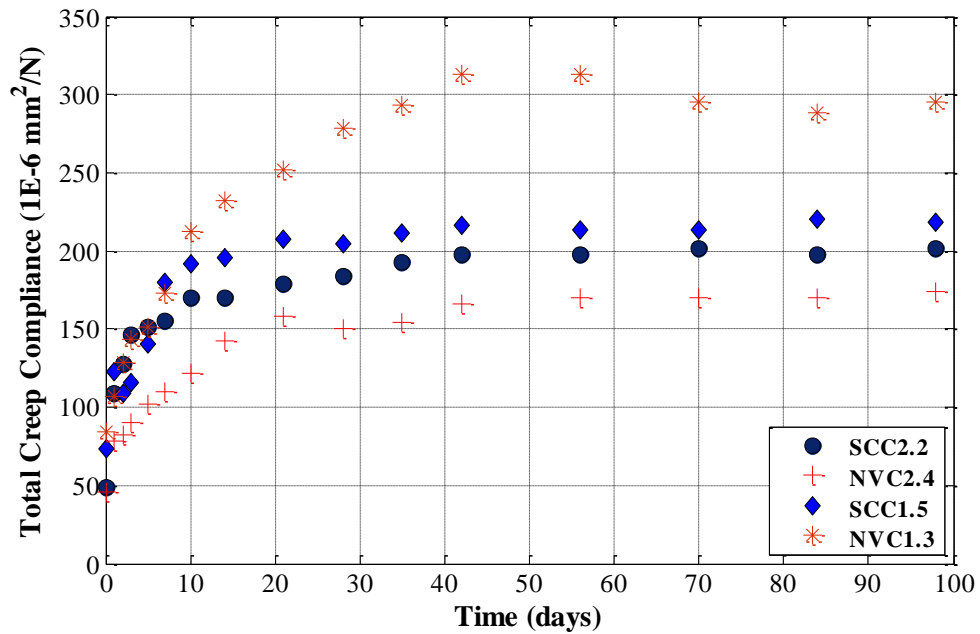


Figure 3.48. Total tension creep compliance of SCC2.0, SCC1.5, NVC2.4, and NVC1.3

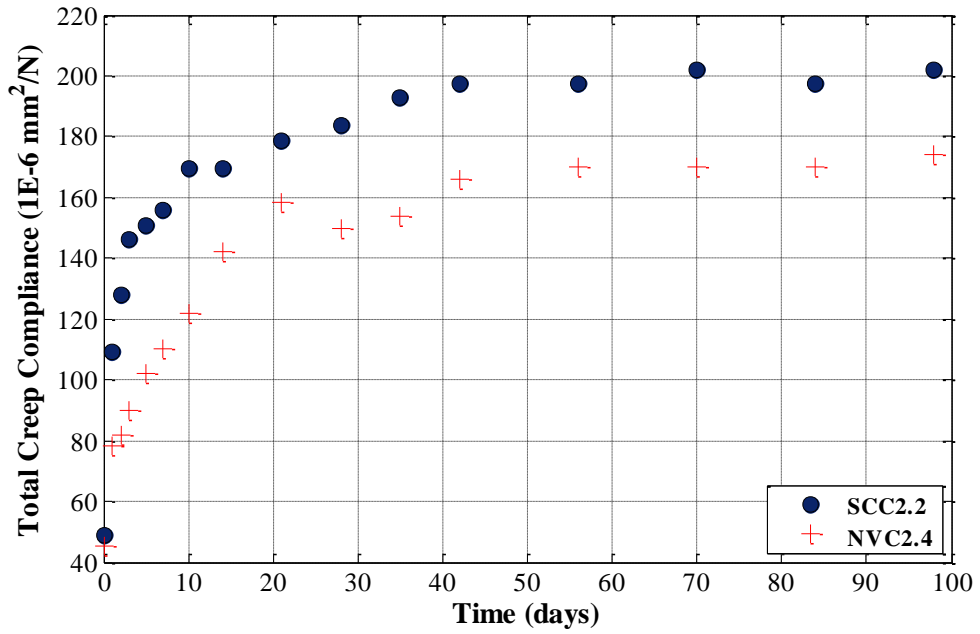


Figure 3.49. Total tension creep compliance of SCC2.2 and NVC2.4

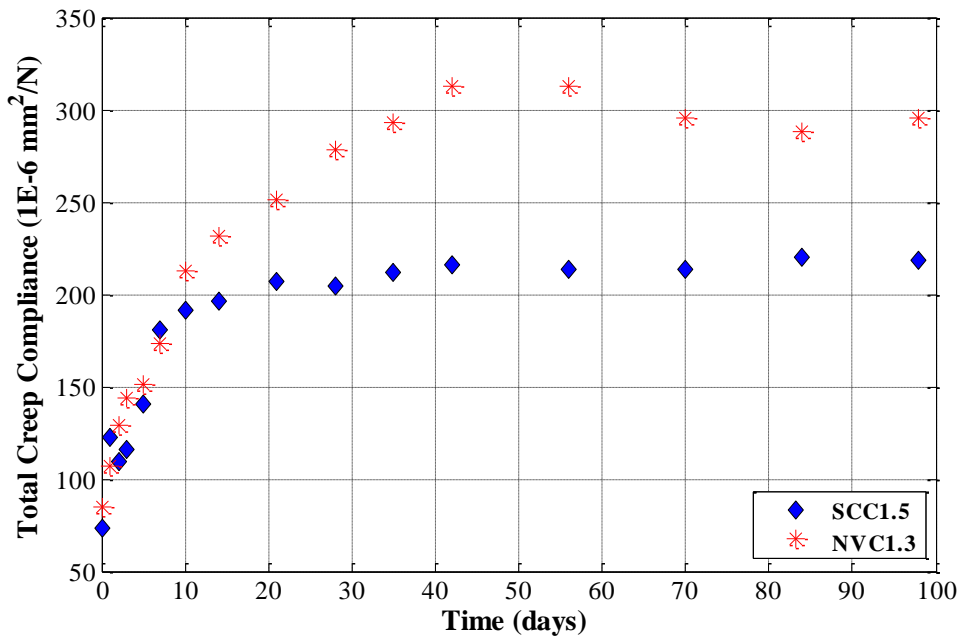


Figure 3.50. Total tension creep compliance of SCC1.5 and NVC1.3

Figure 3.51 shows the basic creep compliance of the SCC and NVC mixes. The loaded wrapped specimen for SCC2.2 failed in the epoxy after only a few hours after loading, damaging the concrete specimen so the basic creep of SCC2.2 is not shown here. The figure shows similar results to those found in the total creep compliance experiments. However, there appears to be less difference between SCC1.5 and NVC1.3. Figure 3.52 shows a comparison of basic creep compliance of SCC1.5 and NVC1.3. This might provide more evidence to suggest that SCC1.5 exhibited higher load induced shrinkage, since little difference was shown in creep compliance when specimens were restricted from water losses.

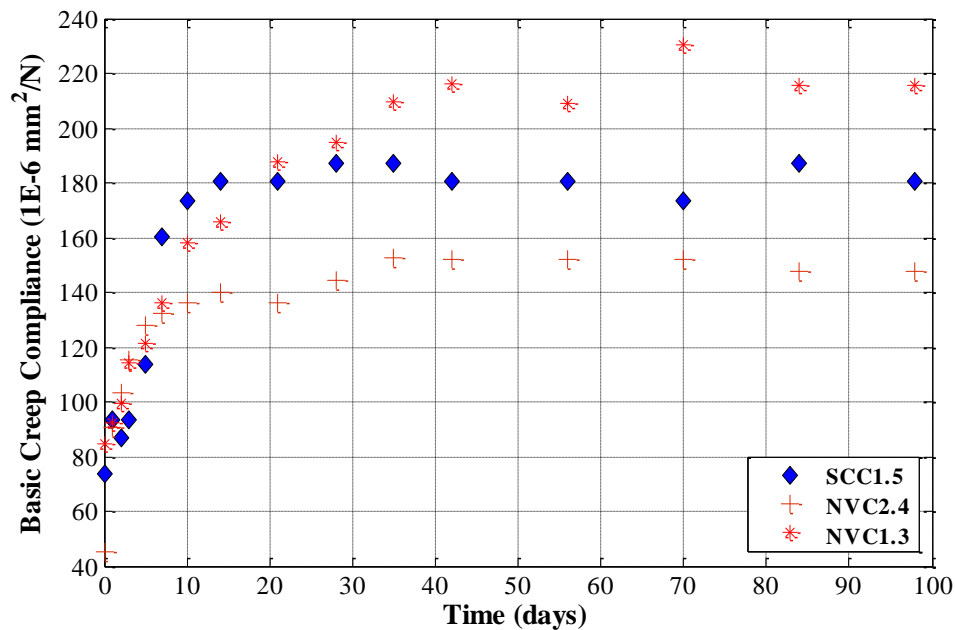


Figure 3.51. Basic tension creep compliance of SCC1.5, NVC2.4, and NVC1.3

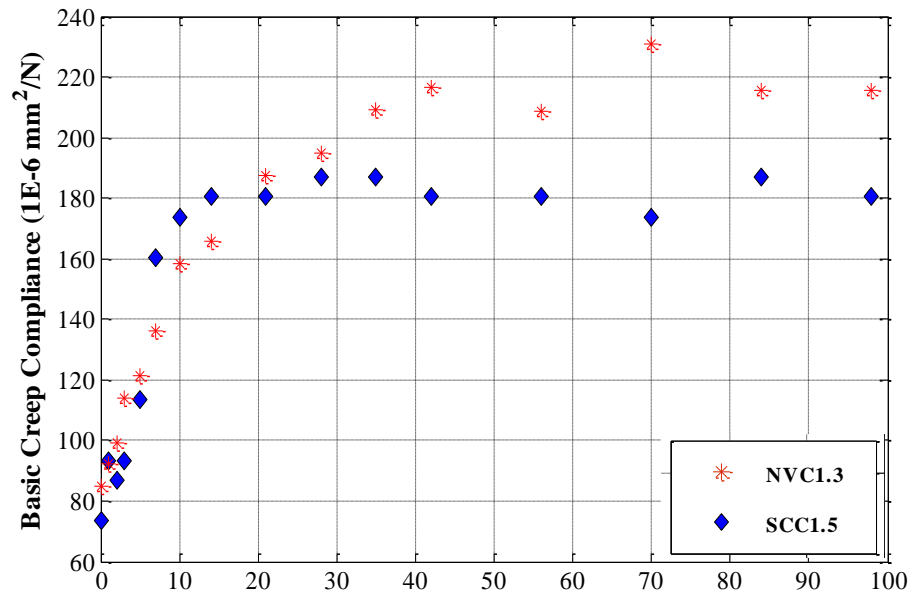


Figure 3.52. Basic tension creep compliance of SCC1.5, NVC2.4, and NVC1.3

CHAPTER 4. NANOSCALE CHARACTERIZATION OF SCC

4.1 INTRODUCTION

This chapter describes the nanoscale experiments performed for this research. The chapter begins by detailing the different materials and mix proportions used for nanoindentation experiments. An overview of the sample preparation and nanoindenter used for this experimental work is also presented. Then the chapter outlines four experimental programs used to characterize self-consolidating concrete (SCC) at the nanoscale using nanoindentation including N1, N2, N3, and N4. The N1 and N2 programs were used to compare nanomechanical response of the cement pastes of SCC and normal vibrates concrete (NVC) mixes. N3 was directed at classifying the mechanical properties of different concrete phases of an SCC mix. Lastly, the N4 program was used to compare the creep response at the nanoscale between a low strength SCC and an ultra high strength concrete. The chapter concludes by presenting the results obtained from the different experiments and a discussion of their significance.

4.2 MATERIALS AND MIX PROPORTIONS

Eight different concrete mixes were selected for the four different experimental programs used for nanoscale characterization of SCC. These include: three NVC mixes, four SCC mixes, and one ultra high performance concrete (UHPC) mix. For the SCC and NVC mixes ordinary Portland cement (ASTM Type I-II) and fly ash (ASTM Class-F) were used as the cementitious materials. Also, for SCC and NVC mixes, washed concrete sand and natural siliceous gravel were used as fine and coarse aggregates respectively. Both aggregates fell within the range of ASTM standards as described in Section 0. As in the macro-creep experiments SCC and NVC mixes contained a water reducer (Glenium3030NS™, BASF Inc) and viscosity modifying agent (VMA362, BASF Inc.).

The UHPC mix included Type I-II Portland cement, nanosilica and densified microsilica (silica fume). Choices of these materials were made for the production of UHPC with adequate workability after Reda et al. [127]. The microsilica used had an average size of 150 μm, while the nanosilica had an average size of 7 nm. For the aggregate, calcined bauxite with a nominal maximum size of 4.75 mm was used. For control of concrete flowability and hardening, superplasticizer (ADA 190™, Grace Inc.) and accelerator (Duraset 400™, Grace Inc.) were used.

Table 4.1. Mix proportions and compressive strength of concrete mixes

	SCC 40	SCC30	SCC17	NVC30	NVC00	UHPC165
<i>Water (kg/m³)</i>	150	150	150	185	140	200
<i>Cement (kg/m³)</i>	360	270	203	289	350	1040
<i>Fly Ash (kg/m³)</i>	90	180	248	97	-	-
<i>Microsilica (kg/m³)</i>	-	-	-	-	-	310
<i>Nanosilica (kg/m³)</i>	-	-	-	-	-	200
<i>CB (kg/m³)</i>	-	-	-	-	-	800
<i>CA (kg/m³)</i>	809	794	780	1143	1090	-
<i>FA (kg/m³)</i>	920	902	886	700	892	-
<i>SP (mL/m³)</i>	7650	4050	4500	1570	-	1500
<i>VMA (mL/m³)</i>	4140	1800	1800	-	-	-
<i>ACC(mL/m³)</i>	-	-	-	-	-	1000
<i>w/b ratio</i>	0.33	0.33	0.33	0.48	0.40	0.15
<i>7 Day f'_c [22]</i>	34.6	13.9	11.0	13.1	-	138
<i>28 Day f'_c [22]</i>	42.6	28.9	17.4	30.2	-	165

CB Calcined Bauxite; *CA* Coarse Aggregate; *FA* Fine Aggregate; *SP* Superplasticizer; *VMA* Viscosity Modifying Admixture; *ACC* Accelerator; *w/b* water/binder ratio; f'_c Mean Compressive Strength

4.3 EXPERIMENTAL METHODS

4.3.1 SAMPLES

Two types of samples were examined in this experimental work. These types include cement paste samples comprised of the same concrete mix without including any fine or coarse aggregates and concrete samples that include aggregate. Cement paste samples were cast into 50 mm x 50 mm x 50 mm cubes and concrete samples were cast into cylinders and prisms as outlined in Sections 3.3.2.3 and 3.4.2.3. All specimens were allowed to set in the molds for 24 hours and then placed into a standard lime-water curing bath (as described in Section 3.3.2.3). Specimens remained in the curing bath until the time they were prepared for indentation. After curing, the specimens for nanoindentation were prepared by slicing 25 mm x 25 mm x 10 mm sections with a diamond blade saw.

4.3.2 SAMPLE PREPARATION

Samples used in these experiments were prepared on the day of the nanoindentation experiments. The samples (sliced sections) were first cast in fast set acrylic epoxy. Upon hardening of this epoxy (approximately 20 minutes), the surface sides of the samples were ground using a mechanical polishing wheel, shown in Figure 4.1. The specimens were rinsed continuously with running water during the grinding process. The grit sizes used for grinding were 120, 240, 600, 1000 and 2000 in consecutive order. After completion of the 2000 grit cycle, specimens were rinsed with distilled water and placed in a sonicating bath filled with distilled water for 10 minutes, to displace any lodged particles. The specimens were then polished using the same mechanical polishing wheel fitted with a microcloth impregnated with 0.6 and 0.1 micron diamond pastes consecutively. Again, after this process, samples were rinsed with distilled water and

placed in the sonicating bath. Finally, the specimen was dried using pressurized air and placed into a sealed specimen container until testing to avoid contamination.



Figure 4.1. Grinding of nanoindentation sample

4.3.3 NANOINDENTER

Nanoindentation experiments were performed using a NanoTest™ 600 system from Micro Materials, Inc., Wrexham, UK. This is a pendulum-based depth-sensing system where the sample is mounted vertically and the load is applied electromagnetically as shown schematically in Figure 4.2. The mechanism of nanoindenter operation involves sending an electrical current through the coil to cause the pendulum to rotate about a frictionless pivot so that the diamond probe penetrates the sample surface. Test probe displacement is measured with a parallel plate capacitor achieving a sub-nanometer

resolution. A Berkovich diamond indenter and a spherical diamond indenter were used to perform the indentations presented in this work. The Berkovich diamond tip indenter had a face angle of 65.27° . This indenter has a pyramid shape with a maximum depth of 1800 nm and a pyramid base width of 2000 nm. The spherical indenter diamond tip had a maximum diameter of 50 μm . The indentation process includes loading then unloading the specimen. The load-indentation data for each indentation is then recorded, analyzed and the properties of the material at the nanoscale are identified.

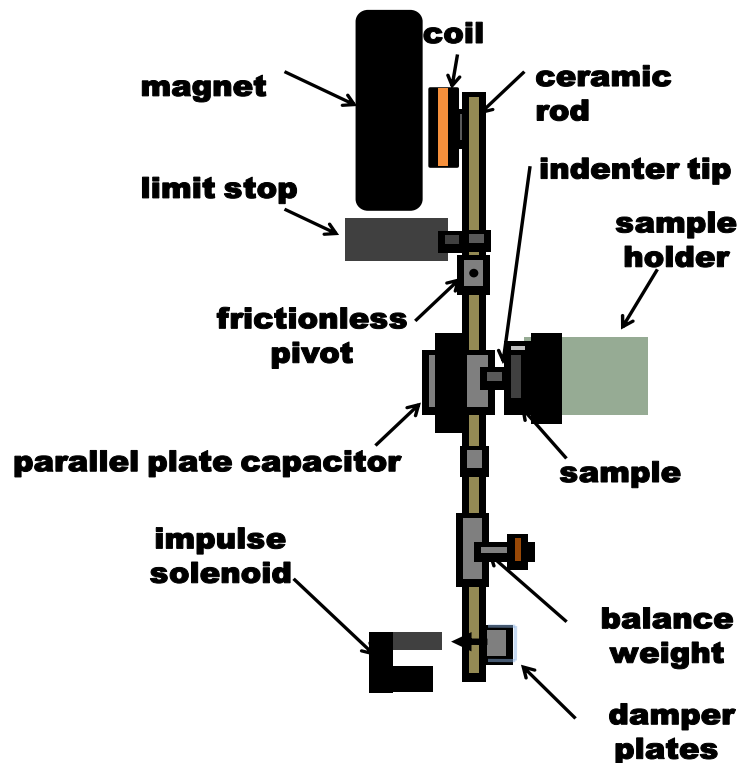


Figure 4.2. Schematic of NanoTest™ 600 system

4.3.4 NANOINDENTATION EXPERIMENTS

4.3.4.1 NANOINDENTATION EXPERIMENTAL PROGRAM NI

The purpose of this experimental program is to determine the effects of chemical admixtures (viscosity modifying agent (VMA) and superplasticizer) on the nanoscale. More specifically the goal of this program is to determine whether chemical admixtures change the percentage of formation of low density (LD) and high density (HD) calcium silicate hydrate (C-S-H). Two concrete mixes were chosen, NVC00 and SCC30, to examine possible effects. SCC30 a typical SCC mix contained both VMA and superplasticizer, while the NVC00 mix contained no chemical admixtures. Mix proportions of these mixes are presented in Table 4.1. Cement paste samples of these two mixes were produced, cured in a standard water lime bath and then indented at 7 days of age.

To determine the nanomechanical properties of the two cement paste specimens, indentations were made on two gridlines spaced 30 μm apart. Each gridline contained 20 indentation points of the same load spaced 10 μm apart. Moreover, each gridline was loaded with the different loading value of 0.5 mN and 1 mN. This was done since material properties of non-homogeneous materials are known to be a function of the indentation depth. The spacing of the indents allowed no overlap between individual indentations and ensured that each indentation had no influence on adjacent indentations by considering a spacing of at least 10 times the maximum indentation depth [98]. Figure 4.3 shows a schematic of the nanoindentations made on the cement paste samples.

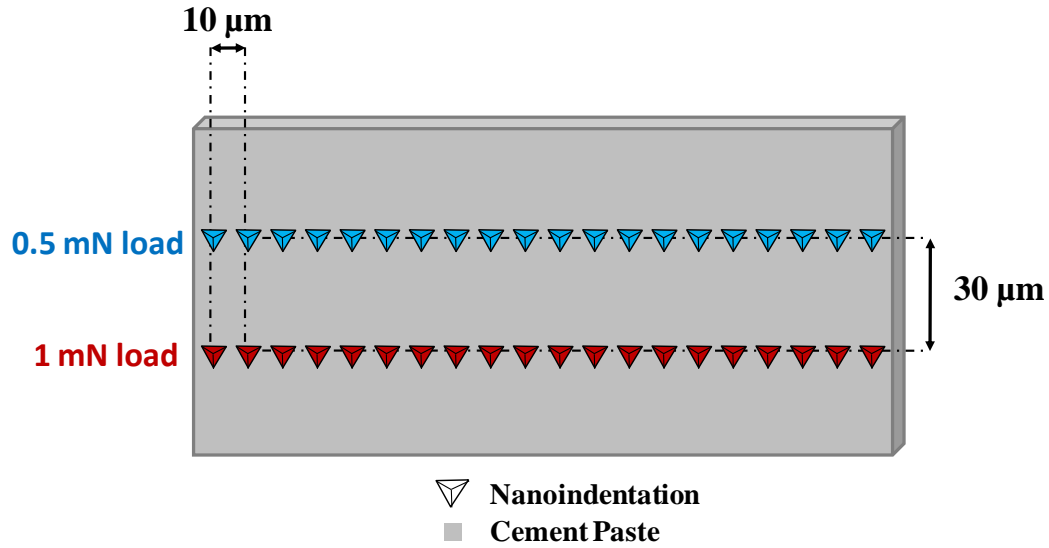


Figure 4.3. Schematic of indentations made on SCC30 and NVC00 cement pastes

The indentation loading and unloading rates were 0.015 mN/s and 0.033 mN/s for the 0.5 mN and 1.0 mN loads respectively. The maximum load was held for a dwell period of 40 seconds to ensure time dependant displacement would not affect unloading data. The variable loading rates kept the total time of each indentation cycle constant at 106 seconds. Figure 4.4 shows the loading cycles for indentations made at the three load levels.

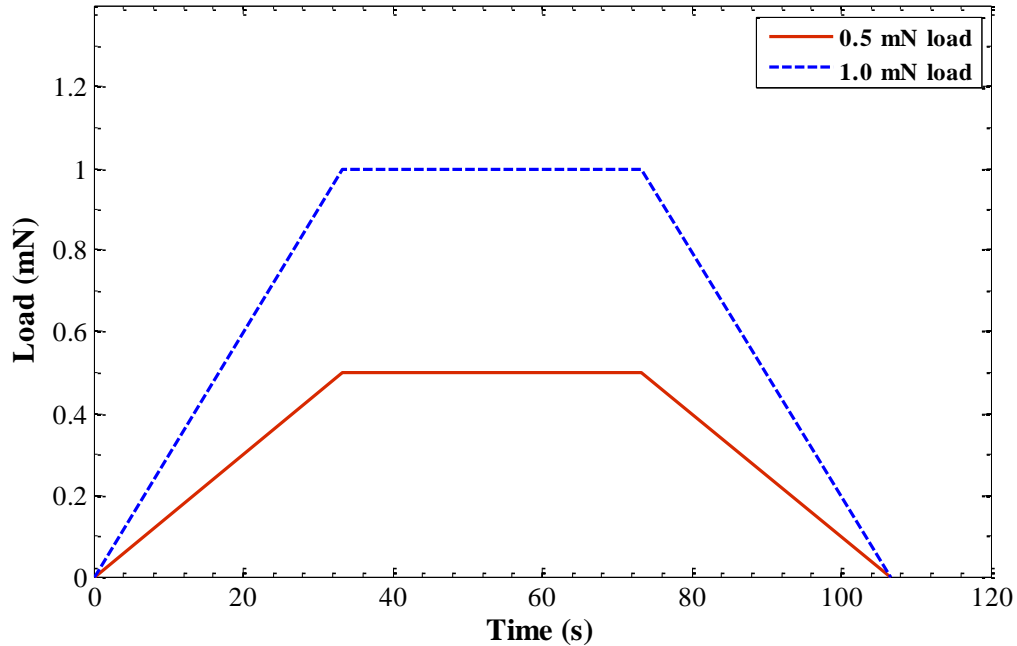


Figure 4.4. Loading cycles for three loads used to indent cement pastes of SCC30 and NVC00

4.3.4.2 EXPERIMENTAL PROGRAM N2

The purpose of this experimental program was to examine nanomechanical properties of an SCC and NVC cement paste that had similar concrete mechanical properties at the macroscale. Moreover, this experiment was used to compare the differences in the nanomechanical response of cement paste indented under wet and dry conditions. SCC30 and NVC30 were chosen for this experimental program. These mixes were used in the macroscale creep experiments presented in Chapter 3. Cement paste samples of the two mixes were indented at 11 days. This time was chosen since macrocreep samples of the concrete mixes were produced, cured in a standard water lime bath and kept in wet conditions and then indented at 11 days of age.

In this experiment, indentations were made on three gridlines spaced 30 μm apart. Each gridline contained 10 indentation points of the same load spaced 30 μm apart. Each gridline was loaded with a different loading value of 0.5 mN, 1 mN, and 1.5. Figure 4.5 shows a schematic of indentations made on the cement paste samples.

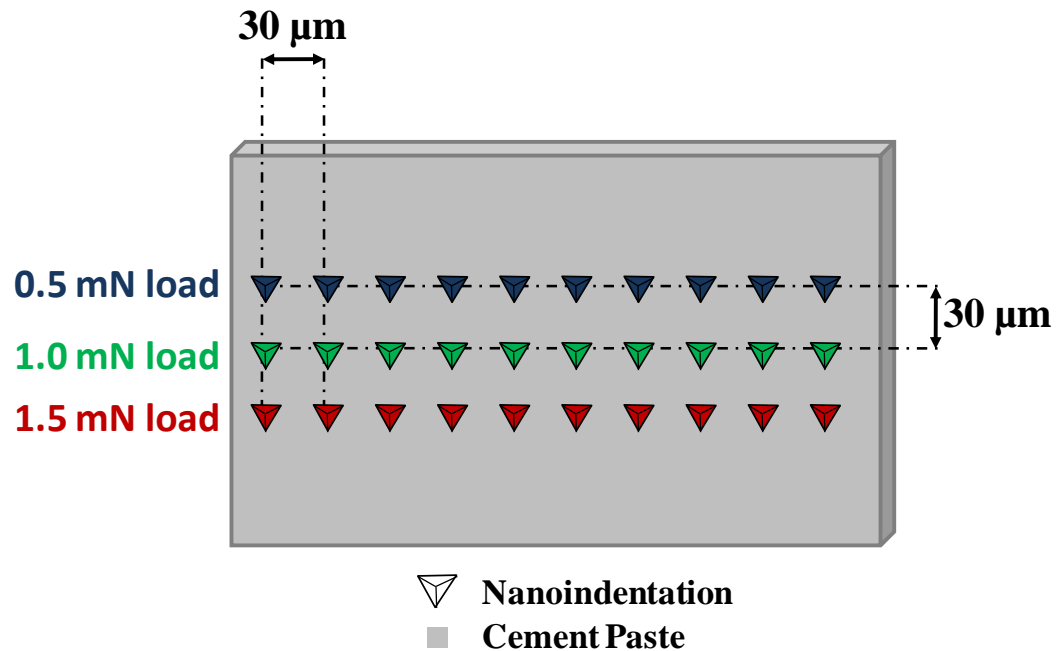


Figure 4.5. Schematic of indentations made on SCC30 and NVC00 cement pastes

To discern the difference between dry cement paste and cement paste at 100 relative humidity specimens were indented while saturated in water. Wet nanoindentation required placing specimen in a sample holder fitted with a capsule (Wet Stage set up from Micro Materials Ltd.) filled with a reservoir of distilled water keeping the specimen saturated throughout the nanoindentation program. Figure 4.6 shows a schematic of the sample holder with the “wet stage” setup fitted on the sample holder. After performing indentations using the wet stage, the set up was removed and specimens were allowed to

air dry for 3 hours before performing indentations under dry conditions. Dry indentations were performed on the same specimens but at another location far from that indented under wet conditions.

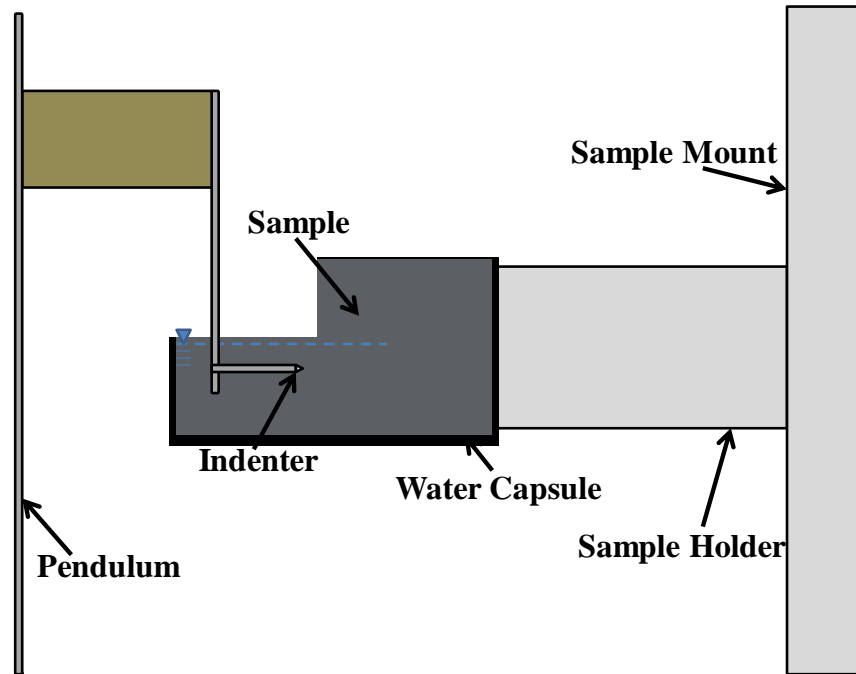


Figure 4.6. Schematic of wet stage indentation experiments

The nanoindentation loading and unloading rate was kept at 0.5 mN/s for all three indentation loads. The maximum load was held for a dwell period of 180 seconds to extract the time dependent displacement data of the two cements pastes. To correct for thermal drift, dwell data was collected for 40 seconds prior to each loading cycle. This was then subtracted from the time displacement data to eliminate thermal drift effects. Figure 4.7 shows the loading cycles for indentations made at the three load levels.

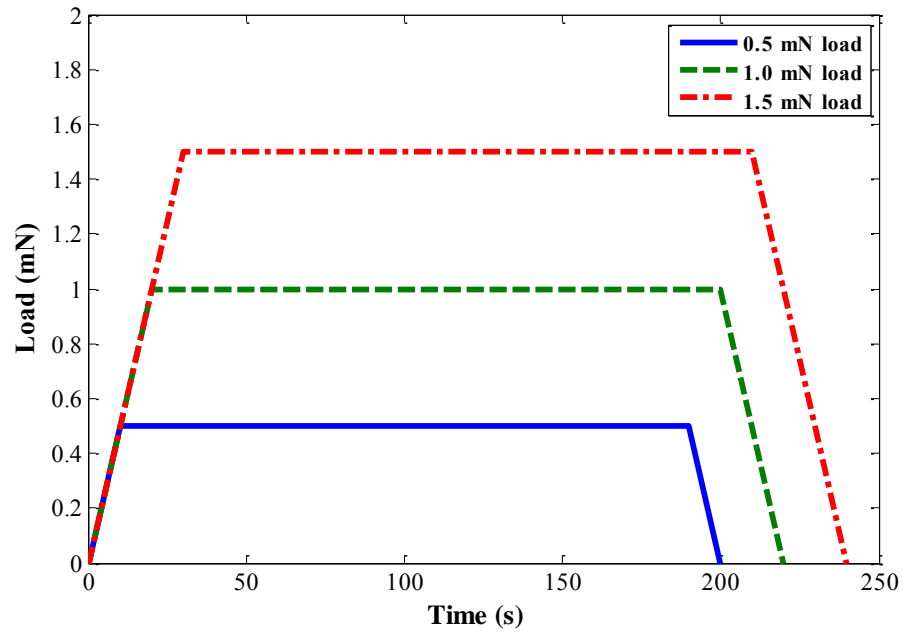


Figure 4.7. Loading cycles for three loads used to indent cement pastes of SCC30 and NVC30

4.3.4.3 EXPERIMENTAL PROGRAM N3

The purpose of this experimental program was to extract the nanomechanical properties of the different microstructural phases of an SCC concrete (i.e. aggregate, cement paste phases (C-S-H), interfacial transition zone (ITZ)). For this experiment SCC40, a typical SCC mix, was used. This mix had a mean compressive strength of 35 MPa and 43 MPa at 7 and 28 days, respectively. The concrete specimen for indentation was extracted from a concrete sample that was cured in a standard water lime bath for 11 days and then kept under laboratory conditions. The sample was prepared and indented at 150 days of age.

Indentation locations on the SCC40 specimen were selected using a high magnification light microscope (1000X) attached to the NanoTest™ 600 platform. An

area on the concrete samples that contained aggregate particles space of approximately 600 μm was chosen for indentation. Indentations were then made along straight line spaced at 20 μm spanning between two aggregate particles (20 indentation points). Indentations were made with a Berkovich indenter to extract nanomechanical properties of each individual phase.

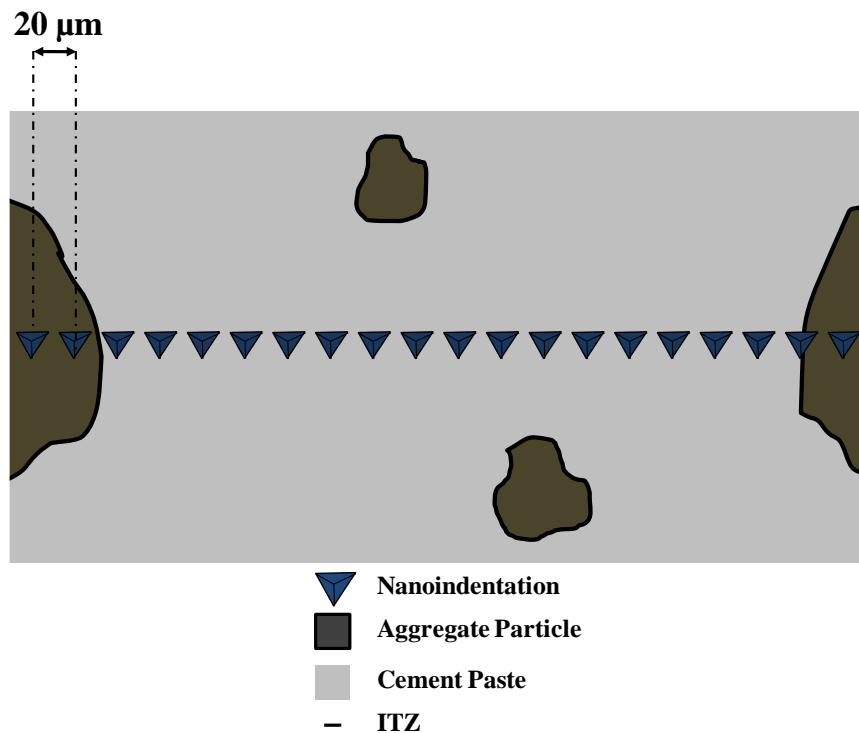


Figure 4.8. Schematic of concrete indentation made along a line using Berkovich indenter

For this experimental program a two condition system was implemented where the loading was stopped when the load reached 25 mN or the indentation depth reached 600 nm. This was performed to account for the extreme heterogeneity of concrete at the nanoscale and the vast difference in mechanical properties between various phases. The depth condition ensured extracting nanoscale properties of different microstructural

phases based on the $\frac{1}{10}$ rule of thumb [9]. Figure 4.8 shows a schematic of a concrete specimen indented in this manner.

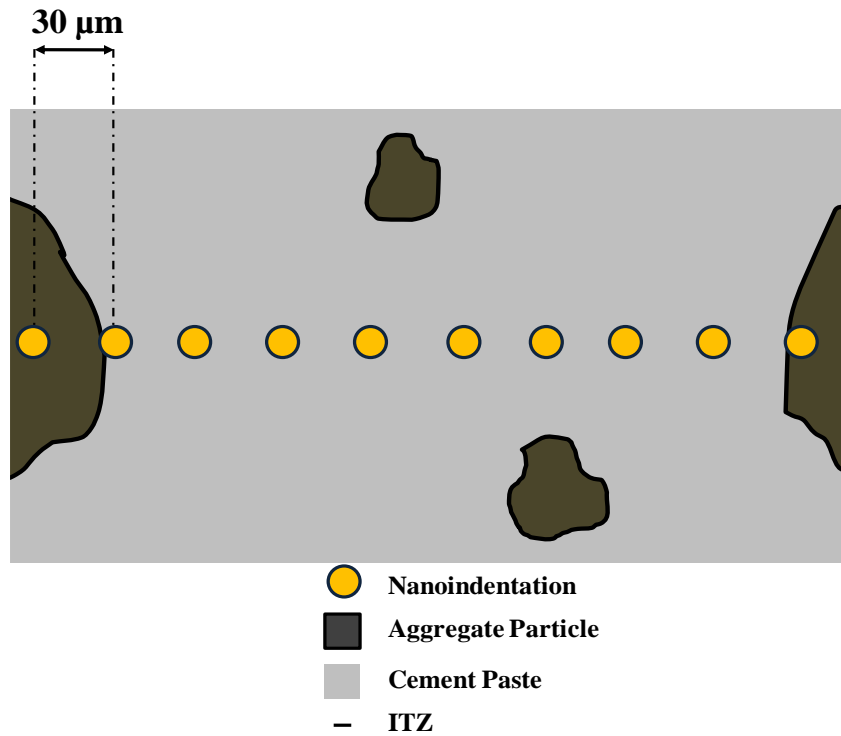
4.3.4.4 EXPERIMENTAL PROGRAM N4

Experimental program N4 was carried out to determine the differences in creep compliance of the cement paste phase of a low strength SCC mix (SCC17) and a UHPC mix (UHPC165). Concrete specimens for this experimental program were extracted from samples cured for 14 days and indented on the 14 day. It is important to note here that the UHPC mixes was cured in a 90 °C water bath and the SCC mix was cured under standard conditions as discussed in Section 4.3.1.

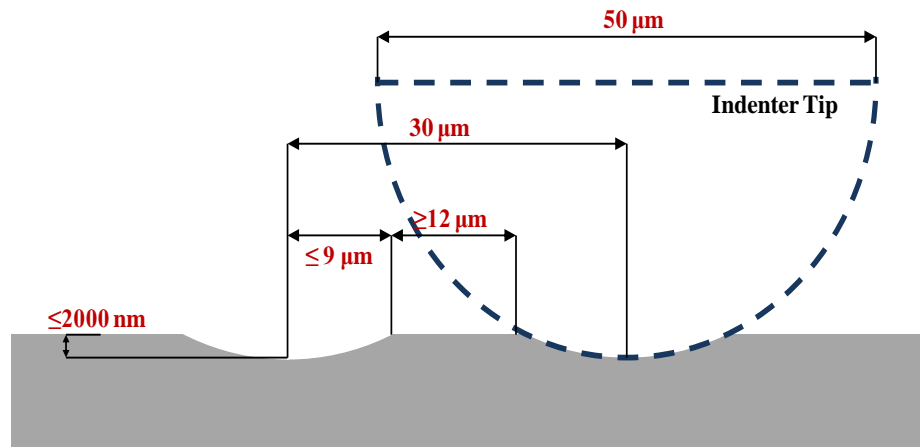
As in experimental program N3, indentation locations on the specimens were selected using a high magnification light microscope (1000X) attached to the NanoTest™ 600 platform. Areas on the samples that contained aggregate particles space of approximately 300 µm were chosen for indentation. Indentations of 0.5 mN were then made along straight lines spaced at 30 µm spanning between two aggregate particles (10 indentation points) using a 50 µm diameter spherical indenter. Two random locations were selected for these lines producing a total of 20 indentation points on each sample. Figure 4.9 (a) shows a schematic of an indentation line made on the two specimens. Since, indentation depths were not allowed to exceed 2000 nm, this allowed for a minimum spacing of 12 µm between indentations ensuring no overlapping of adjacent indentations. Figure 4.9 (b) presents a schematic of the worst case scenario indenter spacing.

It is important to note here the reasons for using a spherical indenter in the N4 experimental program. The spherical indenter covers a large area of material allowing for

observation of the microcomposite's mechanical response at the nanoscale. This is important for nanoscale characterization of heterogeneous materials such as concrete because the significance of interaction of the different phases at the nanoscale might seriously affect the mechanical properties of the composite. The results of this experiment should shed light on the effects of the microstructure on creep of SCC.



(a)



(b)

Figure 4.9. (a) Schematic of concrete indentation made along a line using spherical indenter (b) Spacing between adjacent indentations

The loading and unloading rate used in the indentation cycles was 0.25mN/s. To extract the time dependant properties of the two concretes a dwell period of 120 seconds was implemented upon reaching maximum load. This made for a total loading and unloading cycle of 160 seconds for each indentation, shown in Figure 4.10. To correct for extract thermal drift from creep displacements a post indentation dwell period of 30 seconds was used to extract thermal drift data.

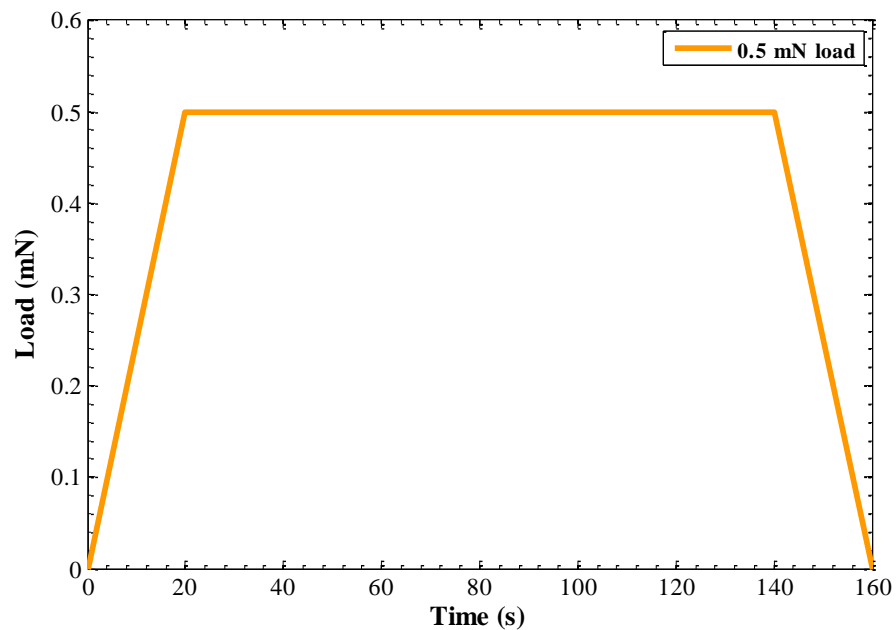


Figure 4.10. Loading cycle indentations made on SCC17 and UHPC165

4.4 ANALYSIS METHODS

4.4.1 BERKOVICH INDENTATION ANALYSIS

The load-indentation data for samples indented with the Berkovich indenter was analyzed using the method outlined by Oliver and Pharr [92]. In this method, properties of indented material were derived from the unloading portion of the load-depth curve gathered during the nanoindentation experiment. This method's major parameters are shown in Figure 4.11.

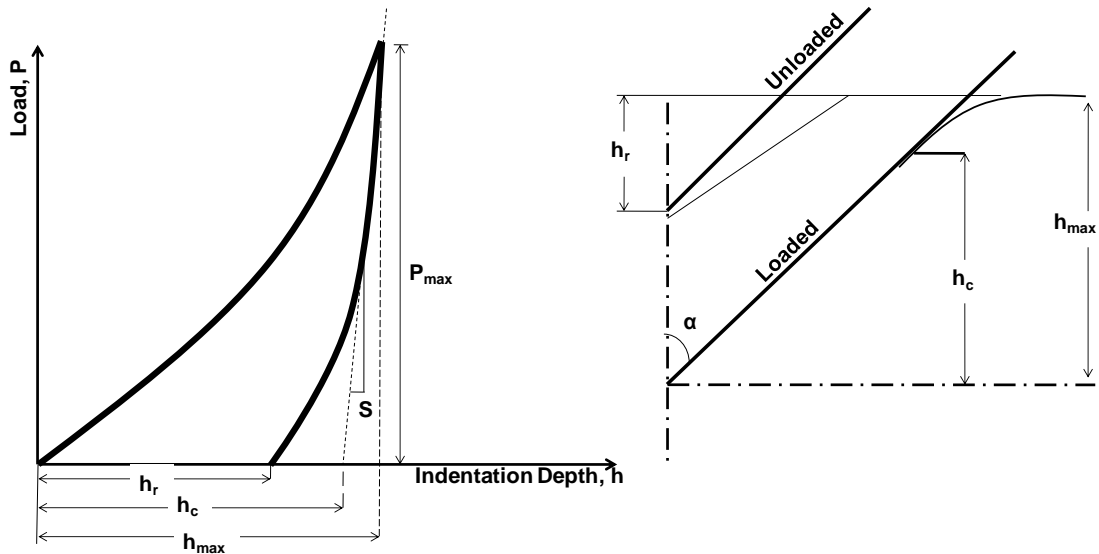


Figure 4.11. Parameters of the Oliver and Pharr method

The total indentation depth h_{max} is defined as the sum of h_c and h_s

$$h_{max} = h_c + h_s \quad (4.1)$$

h_c : indenter contact depth

h_s : displacement at the surface at the perimeter of the indentation

The contact area is then determined by relating the cross-sectional area to h_c . Typically the contact area for a Berkovich indenter A is given as

$$A = 24.5h_c^2 \quad (4.2)$$

h_c : indenter contact depth ($h_{max} - h_s$ from Equation (4.1))

Once the contact area is computed, the hardness of the specimen can then be computed.

The hardness is defined as the ratio of P_{max} to A .

$$H = \frac{P_{max}}{24.5h_c} \quad (4.3)$$

P_{max} : maximum indentation load

Nanoindentation also allows equating the contact stiffness of the indented material to Young's modulus of elasticity. Here the term "reduced modulus" is used in place of Young's modulus to account for the affect of the indenter stiffness on measurements. The reduced modulus E_r can be derived from Equation (4.4).

$$\frac{1}{E_r} = \frac{1 - \nu^2}{E} + \frac{1 - \nu'^2}{E'} \quad (4.4)$$

ν : Poisson's ratio of the indented material

E : Young's modulus of the indented material

ν' : Poisson's ratio of the indenter (0.07)

E' : Young's modulus of the indenter (1141 GPa)

Considering the above relations, E_r can be defined as

$$E_r = \frac{\sqrt{\pi}}{2} \frac{1}{\beta} \left(\frac{S}{\sqrt{24.5h_c^2}} \right) \quad (4.5)$$

β : correction factor (1.034 for the Berkovich indenter [98])

S : contact stiffness

Determining the contact stiffness (S) requires curve fitting of the loading and unloading curves using a power law function. For the unloading portion of the curve the relation can be represented as

$$P = \omega(h - h_r)^2 \quad (4.6)$$

ω : a curve fitting constant

h : indentation depth

h_r : residual indentation depth

Expanding this equation gives a quadratic equation with three constants A , B , and C shown in Equation (4.7).

$$P = A(h)^2 + B(h) + C \quad (4.7)$$

A, B , and C : coefficients determined by fitting the equation to the top 60% of the unloading curve

Then the slope of the unloading curve (S) can be computed as the gradient of the power function at maximum depth.

$$S = \left. \frac{dP}{dh} \right|_{h_{max}} = 2A|h_{max}| + B \quad (4.8)$$

A and B : coefficients determined by fitting the equation to the unloading curve

h_{max} : maximum indentation depth

The elastic, total and plastic work denoted as U_e , U_t and U_p can be defined as the areas under the unloading curves, loading curves and the difference between the loading and unloading curves. These energies can be calculated as

$$U_t = \int_0^{h_{max}} P_L(h) dh \quad (4.9)$$

$$U_e = \int_{h_r}^{h_{max}} P_u(h) dh \quad (4.10)$$

$$U_p = U_t - U_e \quad (4.11)$$

P_L : function representing the indentation loading curve

P_U : function representing the indentation unloading curve

Lee and Radock [128] and Ting [129] showed that indentation experiments can also be used to determine the contact creep compliance. Equation (4.12) describes that the creep compliance under constant stress defined as the ratio of strain as a function of time to the initial applied stress.

$$J(t) = \frac{\epsilon(t)}{\sigma_0} \quad (4.12)$$

$\epsilon(t)$: strain developed with time

σ_0 : initial applied stress

Equation (4.13) can be used to describe the integration to obtain the time-dependent indentation depth $h(t)$ as a function of the applied load P

$$h^2 = \frac{4 \tan^2 \alpha}{\pi} \int_0^t \frac{P}{d} dt \quad (4.13)$$

$h(t)$: nanoindentation depth varying with time

ν : Poisson's ratio

α : indenter surface angle with respect to the vertical axis

J : creep compliance.

Lu et al. [130] showed that the above integration (Equation (4.13)) can be solved by considering a constant loading rate $P = \dot{P} t H(t)$ where \dot{P} is a constant and $H(t)$ is the step function, or under a step loading in the form of $P = P_0 H(t)$ where $H(t)$ is the step function and P_0 is a maximum load. We consider here the case of dwell period loading ($t = 180$ seconds) to be divided into two parts. First, a ramp loading occurring at time period t_1 and is assumed to take place within a very short rise time ($t_1 = 1$ second),

then a constant load afterwards for a time period $t_2 = 179$ seconds. With such consideration, Equation (4.13) can be re-written as

$$J = \frac{4 h^2(t) \tan^2 \alpha}{P_0} \quad (4.14)$$

P_0 : maximum applied indentation load at which the load was kept constant

$h(t)$: nanoindentation depth varying with time

ν : Poisson's ratio

α : indenter surface angle with respect to the vertical axis

A Poisson's ratio of 0.25 based on published cement properties was used for the mortar matrix in both concrete mixes [131]. Nanocrep data was corrected for thermal drift by compensating for thermal drift measurements at very low load where no creep takes place as described by Fischer-Cripps [98].

4.4.2 SPHERICAL INDENTATION ANALYSIS

For analysis of the nanoindentation data gathered from using the spherical indenter, the Oliver and Pharr method was applied to the spherical indenter [98]. This method recognizes the variation of the indented radius with depth. Figure 4.12 shows the major variables used in this analysis.

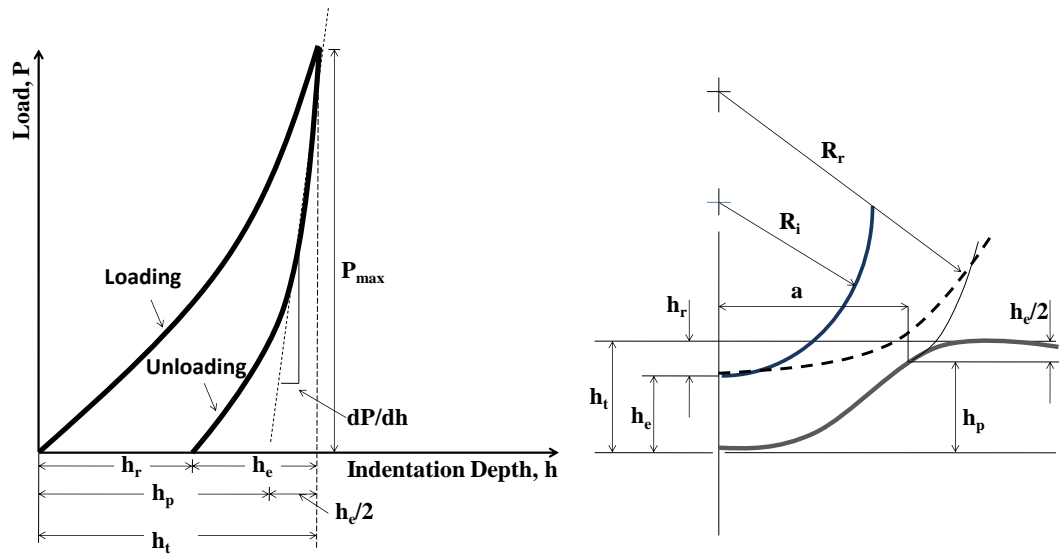


Figure 4.12. Schematic of parameters for spherical indenter

The total indentation depth h_t is the sum of the plastic depth and the half the elastic displacement, shown in Equation (4.15).

$$h_t = h_p + \frac{h_e}{2} \quad (4.15)$$

h_p : plastic indentation depth

h_e : elastic displacement

The elastic displacement h_e is defined in Equation (4.16) (Hertz [132]).

$$h_e = \frac{a^2}{R} \quad (4.16)$$

a : radius of the circle of contact at maximum load

R : relative radius of curvature of the residual impression

Where a can be calculated as a function of the plastic depth and the indenter radius as described by Equation (4.17).

$$a = \sqrt{2R_i h_p} \quad (4.17)$$

R_i : indenter radius (25 μm for this experimental work)

The relative radius of curvature R is defined as

$$\frac{1}{R} = \frac{1}{R_i} - \frac{1}{R_r} \quad (4.18)$$

R_i : indenter radius

R_r : radius of curvature of the residual impression

The contact area A can be calculated from the radius of the circle of contact a . As mentioned earlier, Oliver and Pharr [92] recognized that the unloading curve for a majority of materials indented followed a power fit rather than a strict linear relationship. They noted these phenomena for a Berkovich indenter, but this method can be applied to other indenters. For this work, a power function was fit to top 60% of the unloading curve and the slope of indentation load-depth curve (dP/dh) was calculated as the slope of a line tangent to the power fit relationship or the derivative of the power fit relationship, as described in the Berkovich analysis. Once the contact area and slope were determined, the reduced modulus E_r can be calculated as

$$E_r \left[\frac{dP}{dh} \frac{1}{2a} - \frac{1}{2} \frac{dP}{dh} \frac{\sqrt{P}}{\sqrt{A}} \right] \quad (4.19)$$

A : contact area

a : radius of the circle of contact at maximum load

Lu et al. [130] showed that for a spherical indenter tip the time dependent displacement can be described as

$$h(t) = \frac{3}{8\sqrt{R}} \left[\frac{P_0}{d} \right]^{1/3} J(t) \quad (4.20)$$

$h(t)$: nanoindentation depth varying with time

J : creep compliance.

Tweedie and Van Vliet (2006) [14] showed creep compliance can be deduced from the contact compliance extracted from nanoindentation using spherical indenter tip.

$$J(t) = \frac{8\sqrt{R_i}}{3P_0} \left(1 - \frac{h(t)}{h_0} \right)^{3/2} \quad (4.21)$$

P_0 : maximum applied load at which the load was kept constant

R_i : indenter radius

$h(t)$: nanoindentation depth varying with time

ν : Poisson's (0.25 based on Haecker et al. [131])

4.4.3 STATISTICAL ANALYSIS

4.4.3.1 *STUDENT T-TEST OF MEANS AND ZERO DEPTH REDUCED MODULUS*

To account for the variability of the indentation data, a one tailed student t-test of means was performed to compare the nano-mechanical properties of SCC and NVC. A confidence interval of 90% was employed to determine if the means possessed any significant difference. The use of the student t-test is due to the small populations of mechanical property data.

It has been shown that in materials heterogeneous at the nano and microscales the reduced modulus may vary with indentation depth. Therefore, an equivalent, zero depth reduced modulus was recommended to represent the intrinsic depth-independent properties of materials. This depth-independent Young's modulus of elasticity of cement paste was determined using a linear function to describe the relationship between the maximum indentation depth and the reduced modulus with the objective of identifying Young's modulus of elasticity at zero depth [98].

4.4.3.2 *PHASE RECOGNITION USING STATISTICAL DECONVOLUTION METHOD*

A statistical deconvolution method after Constantinides et al. [9] was employed to separate the mechanical properties of the different microstructural phases encountered in the multiple indentations performed on cement paste with the Berkovich indenter. It was assumed that each indent took place at only a single phase of the cement paste. Based on this assumption the observed experimental frequency density (EFD) can be calculated as the probability density function (PDF) $p(x)$:

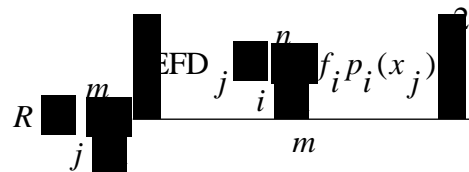
$$p(x) = \sum_{i=1}^n f_i p_i(x) \quad (4.22)$$

f_i : surface fraction occupied by i th phase on the indented surface

$p_i(x)$: PDF of each phase

n : number of phases

The probability $p(x)$ can be deconvoluted into a number of PDFs describing the different microstructural phases ($n p_i(x)$) and the corresponding surface fraction (f_i) of those phases by minimizing the standard error R between EFD and $p(x)$ as



$$R = \sum_{j=1}^m |EFD_j - \sum_{i=1}^n f_i p_i(x_j)| \quad (4.23)$$

EFD_j : experimental frequency density at the j -th bin

$p(x_j)$: value of PDF shown in previous slide at point x_j

m : number of bins used to construct the EFD distribution

This method was applied to nanoindentation observations to extract the mean value of the mechanical properties of the different microstructural phases.

4.5 RESULTS AND DISCUSSION

4.5.1 NANOINDENTATION EXPERIMENTAL PROGRAM N1

A significantly higher indentation depth of SCC compared with NVC was observed in indentation experiments performed at 7 days on SCC30 and NVC00. For both applied indentation loads 0.5 mN and 1 mN SCC30 showed a higher maximum indentation depth. For SCC30 the mean maximum indentation depths were 264 nm and 390 nm for loads 0.5 mN, and 1 mN respectively, while the mean respective depths for the NVC00 samples were 179 nm and 268 nm for the two loads. Based on the student t-test, the mean depths for both loads were found to be significantly different. Figure 4.13 displays a comparison between the indentation depth of SCC30 and NVC00 cement pastes at 1 mN load. In Figure 4.13, the probability represents the likelihood of having a given value with the given mean and standard deviation calculated using the normal probability mass function.

The mean hardness of SCC30 showed to be significantly less than NVC00 at 1mN. However, no difference was observed in the hardness of both materials at the 0.5 mN load. Figure 4.14 shows a comparison of values of hardness for SCC30 and NVC00 at the 0.5 mN indentation load. The figure also shows the results of the student t-test where no significant difference was found between the mean hardness of the two samples at the given load. The mean hardness values for SCC30 at loads of 0.5 mN and 1 mN were 0.98 GPa and 0.43 GPa respectively. The mean hardness for NVC00 at these same loads was 0.82 GPa and 0.81 GPa respectively.

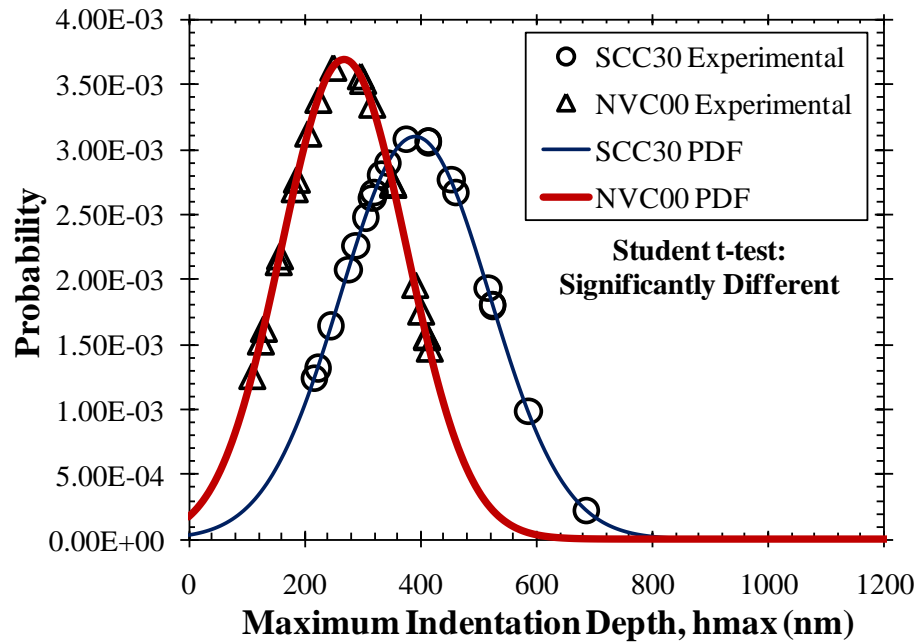


Figure 4.13. Comparison of maximum indentation depth between SCC30 and NVC00 at 1mN load

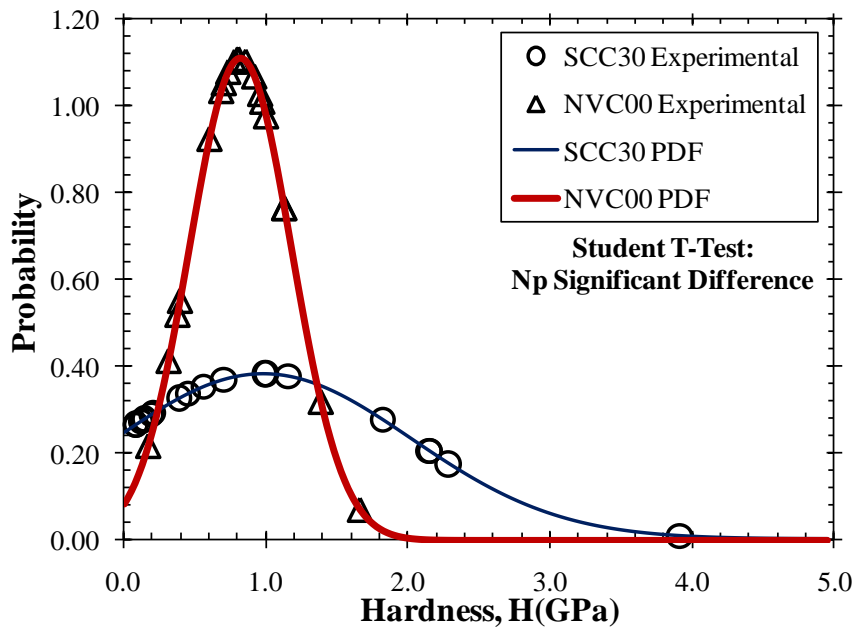


Figure 4.14 Comparison of hardness between SCC30 and NVC00 at 0.5 mN load

The two cement pastes showed no significant difference in their reduced modulus at a load of 1 mN but showed a significant difference in reduced modulus at a load of 0.5 mN. Figure 4.15 shows a comparison of reduced modulus obtained from experiments with a load of 0.5 mN where the student t-test of means yielded a significant difference. The mean reduced modulus values found for SCC30 were 22.5 GPa and 18.2 GPa, in order of increasing load. On the other hand, the mean reduced modulus values of the NVC00 mix were 16.1 GPa and 14.2 GPa, in order of increasing load. In general, as the load increased the reduce modulus decreased. This occurs because reduced modulus is an inverse function of indentation depth, thus the higher the load the higher the maximum depth of indentation resulting in a lower reduced modulus. Therefore, it is recommended to extract a load and depth-independent reduced modulus. A statistical procedure for extracting load independent reduced modulus is suggested by Kim et al. [133].

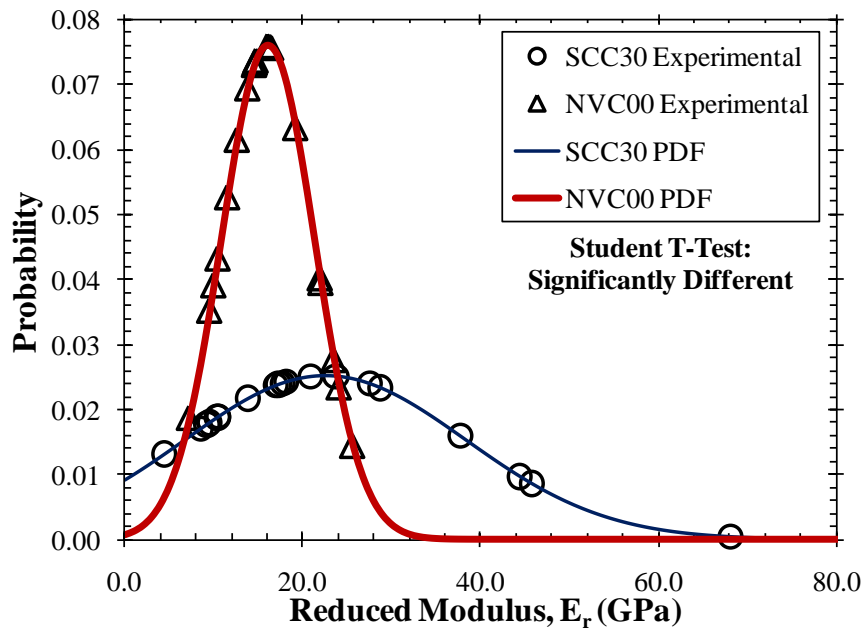


Figure 4.15. Comparison of reduced modulus between SCC30 and NVC00 at 0.5 mN load

The limited number of experiments for the two different loads might not provide enough information to draw general conclusions. However, it is evident that the SCC30 mix examined here was softer than the NVC00 mix. SCC30 showed a significantly higher indentation depth for both loads and a significantly lower hardness and reduced modulus for at 1 out of the 2 loads used for the experiment. Therefore, the presence of superplasticizers, VMA, and fly ash in the SCC mix significantly weakened the microstructure of the cement paste. However, since the compressive strength of the NVC00 mix was not found, it cannot be ruled out that a possible higher compressive strength for NVC00 could be the reason SCC30 was softer.

To investigate any possible changes in the distribution of LD and HD C-S-H a deconvolution analysis after Constantinides et al. [9] was performed. Figure 4.16 and Figure 4.17 show the experimental data points and the combined PDF's of LD and HD C-S-H for SCC and NVC at indentation loads of 0.5 mN and 1.0 mN respectively. Since the maximum depths of indentation were all less than 700 nm, we can say with confidence that all reduced modulus measurements represent a single phase. The figures clearly show a difference in the distribution of LD and HD C-S-H, however a statistical difference was not always found. Clearly, the use of fly ash, VMA, and high amounts of superplasticizer altered the distribution of LD and HD C-S-H. This might be due to a difference in C-S-H formed as a result of pozzolanic reactions instead of normal cement hydration. However, due to the low number of measurements and high number of variables, more experiments are needed to confirm this hypothesis.

Table 4.2 presents the mean, standard deviation and fraction of reduced modulus of LD and HD C-S-H for SCC30 and NVC00. Figure 4.18 and Figure 4.19 show representative load-indentation curves for LD and HD C-S-H encountered when indenting SCC30 and NVC00 at the 0.5 mN and 1.0 mN loads.

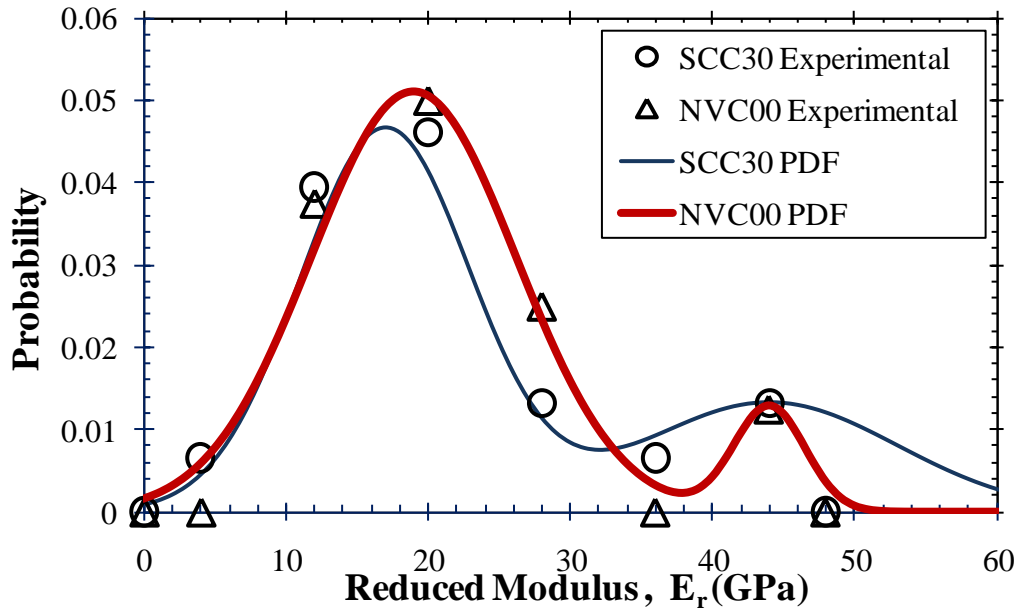


Figure 4.16. Experimental and theoretical PDFs of LD and HD C-S-H for SCC30 and NVC00 at 0.5 mN load

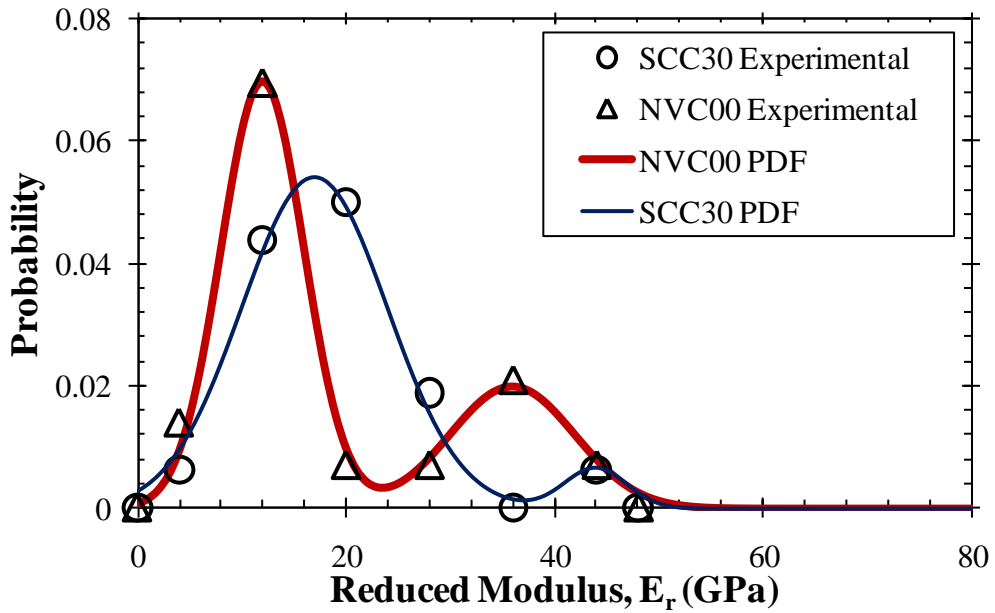


Figure 4.17. Experimental and theoretical PDFs of LD and HD C-S-H for SCC30 and NVC00 at 0.5 mN load

Table 4.2. Mean, standard deviation of reduced modulus and surface fraction of LD and HD C-S-H for SCC30 and NVC00

		LD C-S-H			HD C-S-H		
		Mean (GPa)	Std. (GPa)	Fraction	Mean (GPa)	Std. (GPa)	Fraction
SCC30	0.5 mN	17	6	0.70	44	9	0.30
	1.0 mN	17	7	0.95	44	3	0.05
NVC00	0.5 mN	19	7.2	0.92	44	2.5	0.08
	1.0 mN	12	4	0.70	36	6	0.30

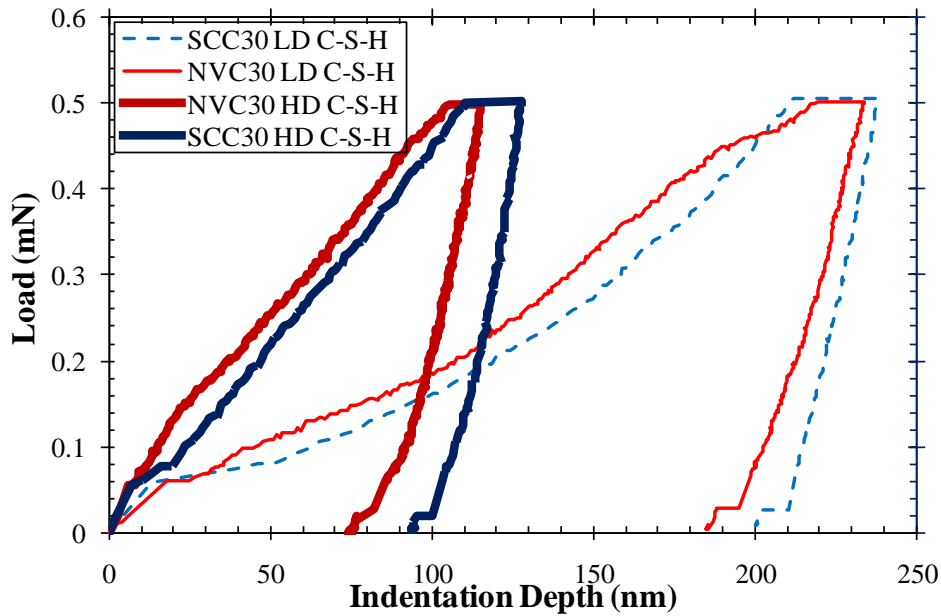


Figure 4.18. Representative load-indentation curves of SCC30 and NVC30 LD and HD C-S-H indented at 0.5 mN load

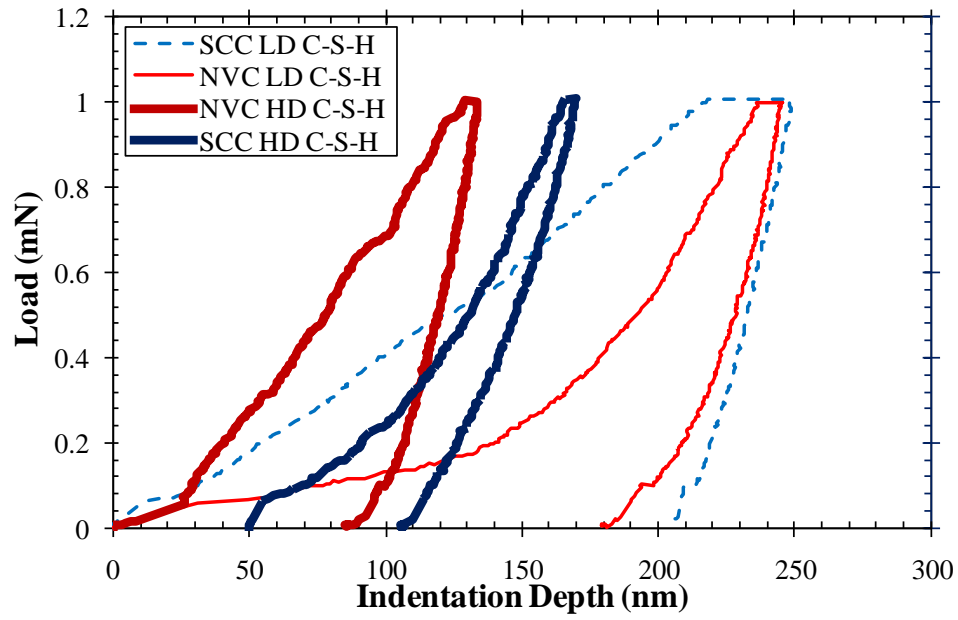


Figure 4.19. Representative load-indentation curves of SCC30 and NVC30 LD and HD C-S-H indented at 1.0 mN load

4.5.2 NANOINDENTATION EXPERIMENTAL PROGRAM N2

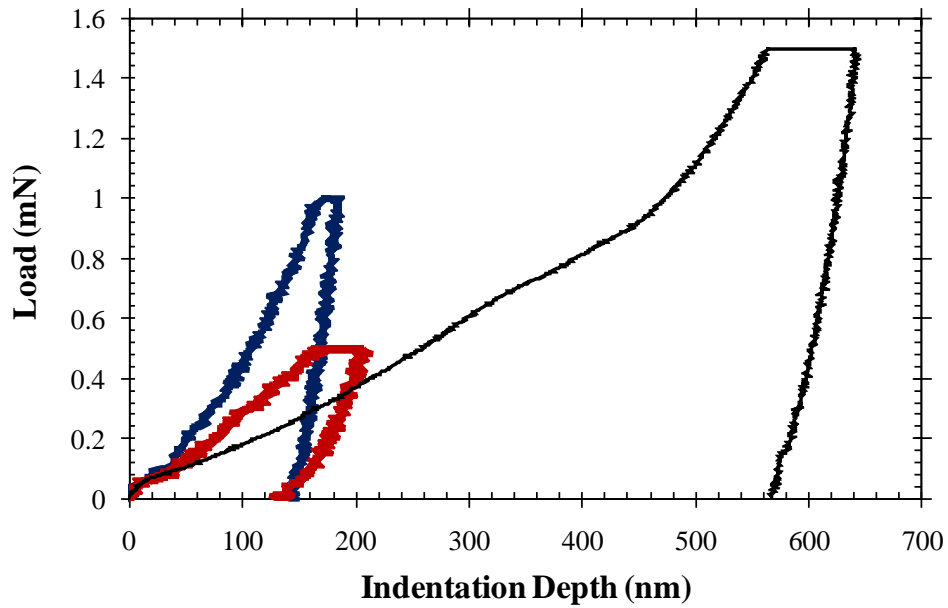


Figure 4.20. Representative curves of indentations made on SCC30 at loads of 0.5 mN, 1.0 mN and 1.5 mN

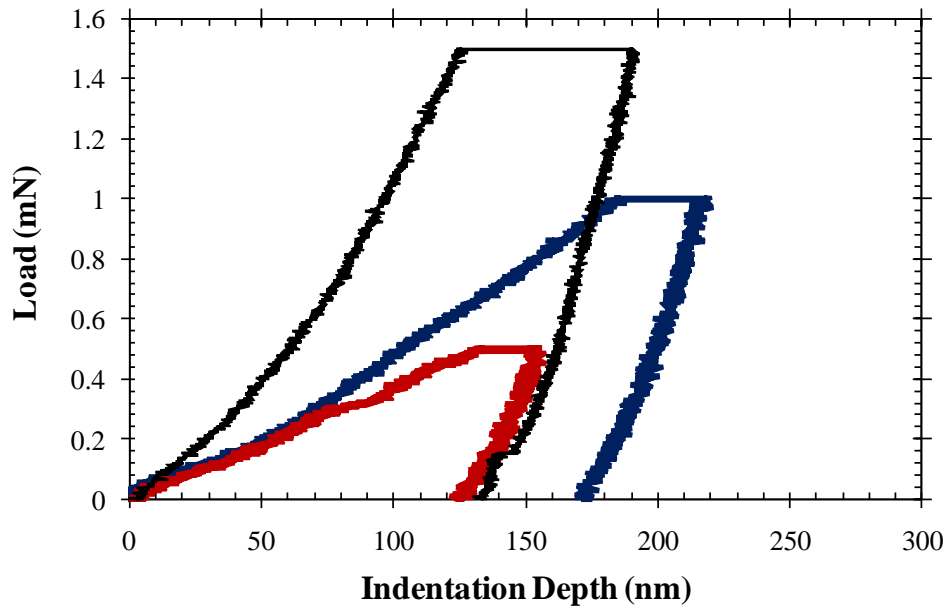


Figure 4.21. Representative curves of indentations made on NVC30 at loads of 0.5 mN, 1.0 mN and 1.5 mN

To examine the nanoscale properties of two concretes with similar macroscale properties, indentations were performed on SCC30 and NVC30 cement pastes at 11 days. Both these mixes showed a very similar compressive strength at 11 days age. SCC30 had an 11 day compressive strength of 17 MPa, while NVC30 had an 11 day compressive strength of 19 MPa. Although, SCC30 showed similar macroscale compressive strength as compared with NVC30, the SCC30 mix showed significantly different nanoscale properties including maximum indentation depth. Figure 4.20 and Figure 4.21 show representative load-indentation curves for indents made on SCC30 and NVC30 cement pastes at the three loads. SCC showed a significantly higher maximum depth for all three loads, 0.5 mN, 1 mN, and 1.5 mN. Figure 4.22, Figure 4.23, and Figure 4.24 show a comparison of maximum depth and the results of a student t-test of means for all three indentation loads.

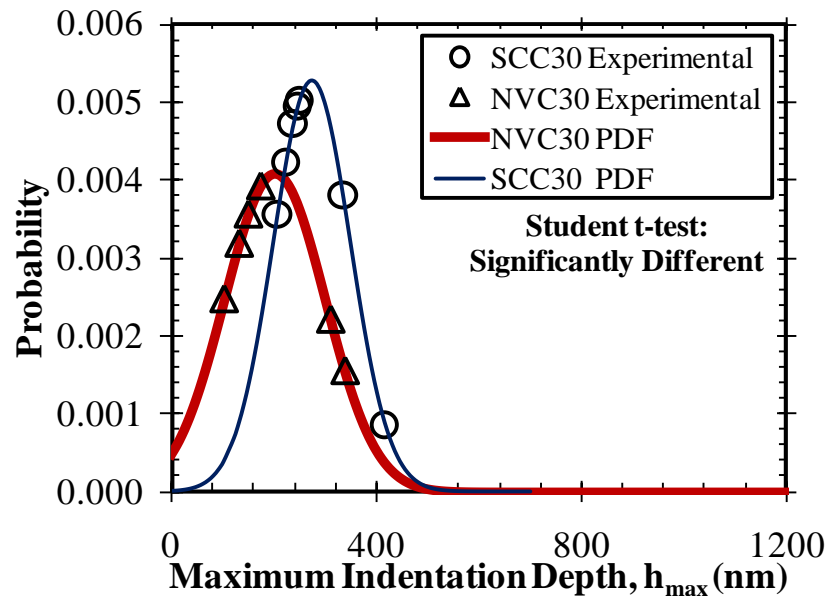


Figure 4.22. Comparison of maximum indentation depth between SCC30 and NVC30 at 0.5mN load

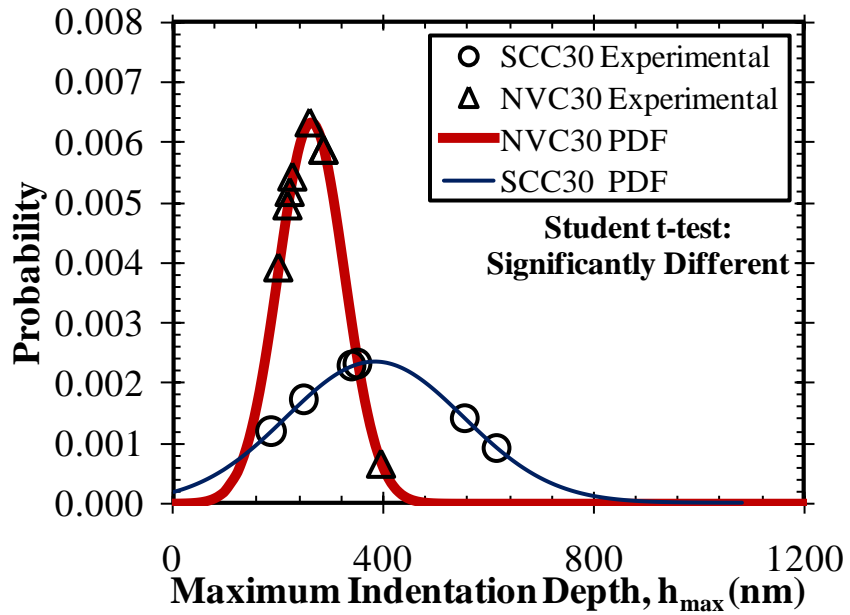


Figure 4.23. Comparison of maximum indentation depth between SCC30 and NVC30 at 1.0 mN load

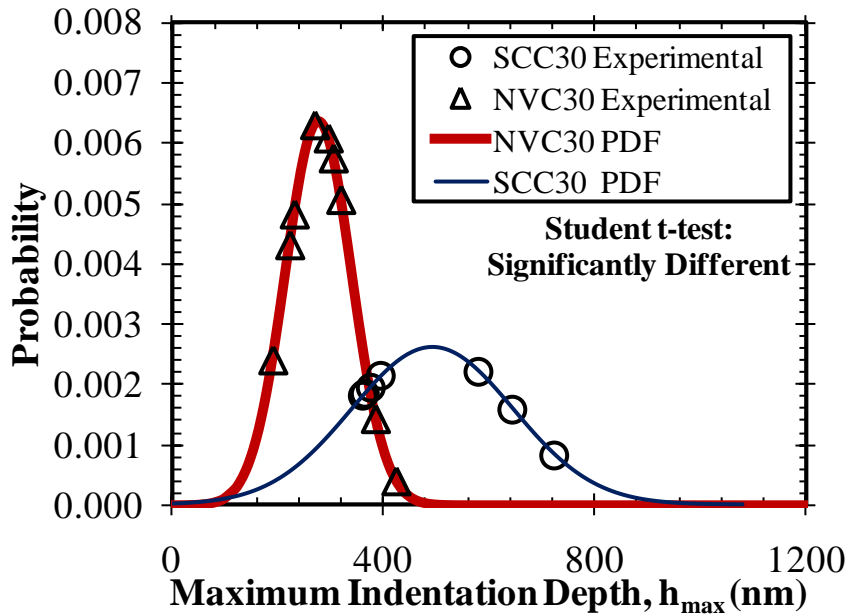


Figure 4.24. Comparison of maximum indentation depth between SCC30 and NVC30 at 1.5 mN load

NVC30 also showed to have a superior stiffness at the nanoscale in comparison with SCC30. The SCC30 mix was found to have a significantly lower reduced modulus at all three loads. Figure 4.25, Figure 4.26 and Figure 4.27 show a comparison of the reduced elastic modulus of SCC30 and NVC30 at loads of 0.5 mN, 1.0 mN, and 1.5 mN respectively.

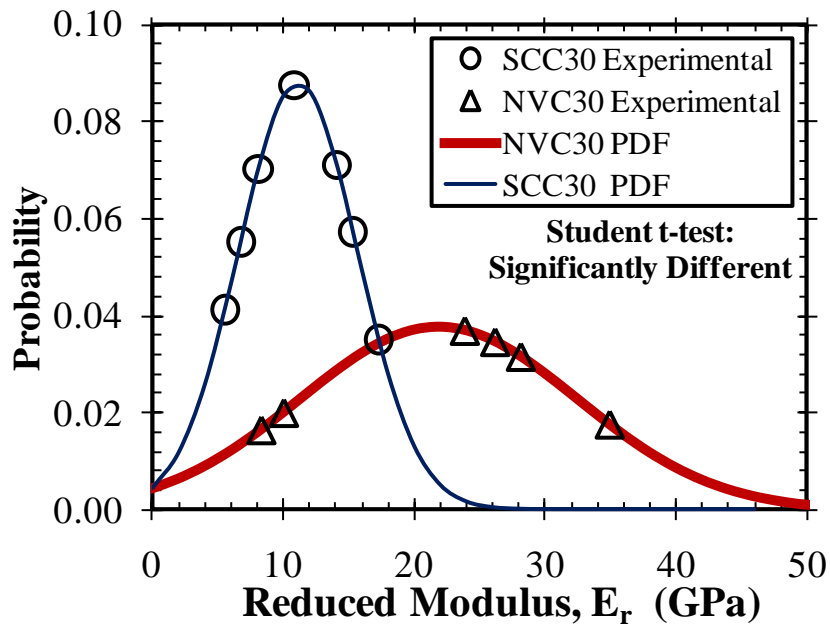


Figure 4.25. Comparison of reduced modulus between SCC30 and NVC30 at 0.5 mN load

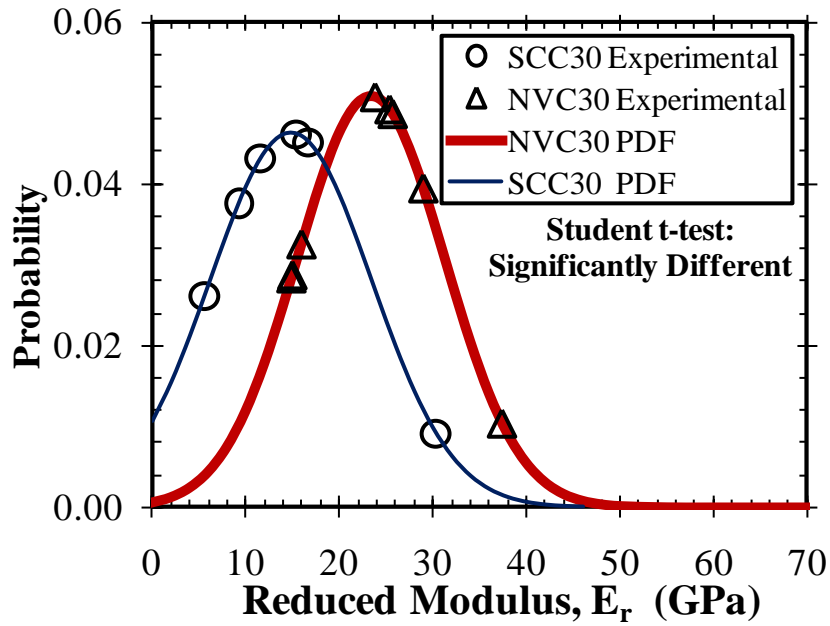


Figure 4.26. Comparison of reduced modulus between SCC30 and NVC30 at 1.0 mN load

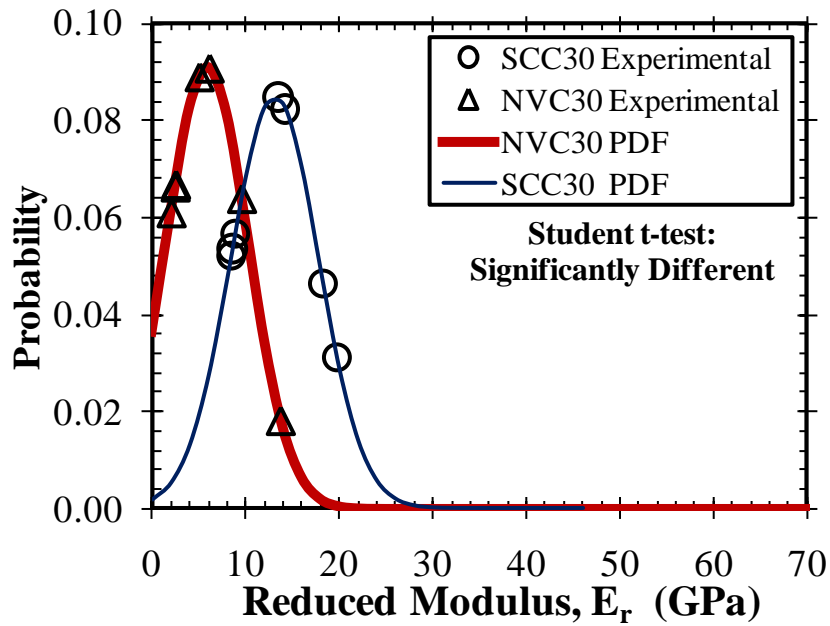


Figure 4.27. Comparison of reduced modulus between SCC30 and NVC30 at 1.5 mN load

A zero depth reduced modulus was deduced using a pre-assumed linear relationship. The zero depth reduced modulus was found to be lower for SCC at value of 20.2 GPa as compared with 38.9 GPa for NVC. Figure 4.28 and Figure 4.29 show the maximum depth plotted against the reduced modulus and the zero depth modulus based on a linear interpretation of the data for SCC30 and NVC 30 respectively. Investigations of these figures might show that the linear relation with indentation depth might not be accurate. However, in both cases the reduced modulus clearly decreases with increasing maximum indentation depth. This suggests that this method of zero depth reduced modulus should be a good indicator of the intrinsic reduced modulus of the material before penetration of the indenter. A probabilistic approach, recently suggested by Kim et al. [133] for determining zero depth or zero load reduced modulus, might be able to yield better results.

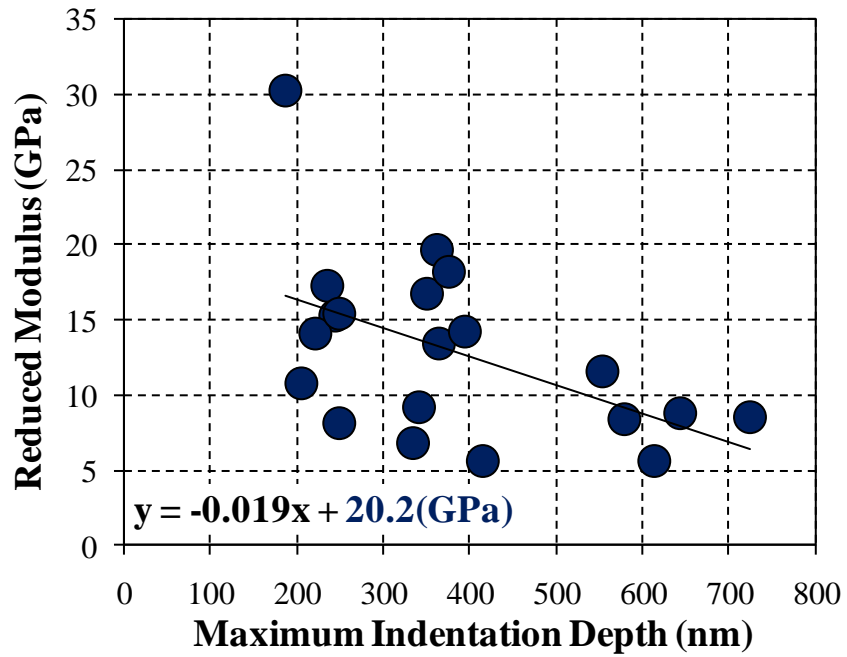


Figure 4.28. Zero depth reduced modulus for SCC30

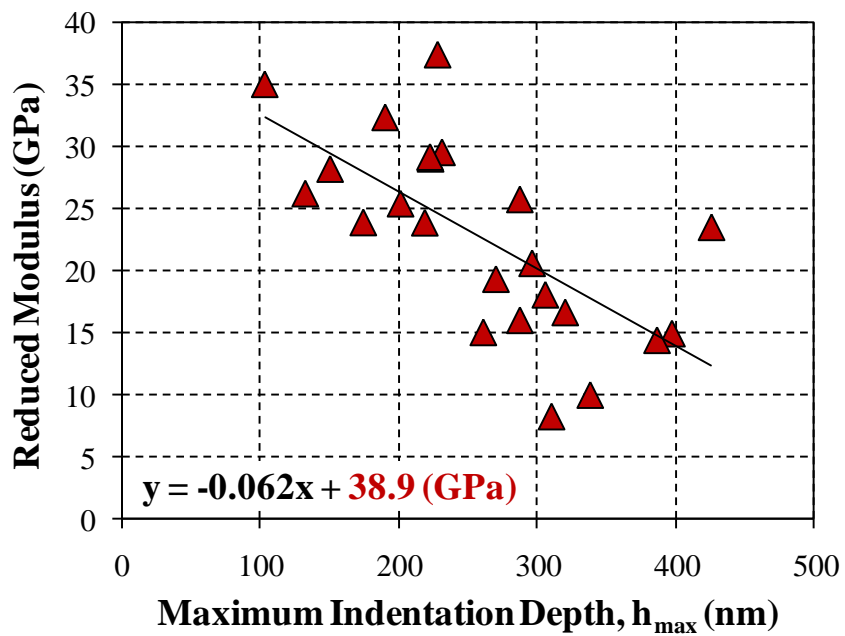


Figure 4.29. Zero depth reduced modulus for NVC30

A significant difference in hardness was observed at loads 0.5mN and 1.5mN. The difference in hardness between NVC and SCC at 1 mN was not significantly different statistically based on the 90% confidence interval. Figure 4.30, Figure 4.31, and Figure 4.32 present comparisons of the hardness of SCC30 and NVC30 at loads of 0.5 mN, 1.0 mN, and 1.5 mN respectively.

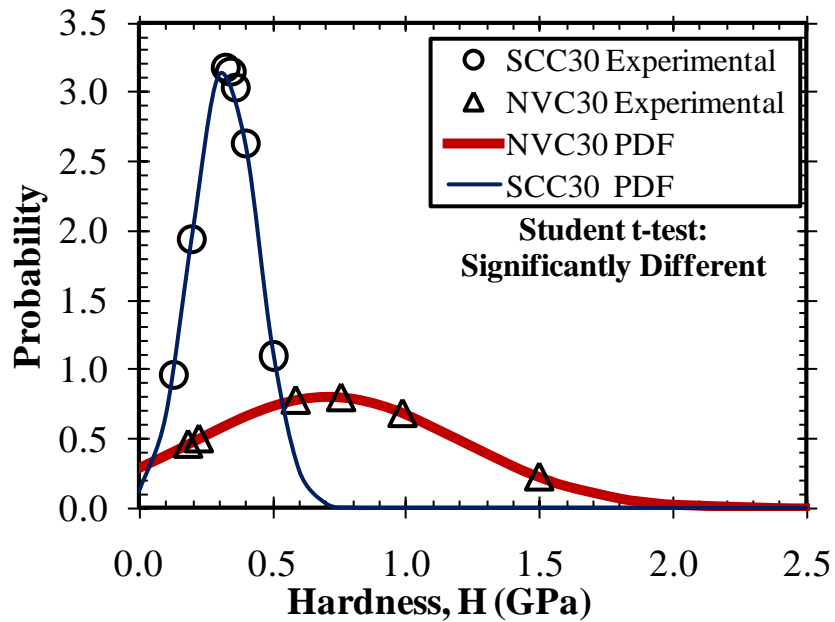


Figure 4.30. Comparison of hardness between SCC30 and NVC00 at 0.5 mN load

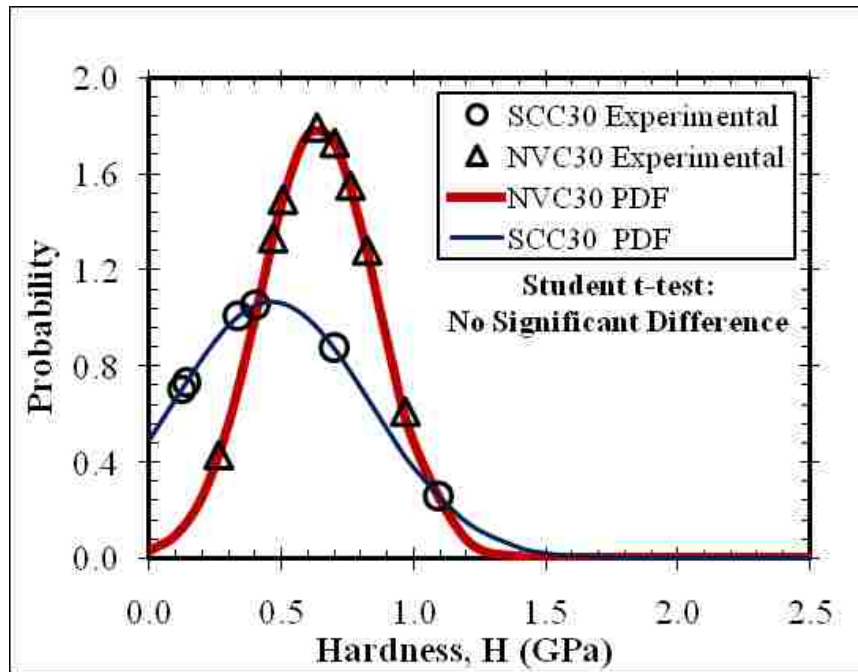


Figure 4.31. Comparison of hardness between SCC30 and NVC00 at 1.0 mN load

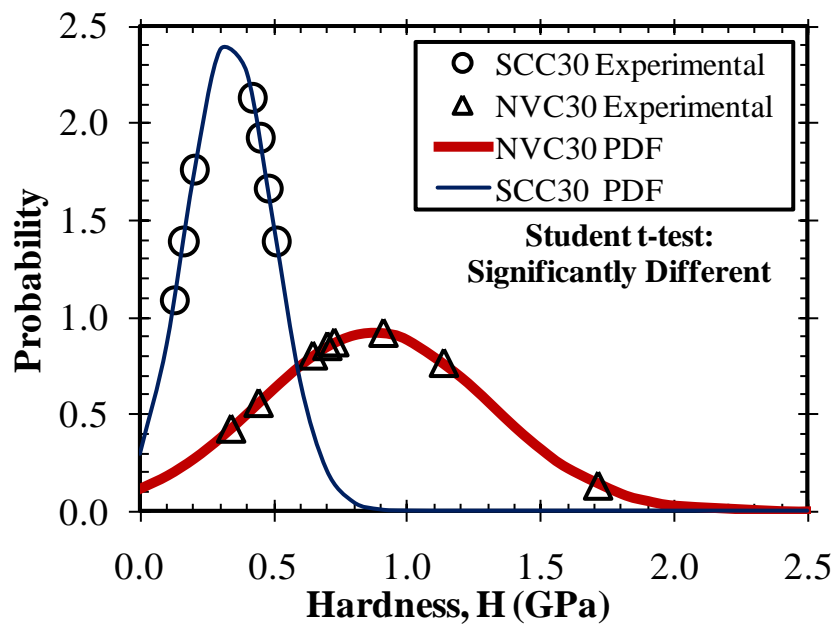
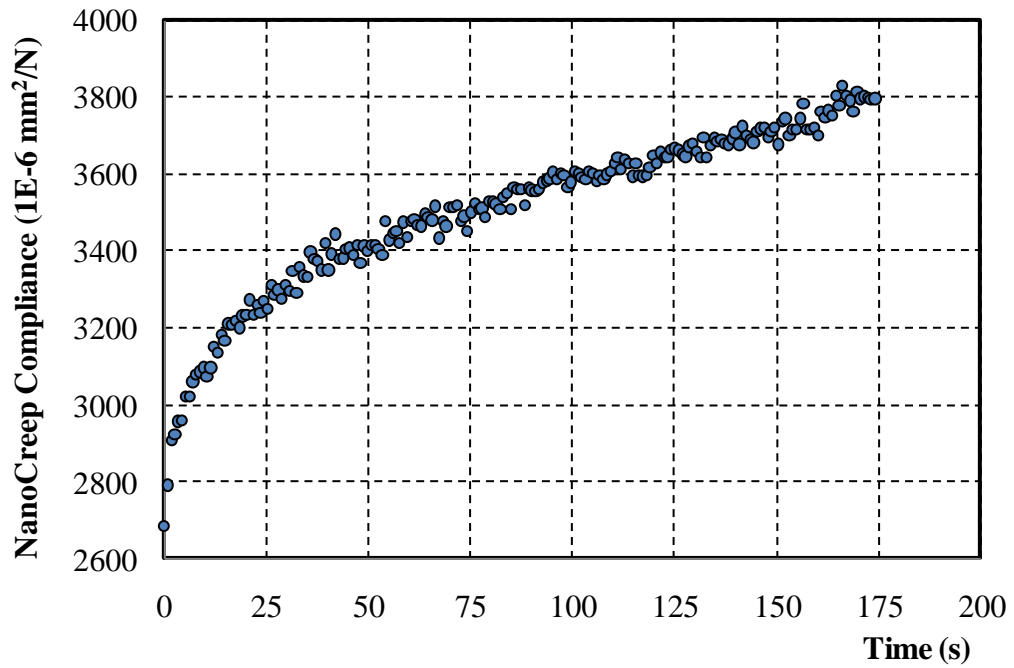
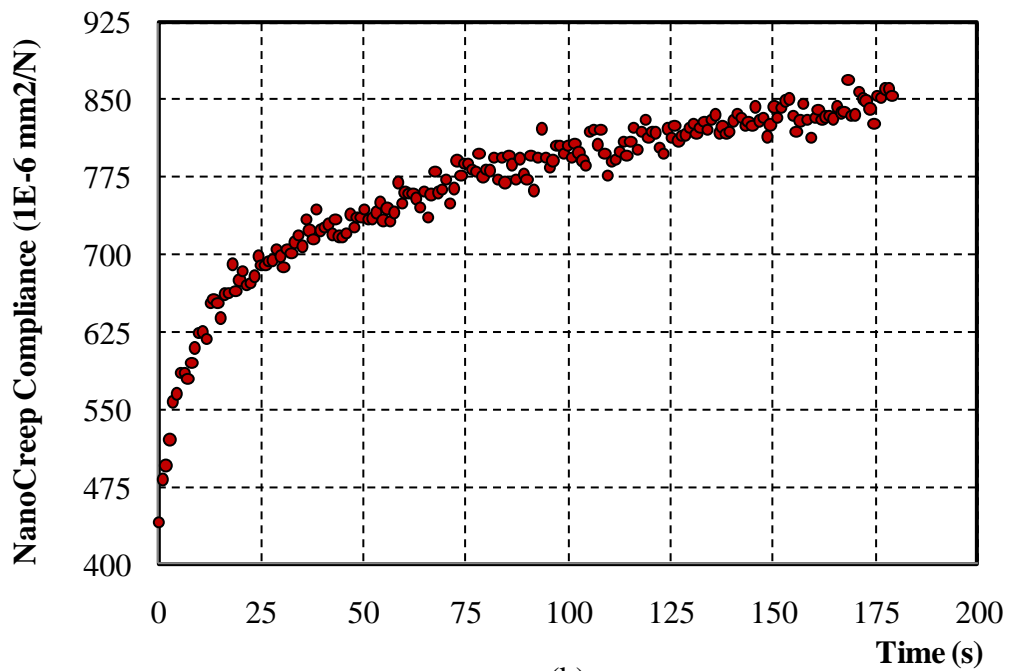


Figure 4.32. Comparison of hardness between SCC30 and NVC00 at 1.5 mN load

Figure 4.33 shows representative creep compliance curves for both SCC30 and NVC30. A significant difference in the ultimate creep compliance of the two cement pastes was observed at the 1 mN and the 1.5 mN loads. At the 0.5 mN load, the SCC paste exhibited slightly higher ultimate creep compliance, however no significant statistical difference was observed. The results of the nanoscale creep experiments match the results of the macroscale creep experiments where SCC30 exhibited higher creep compliance. Figure 4.34, Figure 4.35 and Figure 4.36 display comparisons of the ultimate creep compliance of SCC30 and NVC30 at loads of 0.5 mN, 1.0 mN, and 1.5 mN, respectively.



(a)



(b)

Figure 4.33. (a) SCC30 representative nanocreep compliance curve (b) NVC30 representative nanocreep compliance curve

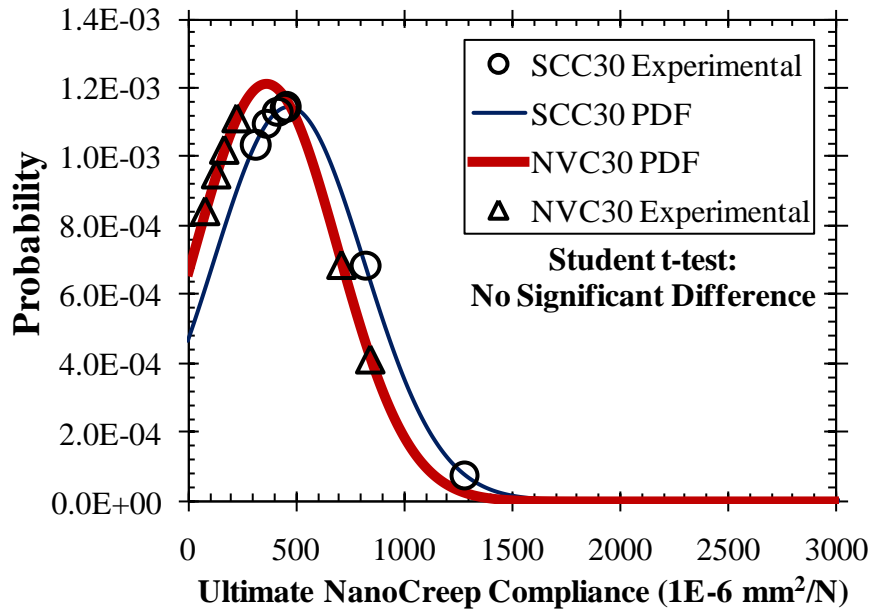


Figure 4.34. Comparison of ultimate creep compliance between SCC30 and NVC30 at 0.5 mN load

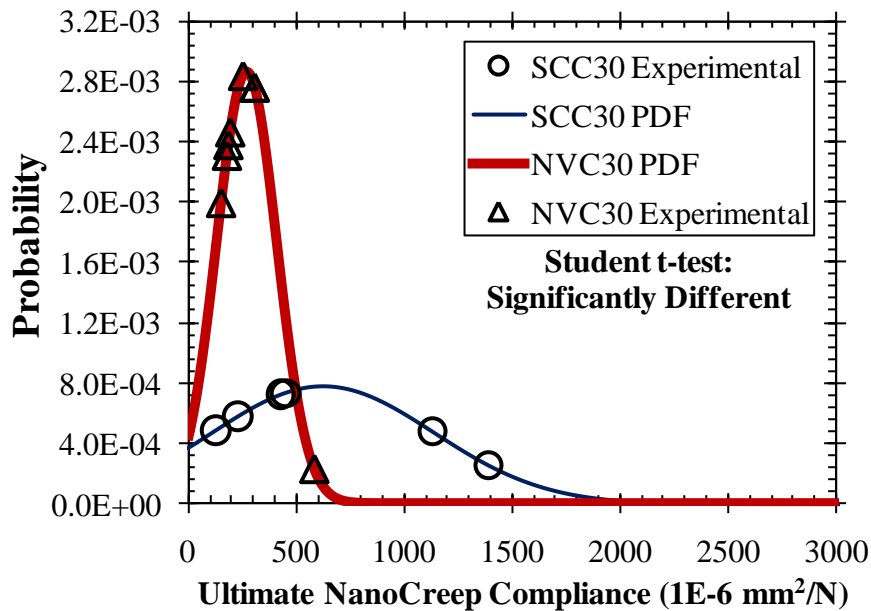


Figure 4.35. Comparison of ultimate creep compliance between SCC30 and NVC30 at 1 mN load

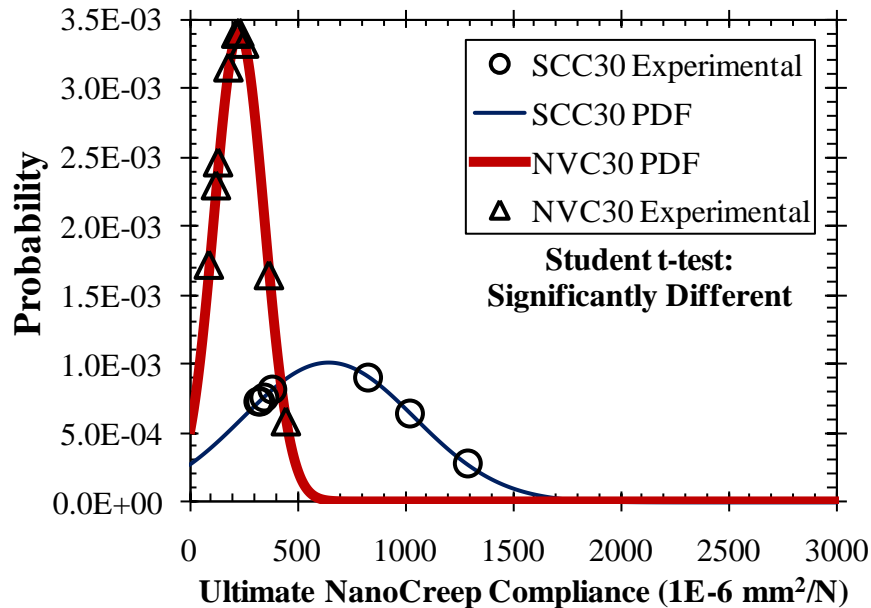


Figure 4.36. Comparison of ultimate creep compliance between SCC30 and NVC30 at 1.5 mN load

Again the small number of data points might not provide enough information to deduce definitive conclusions in comparing SCC30 to NVC30. However, the data clearly shows that SCC30 has a lower reduced modulus higher maximum depth of indentation and higher nano creep compliance than NVC30. Moreover, a lower hardness was observed for SCC30 at two out of three applied loads with only one showing no significant difference. One reason that SCC30 might exhibit lower nanomechanical properties than NVC30 with a similar compressive strength is that SCC contains a larger portion of fine materials. Specifically, the SCC30 mix in question has a much higher percentage of fly ash than the NVC. The higher amount of fly ash and superplasticizer coupled with the VMA allowed for the SCC mix to have a much lower water/binder ratio of 0.33 compared with the NVC mix's of 0.48. Consequently, with the higher amount of

fine particles and the lower amount of water available in the cement paste, the level of hydration of SCC paste would be less than that of NVC cement paste. While incorporating well graded fine particles in concrete (cement paste) mixes can help to provide a dense packing system of particles, the inability to hydrate all these particles due to the limited total water in the cement mix may lead to a well packed but soft microstructure.

These results also shed light on the significance of indentation depth on the properties extracted of multi-phase composite materials such as concrete or cement paste. The use of multiple loads enables extracting depth-independent properties which might be of a great value for composites like concrete. It was also shown that the reduced modulus is clearly a function of depth and a zero depth reduced modulus can be used to get a virtual modulus of the material before penetration of the indenter.

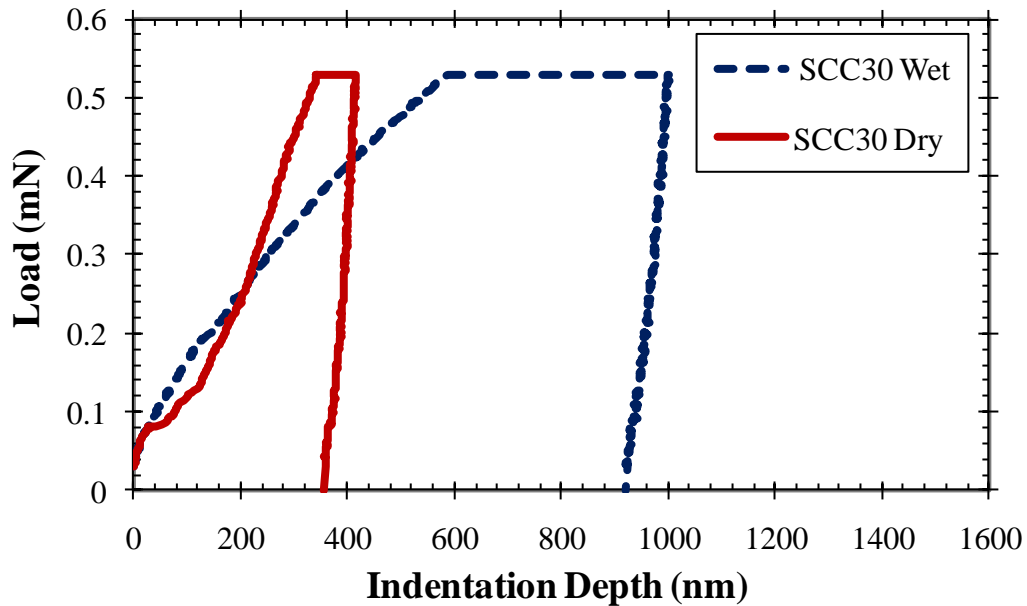
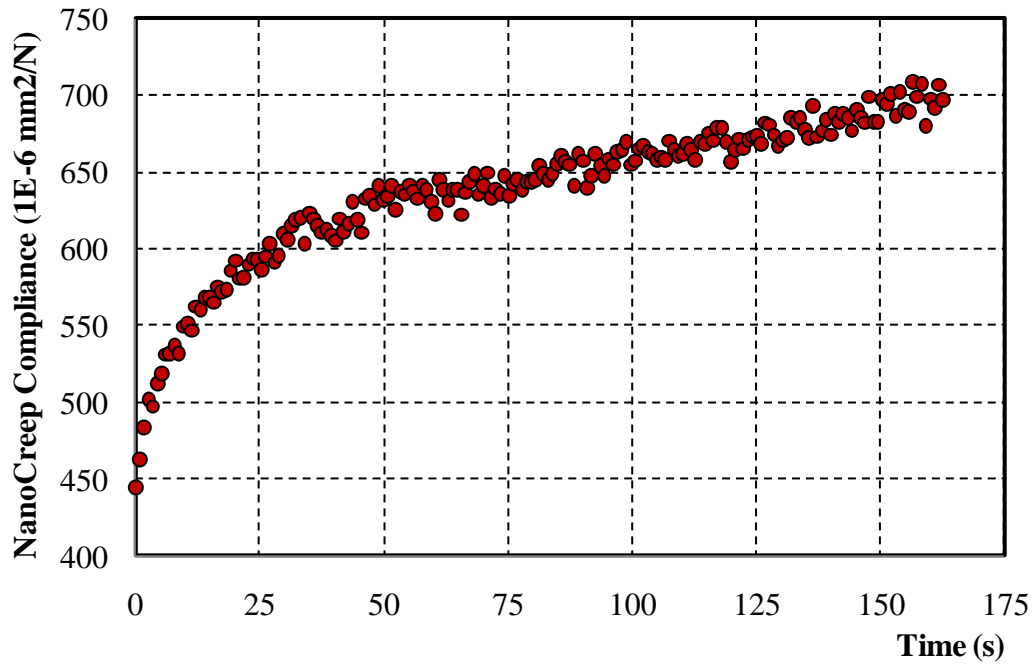


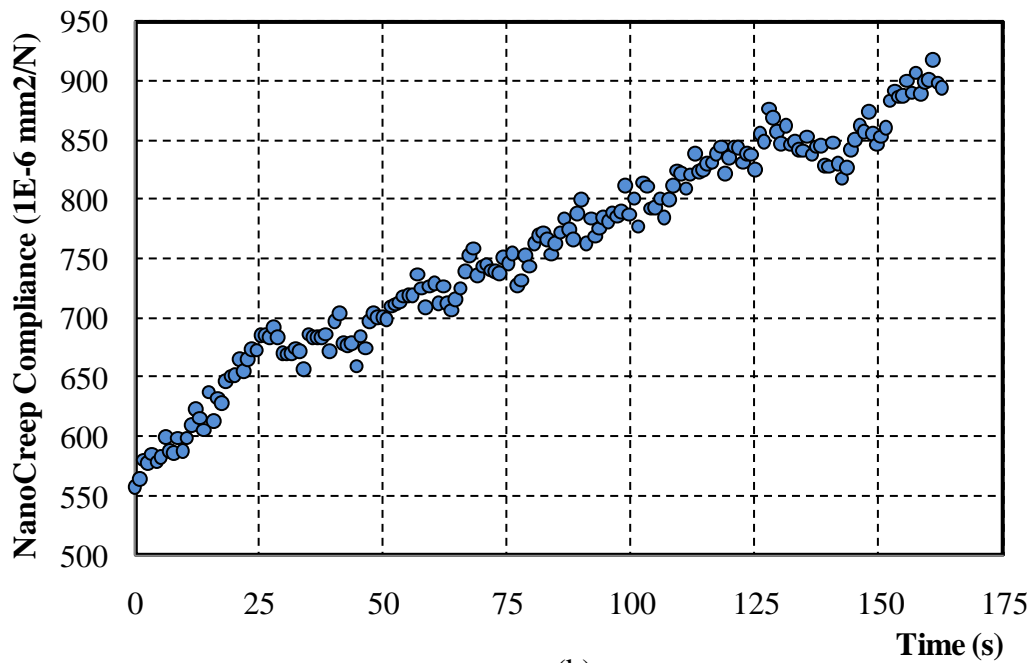
Figure 4.37. Representative load indentation curves for SCC30 cement paste under wet and dry conditions at a load of 0.5 mN

Attaching the wet stage attachment to the nanoindenter allowed for comparing the indentations made on the SCC cement paste under wet and dry conditions. From these experiments it was found that in general the specimens indented under dry conditions showed no significant difference in mechanical properties compared with the samples indented under wet conditions. For SCC30, the zero depth reduced modulus was 17.4 GPa under wet conditions and 20.2 GPa under dry conditions. Furthermore, only indentations made at the 1 mN load showed a significant difference of means based on the student t-test. However, there appeared to be some difference in the amount of creep compliance displayed by wet and dry specimens. For wet indentations, the mean ultimate creep compliance for the 0.5 mN, 1mN, and 1.5 mN loads was 1862 1E-6 mm²/N, 1129 1E-6 mm²/N, and 890 1E-6 mm²/N respectively. Whereas, for dry indentations the mean

ultimate creep compliance for the 0.5 mN, 1mN, and 1.5 mN loads was 584 1E-6 mm²/N, 627 1E-6 mm²/N, and 654 1E-6 mm²/N respectively. While a significant difference of means was not found the wet indentations clearly displayed higher creep compliance in comparison with the dry indentations. Figure 4.38 displays representative creep curves for indentations made on SCC30 under wet and dry conditions.



(a)



(b)

Figure 4.38. (a) SCC30 dry representative nano creep compliance curve (b) NVC30 wet representative nano creep compliance curve

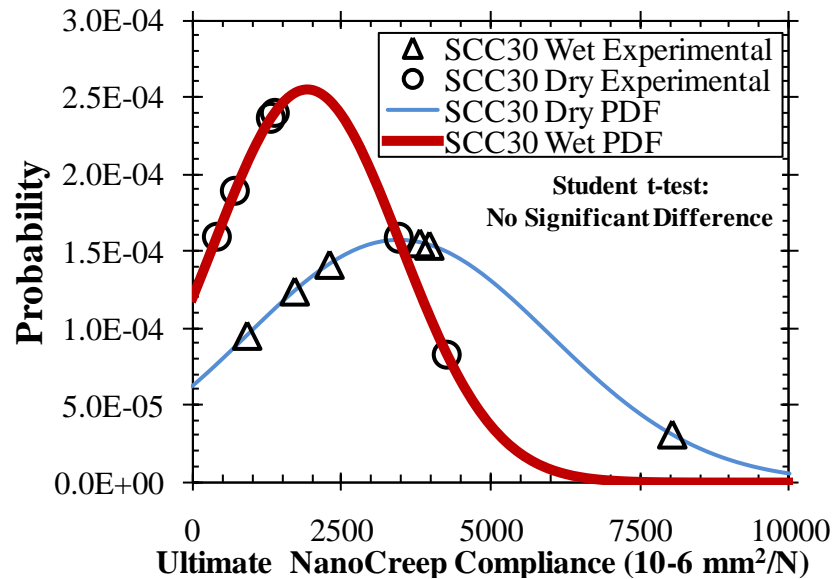


Figure 4.39. Comparison of ultimate creep compliance between SCC30 wet and dry indentations at 1mN load

It is interesting to observe higher creep compliance extracted from wet nanoindentations compared with dry nanoindentations. The effect of moisture on creep compliance at the nanoscale seems the opposite of moisture effect on creep compliance from macro creep experiments. At the macroscale, it is known that drying results in drying creep and thus higher ultimate creep compliance in comparison with specimens kept under moist conditions. This difference might be attributed to the significance of drying on the nanoindentation specimens. Drying of cementitious specimens will result in producing considerable shrinkage stresses at the specimen surface. Therefore, higher nanoindentation loads will be needed to produce a specific nanoindentation depth due to the need to overcome “shrinkage-induced” tensile stresses. This will be extended to creep as the net stress affecting the wet specimens is higher in the case of the wet indentation in comparison with that of dry indentation. Therefore, it is obvious that this possible surface

tensioning effect that occurs as a result of drying and shrinkage counteracted the load applied by the indenter. While such behavior might not be observed in other materials sensitive to drying (e.g. polymers), it seems to have a significant effect on cementitious materials due to the significant amount and influence of shrinkage observed by hydrated cement.

4.5.3 NANOINDENTATION EXPERIMENTAL PROGRAM N3

To obtain the nanomechanical properties of different phases of SCC, a line of 20 indents spaced 20 μm apart with a Berkovich indenter was performed on a 150 day old SCC40 concrete sample. Figure 4.40 shows a micrograph of the indented area of the SCC40 concrete sample. The line of 20 indents began at point A 4 μm above the gridline shown in red, ending at point B. The grid shown is 50 μm x 50 μm for each unit. So the whole area pictured is 500 μm x 500 μm .

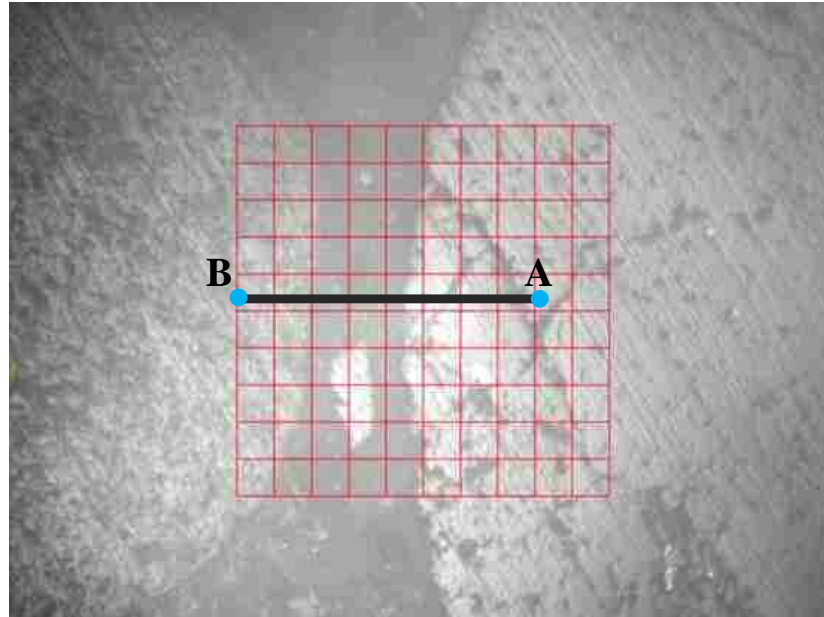


Figure 4.40. Micrograph of SCC40 concrete sample showing the line of indentation

Performing this experiment allowed for obtaining a spatial distribution of the nanomechanical properties along the line of indentation. Moreover, this allowed for determining hardness and stiffness values for the different phases encountered along the line of indentation, allowing for making distinctions between the nanomechanical properties of the mortar phase, aggregate phase, and ITZ. Figure 4.41 and Figure 4.42 show the spatial distribution along the line of indentation for mechanical properties of hardness and reduced modulus respectively.

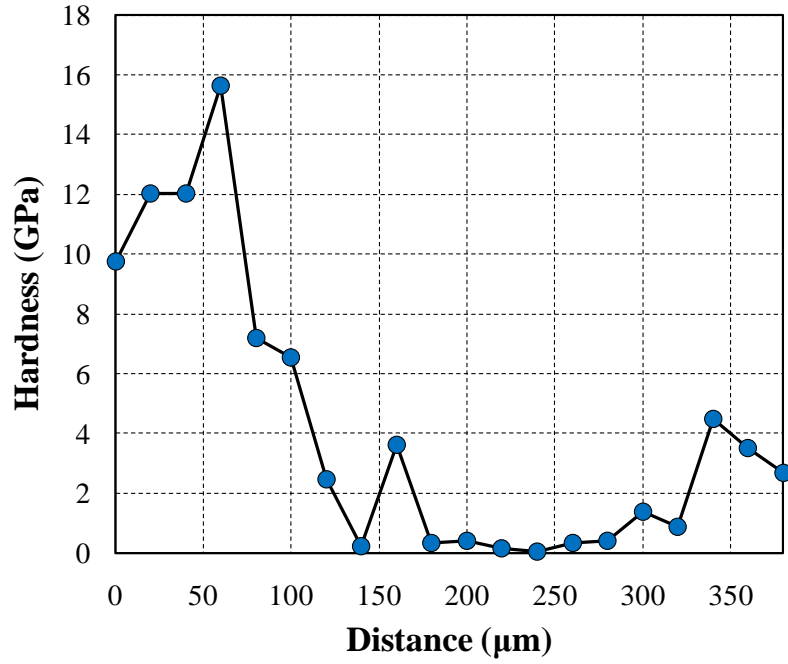


Figure 4.41. Spatial distribution of hardness on SCC40 concrete mix

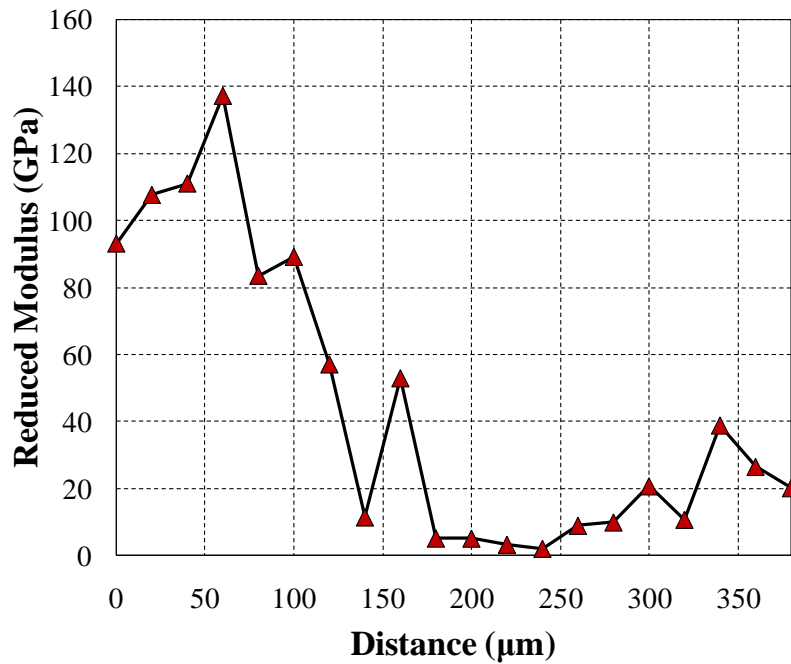


Figure 4.42. Spatial distribution of reduced modulus on SCC40 concrete mix

Figure 4.41 shows that indentations made on the aggregate displayed a high hardness, while indentations made at the mortar phase and ITZ displayed lower hardness. Moreover, this same trend was observed in Figure 4.42, as the indentations move into the area of ITZ and mortar phase the reduced modulus decreased.

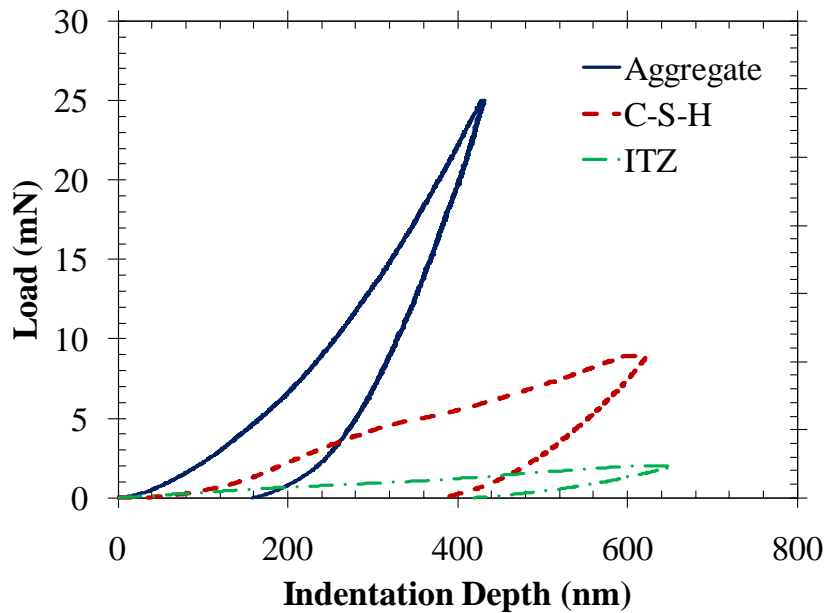


Figure 4.43. Load-indentation curves of aggregate, C-S-H, and ITZ for SCC40

Table 4.3. Nanomechanical properties for indented phases

	Maximum Depth (nm)	Hardness (GPa)	Reduced Modulus (GPa)	Total Work (nJ)
<i>Aggregate</i>	432	9.75	93.2	4.01
<i>C-S-H</i>	626	1.36	20.7	2.62
<i>ITZ</i>	651	0.33	5.2	0.25

Figure 4.43 shows load-indentation curves for the three indented phases of aggregate, C-S-H and ITZ. The aggregate indent was made at A, the C-S-H indent occurred at 320 μm from point A, and the ITZ indentation occurred at 200 μm from point A at the cement aggregate interface. Table 4.3 shows nanomechanical properties for the three indented phases. The aggregate showed the lowest maximum depth at 432 nm at a maximum load of 25 mN. The C-S-H showed a maximum depth of 626 nm at a load of 9 mN. The indentation made in the ITZ showed the highest maximum depth (651 nm) at the lowest applied load (2.4 mN). Moreover, the aggregate had the highest reduced modulus of 93.2 GPa and the ITZ indentation showed the lowest at 5.2 GPa. The ITZ indentation also displayed the lowest amount of energy absorbed during the indentation cycle at about 10 ten times less of the total energy absorbed by the C-S-H phase and 16 times less than the energy absorbed by the aggregate.

4.5.4 NANOINDENTATION EXPERIMENTAL PROGRAM N4

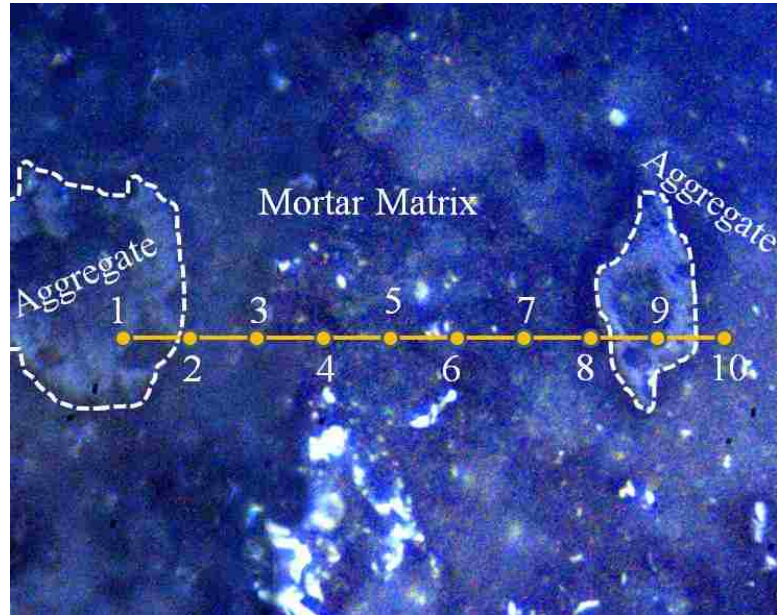


Figure 4.44. Micrograph showing indented area of UHPC165

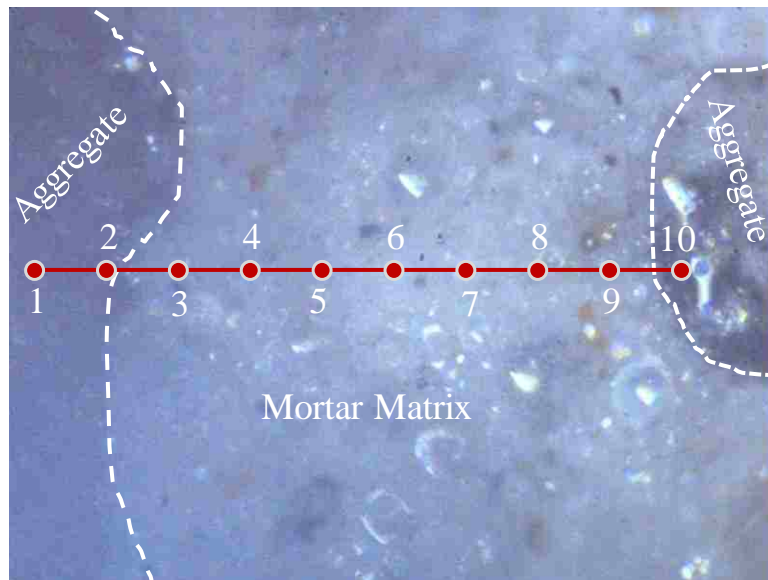


Figure 4.45. Micrograph showing indented are of SCC17

Figure 4.44 and Figure 4.45 show micrographs for one of the indented areas on each of the UHPC165 and SCC17 concrete mixes. The two concretes were indented at 14 days of age in two different lines of 10 points with a 50 μm spherical indenter spanning aggregate particles at a spacing of 30 μm . Figure 4.46 shows representative load-indentation curves of UHPC165 and SCC17.

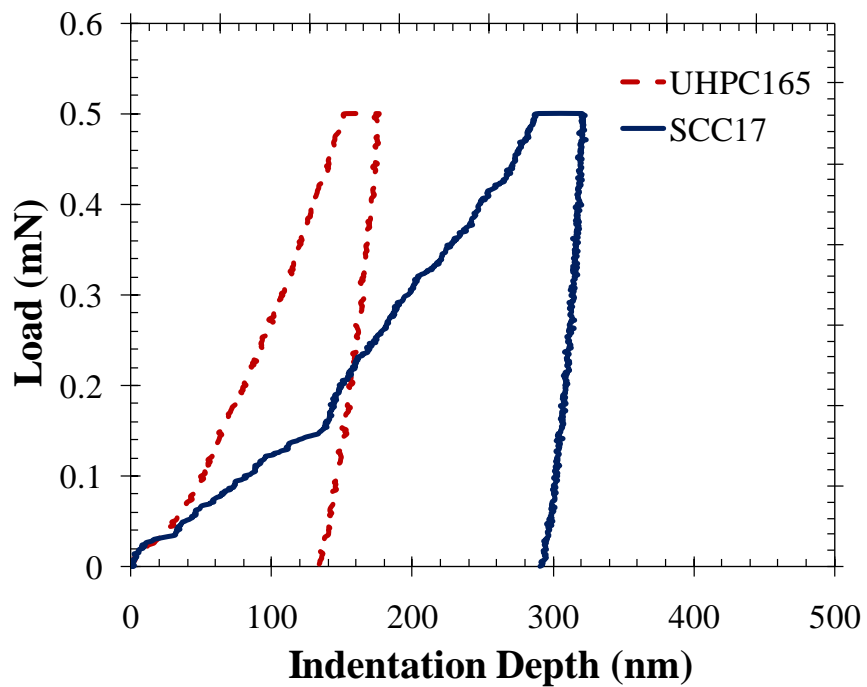


Figure 4.46. Representative load-indentation curves of UHPC165 and SCC17

Table 4.4. Nanomechanical properties of SCC17 and UHPC165

	SCC17		UHPC165	
	<i>Mean</i>	<i>Std.</i>	<i>Mean</i>	<i>Std.</i>
<i>Maximum Depth (nm)</i>	832	672	378	174
<i>Reduced Modulus (GPa)</i>	1.98	1.35	2.7	1.18
<i>Ultimate Creep Compliance (1E-6 mm²/N)</i>	31.6	34.4	8.5	5.7

Figure 4.47 shows the reduced elastic modulus distribution of both concrete mixes as observed along one line of nanoindentations performed in this experiment. The variation of the reduced elastic modulus presented in Figure 4.47 shows a significant drop of the reduced elastic modulus as indentations get in the vicinity of the ITZ. A significant increase in the modulus of elasticity of the aggregate phase in both concrete mixes compared to the cement phase can also be observed. It is important to note the absence of a significant difference of the reduced elastic modulus of the two concrete mixes despite their apparent differences in compressive strength (165 MPa versus 17 MPa). The variation along the indentation lines reveals two materials that are similar from an elastic response point of view as observed at the nanoscale. Figure 4.48 shows a comparison of all indents made on SCC17 and UHPC165 along with the results of a student t-test of means comparing these two concrete mixes. The results of the student t-test are consistent with the results along each line of indentation. One possible reason for lack of significant difference is that the reduced elastic modulus is extracted under unloading conditions which reduces the compressive stresses produced in the specimen due to indentation. Therefore, comparison of reduced elastic modulus extracted from nanoindentation to

tension elastic modulus might be more accurate than a comparison with compression elastic modulus. The relatively low tensile strength of the cement paste in all types of concrete might explain the limited difference in nanoscale properties compared with macroscale properties of the two types of concrete.

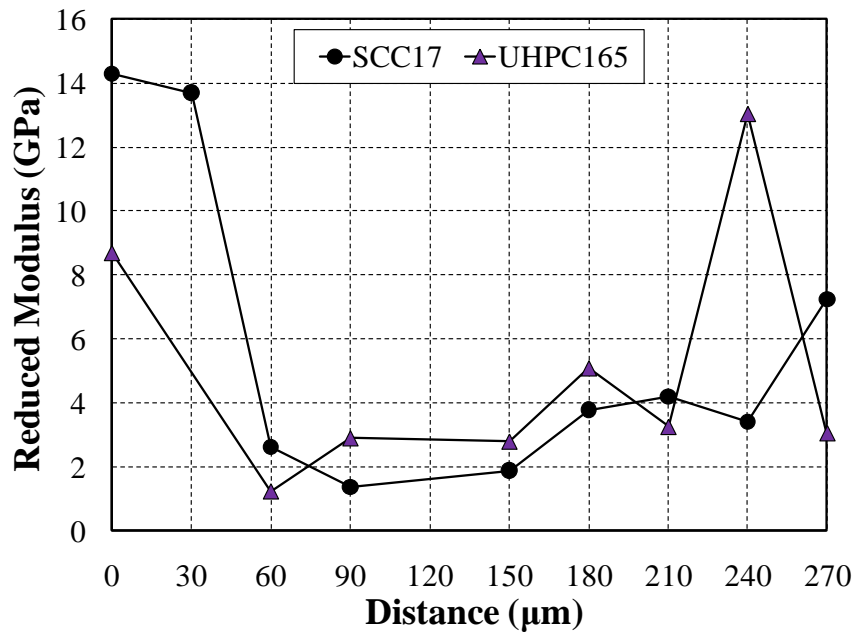


Figure 4.47. Spatial distribution of reduced modulus of SCC17 and UHPC165

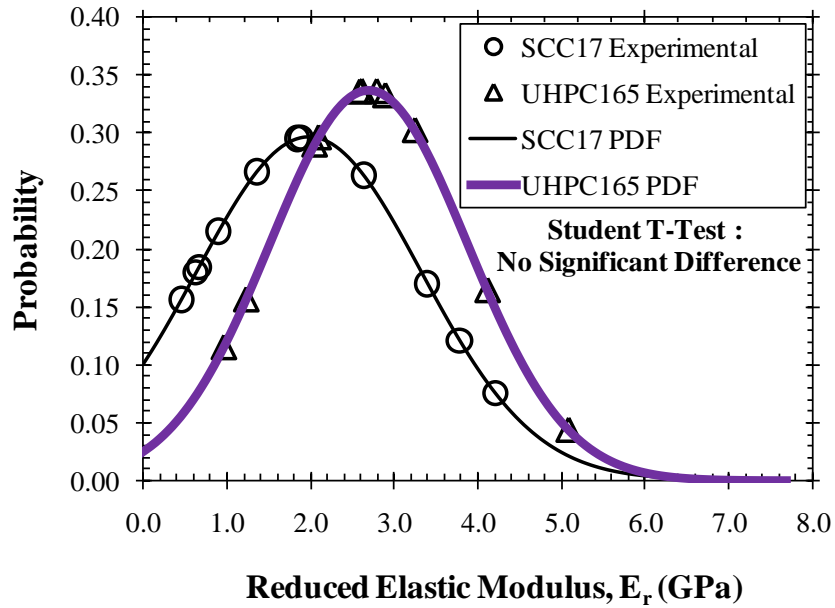


Figure 4.48. Comparison of reduced modulus between SCC17 and UHPC164

The results of the student t-test showed the SCC17 to exhibit a significantly higher maximum indentation depth as well as significantly higher ultimate creep compliance. Figure 4.49 and Figure 4.50 show a comparison of maximum indentation depth and ultimate creep compliance observed for all points made on both specimens along with the results of a student t-test of means for SCC17 and UHPC165, respectively.

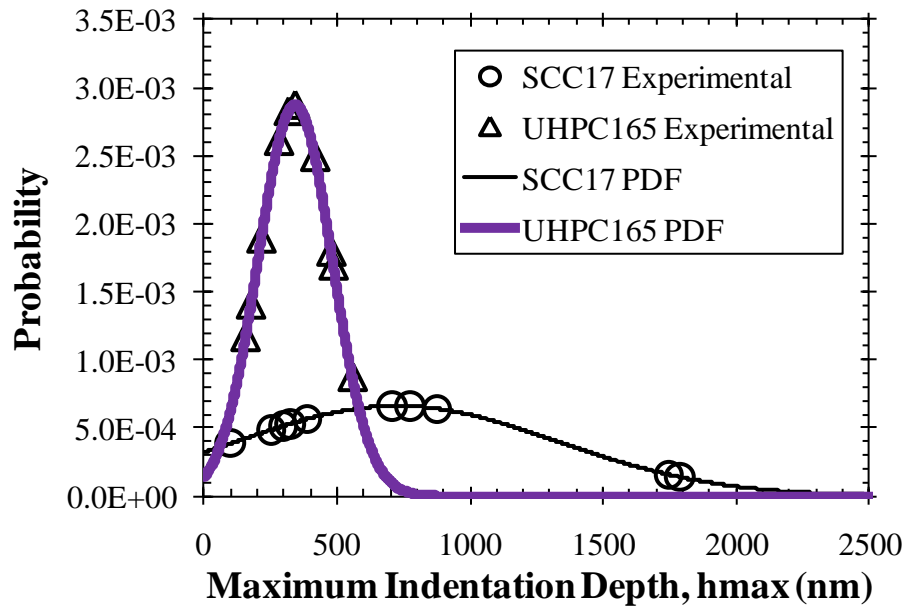


Figure 4.49. Comparison of maximum indentation depth between SCC17 and UHPC165

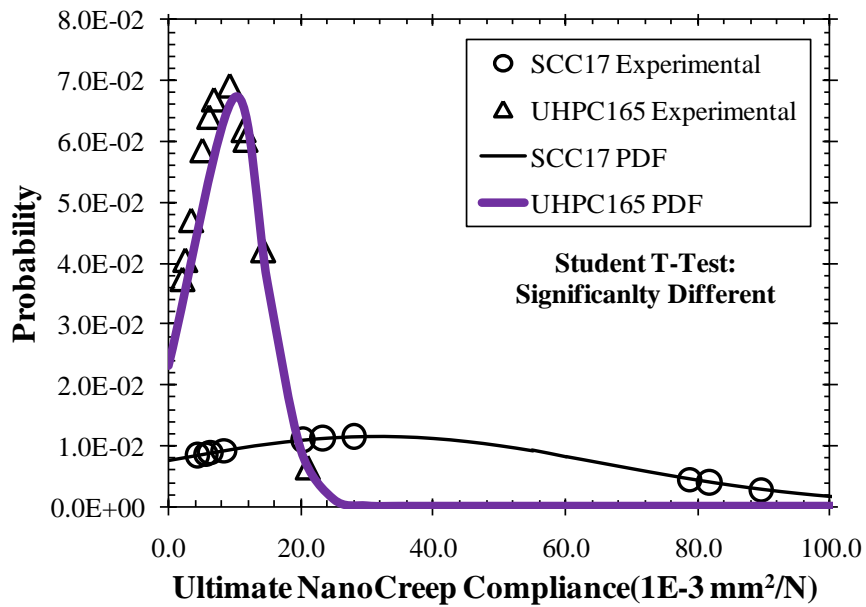
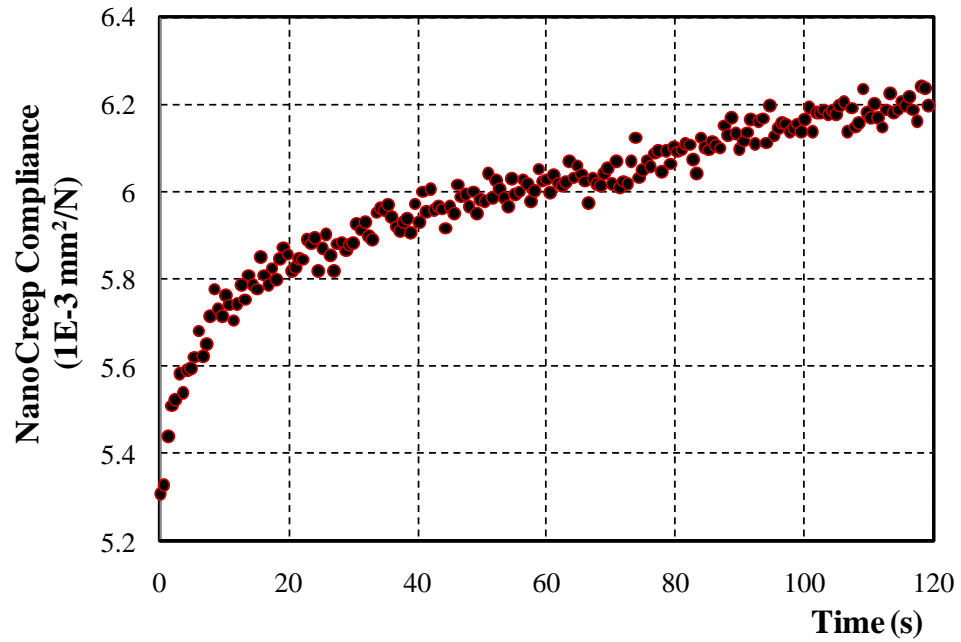
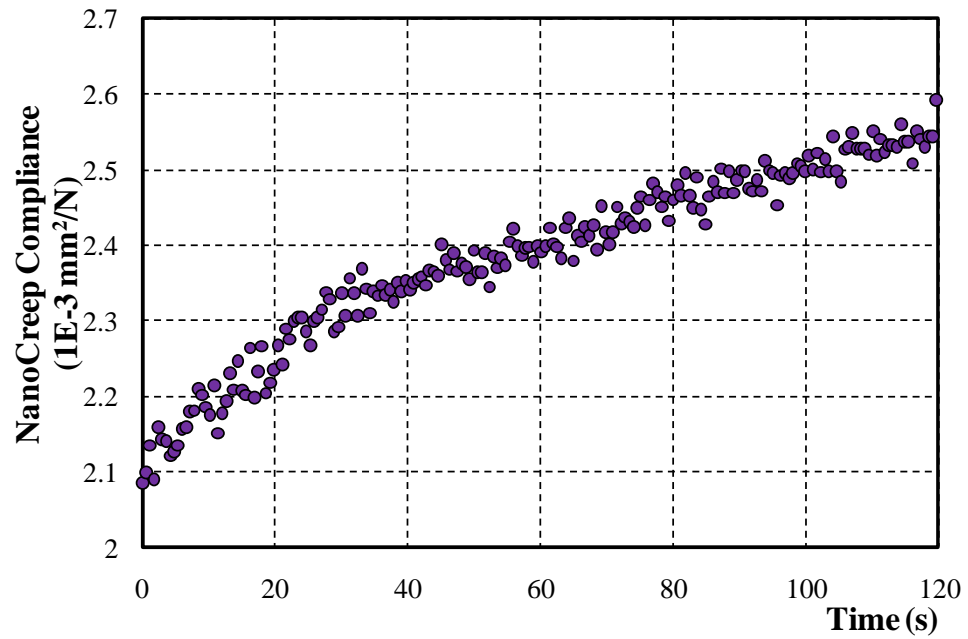


Figure 4.50. Comparison of maximum indentation depth between SCC17 and UHPC165

To compare creep compliance of the cement paste phase along the previously mentioned line of the two mixes, nanoindentation data at points 1, 2 and 10 in the SCC17 mix were excluded as nanoindentations at these points were performed at the aggregate phase. Nanoindentation data at points 1, 2 and 9 of the UHPC165 specimens were also excluded for being at the aggregate phase of the SCC17. The exclusion of the aggregate phase in this comparison is intended to avoid the influence of the significant difference between the two aggregates used in producing the UHPC165 and SCC17 mixes. While calcined bauxite (strong) aggregate was used to produce UHPC165, typical siliceous aggregate was used to produce the SCC17 mix. The ultimate creep compliance at any indentation point in both mixes is the highest creep compliance observed during the 120 second dwell period. Histograms of the ultimate creep compliance of the indentation lines in question for both mixes are shown in Figure 4.52. It was observed that SCC17 had a higher mean value of ultimate creep compliance with a mean value of 23.6 (1E-3) mm²/N compared to UHPC165 which had a mean value of only 8.3 (1E-3) mm²/N. Figure 4.51 shows representative creep compliance curves for both SCC17 and UHPC165.

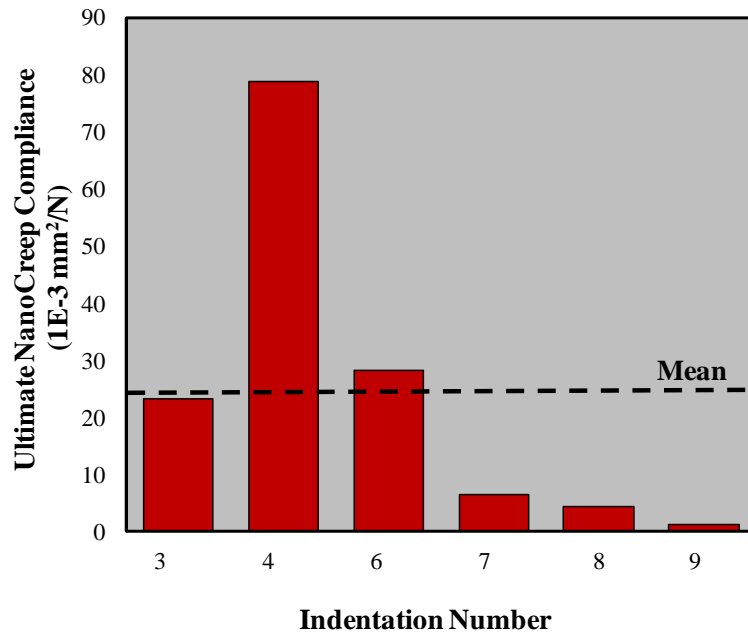


(a)

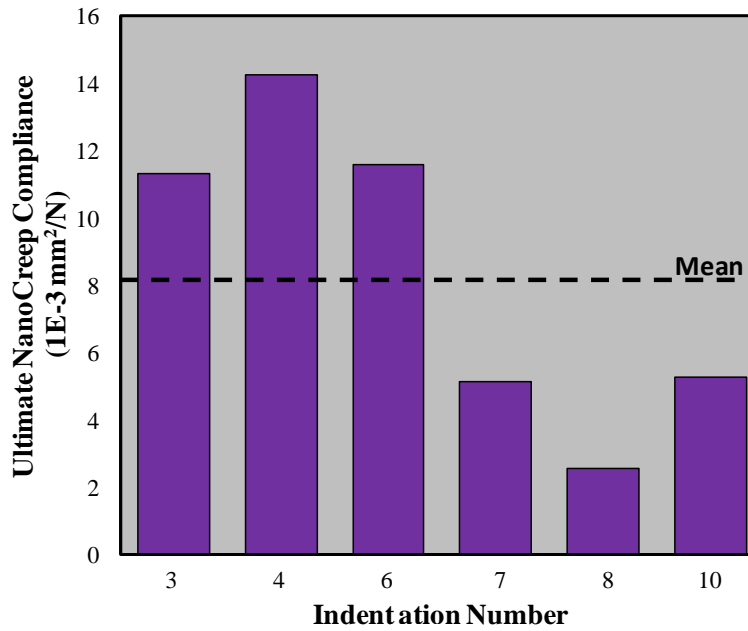


(b)

Figure 4.51. (a) SCC17 dry representative nanocreep compliance curve (b) UHPC165 wet representative nanocreep compliance curve



(a)



(b)

Figure 4.52. (a) Histogram of ultimate creep compliance observe along given line on SCC17 (b) Histogram of ultimate creep compliance observe along given line on UHPC165

The relatively high creep compliance of the SCC17 mix might be attributed to the vast difference in the microstructure between the two concrete mixes. Table 4.5 shows the results from a microstructural model of the cement paste constructed using Hymostruc™.

Table 4.5. Results from Hymostruc™ model

	SCC17 (%)	UHPC167 (%)
<i>C-S-H</i>	28	34
<i>CH</i>	5	0
<i>Unhydrated Cement</i>	7	37
<i>Capillary Pores</i>	24	0
<i>Unreacted Pozzolans</i>	33	25
<i>Others</i>	4	3

It can be observed from the table that the SCC17 mix contained a high estimated percentage of calcium hydroxide (CH) and capillary pores. On the other hand, the UHPC165 mix had 0% estimated percentage of capillary pores and CH. Moreover, these results show a similar response to what the authors would expect to see on the macroscale. It is interesting to observe that such observation prevails in the cement paste phase when measured at the nanoscale. This tells us that the materials used to produce SCC17 significantly altered the microstructure making the concrete more prone to creep. These materials affect the porosity and might even affect pore size distribution. This could explain the differences in creep of the two concretes even though no significant difference was found between other nanomechanical properties (i.e. reduced modulus).

The ability of nanoindentation to allow separating creep of cement paste and aggregate phases can open new venues for modeling creep. While most current creep models of concrete are phenomenological models, multiscale observations of creep for different concrete phases will enable new fundamental modeling methods that can provide higher accuracy than phenomenological models.

CHAPTER 5. CONCLUSIONS

In this thesis, creep of self consolidating concrete (SCC) at the macro and nanoscale was investigated. The differences of creep behavior between SCC and normal vibrated concrete (NVC) mixes were examined and reported. Furthermore, it was shown that nanoindentation could be used to characterized creep properties of different concrete and cement paste phases at the nanoscale.

5.1 MACROSCALE CREEP OF SCC

SCC mixes were produced with the aid of a viscosity modifying agent (VMA) and fly ash as replacement for cement. All examined SCC mixes achieved the required flowability, viscosity and passability with no visual signs of bleeding or segregation during testing of SCC mixes in the fresh state. Furthermore, it appeared that there was a limit of fly ash content beyond which the increase in water demand due to the fineness of fly ash outweighed the enhancement in flowability, thus making the production of a concrete that meets SCC flowability and passability limits impossible.

5.1.1 CREEP UNDER COMPRESSIVE STRESSES

SCC showed a different shrinkage performance compared with NVC depending on the amount of fly ash replacement. Increasing the fly ash replacement ratio resulted in a higher total shrinkage strain of SCC. For basic shrinkage the mix with the highest amount of fly ash replacement showed the highest basic shrinkage strain. The basic shrinkage strain decreased as the fly ash replacement ratio decreased.

For mixes with the same water/binder ratio, all SCC mixes experienced higher creep compliance in comparison with the NVC mix probably due to the inclusion of fly ash and the relatively higher sand-to-total aggregate ratio. The effect of fly ash content on total creep compliance was similar to its effect on total shrinkage strain of SCC. In fact, increasing the fly ash (replacement ratio) in SCC led to higher total creep compliance. The comparison of SCC and NVC mixes of similar compressive strength at time of loading also showed SCC mixes to have higher creep compliance. This again can be attributed to the higher fly ash contents and higher sand-to-total aggregate ratio in the SCC mixes.

The influence of fly ash replacement ratio on basic creep compliance was similar to its effect on total creep compliance. Increasing the amount the fly ash replacement ratio led to higher basic creep compliance. All SCC mixes showed higher or similar basic creep compliance to the NVC mix with similar water/binder ratio. Moreover, SCC mixes exhibited higher basic creep compliance in comparison with NVC mixes with similar compressive strength at loading.

Comparison of the experimental results with the ACI 209 creep prediction model showed the ACI model to be unable to predict the creep of SCC. It was shown that using maximum slump for SCC mixes was not adequate for creep prediction. Therefore, a modified ACI model was suggested allowing for the model to more accurately predict the creep coefficient of SCC mixes containing fly ash.

The CEB-FIP MC90-99 creep prediction model also underestimated the amount of creep for all three SCC mixes. The underestimation was most pronounced for the SCC mix with an intermediate amount of fly ash. It is recommended that the MC90-99 model be modified to allow safe prediction of creep of SCC with high amounts of fly ash.

5.1.2 CREEP UNDER TENSILE STRESSES

SCC and NVC tension specimens showed no significant difference in total shrinkage strains. The SCC mix with the highest fly ash replacement ratio showed the lowest amount of shrinkage, however, this mix showed the highest weight loss percentage. Subsequently, this could have been attributed to experimental error and the difficulties associated with precisely acquiring such very small shrinkage displacements. There

seemed to be no clear trend regarding basic shrinkage with the NVC mix, with the highest water/binder ratio showing the highest basic shrinkage strain.

The SCC mix containing the lowest amount of fly ash replacement showed higher tension creep compliance in comparison with an NVC mix of similar strength. On the other hand, the SCC mix with the higher amount of fly ash showed drastically lower tension creep compliance than the NVC of similar strength. This might be attributed to the extremely high water/binder ratio used to produce a low strength NVC without significantly increasing the fly ash content. The basic creep compliance of the four mixes (2 SCC and 2 NVC) showed the same trends as the total creep compliance.

5.2 NANOSCALE CHARACTERIZATION OF SCC

The nanomechanical properties of SCC30 and NVC00 cement pastes were successfully extracted using nanoindentation. The SCC30 mix showed a significantly higher maximum indentation depth at both loads of 0.5 mN and 1 mN based on the student t-test of means. A significant difference in hardness was only observed for the indentations made at a load of 1 mN. Moreover, the NVC00 paste showed a significantly higher reduced modulus for both loads. Finally, a change in the distribution of high density (HD) and low density (LD) calcium silicate hydrate (C-S-H) was observed. It appears that the C-S-H developed in the cement paste including pozzolans might differ from the C-S-H developed through normal cement hydration (no pozzolans).

The cement paste of SCC30 and NVC30 mixes with similar compressive strength were compared. The two materials showed a significant difference in most nanoscale mechanical properties. SCC30 showed a softer behavior than NVC30 at the nanoscale with a significantly higher maximum indentation depth for all three applied loads (0.5 mN, 1 mN and 1.5 mN). The SCC30 mix also displayed less stiffness in comparison with NVC30 having a significantly different reduced modulus at all three load levels. Furthermore, SCC30 was found to have a lower zero depth reduced modulus of 20.2 GPa in comparison with NVC30's of 38.9 GPa. However, SCC30 only showed a significant difference in hardness at the 0.5 mN load.

Nano-creep compliance was higher under wet conditions than under dry conditions. This might be explained by the significance of shrinkage on generating tensile stresses at the nanoindentation specimen surface which results in consuming part of the indentation

stress to counteract these tensile stresses. It appears that the effect of drying on nanoscale creep compliance was the opposite to that of macrocreep compliance.

It was also shown here that nanomechanical properties of an SCC [22] specimen could be extracted by indenting on a line between two aggregate particles. Furthermore, we present experimental and numerical methods to mechanically characterize individual representative points in the aggregate, cement paste and interfacial transition zone (ITZ). The aggregate phase showed the highest nanomechanical properties taking the highest load with the lowest maximum depth. The cement paste (most likely C-S-H) showed superior mechanical properties at the nanoscale in comparison with the ITZ (very porous phase) showing higher reduced elastic modulus, higher hardness and higher energy absorption.

Finally, an ultra high performance concrete (UHPC) mix with a 28 compressive strength of 165 MPa was compared to a low strength SCC mix with a 28 compressive strength of 20 MPa. Reduced elastic modulus and nano creep compliance of both mixes were extracted at twenty indentation points and compared using a spherical nanoindenter. The distribution of the reduced elastic modulus between the two aggregate particles of both mixes showed similar trend of a reduced elasticity at the ITZ compared with that of the aggregate phase. No significant difference in the reduced elastic modulus of cement phase in both concrete was observed in spite of the significant difference in compressive strength between the two concretes. Moreover, UHPC showed significantly lower creep compliance compared to SCC. The proposed method for characterizing nano creep compliance of concrete enables a new trend of creep modeling of concrete.

5.3 FUTURE WORK

To further investigate the affect of fly ash on SCC mixes more research is needed on mixes with different amounts of fly ash replacement. Moreover, investigating the differences of the effects of different pozzolans on creep and shrinkage in comparison with SCC mixes produced is proposed. Furthermore, due to the apparent humidity loss of the sealed specimens, repeating the basic shrinkage and creep tests by keeping specimens in a 100% humidity controlled environment might give more accurate results. It might also prove valuable to investigate incorporating carbon and steel fibers to curb tensile creep of the SCC. Finally, a study of porosity and pore size distribution of SCC compared with NVC might provide an explanation for the apparent differences in creep behavior.

A full scale microstructural characterization with the use of a scanning electron microscope (SEM) would be helpful in further explaining some of the nanoindentation results. Furthermore, performing a very large number of indents using a spherical indenter on the cement pastes of all specimens used in the macrocreep experiments could shed some more light on correlations between nanoscale and macroscale creep. Nanoindentation of cement paste specimens incorporating large volumes of superplasticizers and viscosity modifying agents might shed light on the significance of the admixtures on creep of SCC.

REFERENCES

1. Persson, B., *Self Consolidating Concrete, High Performance Concrete, and Normal Concrete, Affected by Creep at Different Age, Curing, Load Level, Strength, and Water-Cement Ratio with some Interrelated Properties*. American Concrete Institute Special Publication, 2005. 229: p. 63 - 91.
2. Persson, B., *Shrinkage and Creep of High-Performance Self-Compacting Concrete (HPSCC)*. American Concrete Institute Special Publication, 2004. 220: p. 155-180.
3. Ogawa, A., Sakata, K., and Tanaka, S., *A Study on Reducing Shrinkage of Highly-Flowable Concrete Proceedings of the Second CANMET/ACL International Symposium on Advances in Concrete Technology*. American Concrete Institute Special Publication, 1995. 154: p. 55-72.
4. Di Fabio, F., Galeota, D., Giammatteo, M.M., and Gregori, A. *Long Term Behavior of SCC Precast Members in Third North American Conference on the Design and use of Self-Consolidating Concrete 2008*. Chicago, Illinois.
5. Reinhardt, A.K., Adam, I.A., and Taha, M.M.R. *Total and Basic Creep and Shrinkage of Self-Consolidating Concrete*. in *Third North American Conference on the Design and use of Self-Consolidating Concrete 2008*. Chicago, Illinois.
6. Yehia, S., Abudayyeh, O., Zalt, A., and Barbera, J. *Evaluation of Time Dependent Properties of a SCC Mix*. in *Third North American Conference on the Design and use of Self-Consolidating Concrete 2008*. Chicago, Illinois.
7. Bonen, D. and Shah, S.P., *Fresh and hardened properties of self-consolidating concrete*. *Progress in Structural Engineering and Materials*, 2005. 17(1): p. 14-26.
8. Mondal, P., Shah, S.P., and Marks, L., *A reliable technique to determine the local mechanical properties at the nanoscale for cementitious materials*. *Cement and Concrete Research*, 2007. 37(10): p. 1440-1444.
9. Constantinides, G., Ulm, F., and Van Vliet, K., *On the use of nanoindentation for cementitious materials*. *Materials and Structures*, 2003. 36(257): p. 191-196.
10. Constantinides, G. and Ulm, F.J., *The nanogranular nature of C-S-H*. *Journal of the Mechanics and Physics of Solids*, 2007. 55(1): p. 64-90.
11. Mondal, P., Shah, S.R., and Marks, L.D., *Nanoscale characterization of cementitious materials*. *ACI Materials Journal*, 2008. 105(2): p. 174-179.

12. Zhu, W., Hughes, J.J., Bicanic, N., and C.J., P., *Nanoindentation mapping of mechanical properties of cement paste and natural rocks*. *Materials Characterization*, 2007. 58(11-12): p. 1189-1198.
13. Reinhardt, A.K., Sheyka, M.P., Garner, A.P., Al-Haik, M., and Taha, M.R., *Experimental and Numerical Characterization of Two Phases in Concrete*. *International Journal of Mechanics and Materials in Design*, 2008. 4(4): p. 407–418.
14. Tweedie, C.A. and Van Vliet, K.J., *Contact creep compliance of viscoelastic materials via nanoindentation*. *Journal of Material Research*, 2006. 21(6): p. 1576-1589.
15. ACI Committee 209, *Guide for Modeling and Calculating Shrinkage and Creep in Hardened Concrete*. 2008, American Concrete Institute.
16. Ozawa, K., Neakawa, K., Kunishima, M., and Okamura, H. *Development of high-performance concrete based on durability design of concrete structures*. in *East Asia and Pacific Conference on Structural Engineering and Construction (EASEC-2)*. 1989.
17. Domone, P.L., *Self-compacting concrete: An analysis of 11 years of case studies* *Cement & Concrete Composites*, 2005. 28(2): p. 197-208.
18. Ambroise, J., Rols, S., and Pera, J., *Production and Testing of Self-leveling Concrete*. American Concrete Institute Special Publication, 1999. 186: p. 555-556.
19. Nehdi, M., El Chabib, H., and El Naggar, H., *Cost-Effective SCC for Deep Foundations*. *Concrete International*, 2003. 25(3).
20. Ho, D.W.S., Shenin, A.M.M., and Tam, C.T., *The sandwich concept of construction with SCC*. *Cement and Concrete Research*, 2001. 31(9): p. 1377 - 1381.
21. Okamura, H. and Ouchi, M., *Self-compacting high performance concrete*. *Progress in Structural Engineering and Materials*, 1998. 1(4): p. 378-383.
22. The European Self-Compacting Concrete Group, *The European Guide lines for Self-Compacting Concrete*, BIBM, CEMBUREAU, ERMCO, EFCA, and EFNARC, 2005.
23. Bonen, D. and Shah, S.P., *The effects of formulation on the properties of self-consolidating concrete*, in *Concrete Science and Engineering A Tribute to Arnon Bentur International RILEM Symposium* K. Kolver, S. Marchand, S. Mindess, and J. Weiss, Editors. 2004, RILEM. p. 43-56.

24. Khayat, K.H., *Viscosity-enhancing admixtures for cement-based materials - An overview*. Cement & Concrete Composites, 1998. 20(2-3): p. 171-188.
25. ASTM, *ASTM C143 / C143M - 09 Standard Test Method for Slump of Hydraulic-Cement Concrete*. 2009, ASTM International: West Conshohocken, PA.
26. ASTM, *ASTM C1611 / C1611M - 09b Standard Test Method for Slump Flow of Self-Consolidating Concrete*. 2009, ASTM International West Conshohocken, PA.
27. Khayat, K.H. and Mitchell, D., *Self Consolidating Concrete for Precast, Prestressed Concrete Bridge Elements*, Federal Highway Administration (FHWA) 2009, Transportation Research Board, Washington, D.C.
28. Boukendakdji, O., Kenai, S., Kadri, E.H., and Rouis, F., *Effect of slag on the rheology of fresh self-compacted concrete*. Construction and Building Materials, 2009. 23(7): p. 2593-2598.
29. El-Chabib, H. and Nehdi, M., *Effect of mixture design parameters on segregation of self-consolidating concrete*. ACI Materials Journal, 2006. 103(5): p. 374-383.
30. Ghezal, A. and Khayat, K.H., *Optimizing self-consolidating concrete with limestone filler by using statistical factorial design methods*. Aci Materials Journal, 2002. 99(3): p. 264-272.
31. Guneyisi, E. and Gesoglu, M., *Properties of self-compacting mortars with binary and ternary cementitious blends of fly ash and metakaolin*. Materials and Structures, 2008. 41(9): p. 1519-1531.
32. Guneyisi, E., Gesoglu, M., and Ozbay, E., *Effects of marble powder and slag on the properties of self compacting mortars*. Materials and Structures, 2009. 42(6): p. 813-826.
33. Hwang, S.D., Khayat, K.H., and Bonneau, O., *Performance-based specifications of self-consolidating concrete used in structural applications*. ACI Materials Journal, 2006. 103(2): p. 121-129.
34. Khayat, K.H., Ghezal, A., and Hadriche, M.S., *Factorial design models for proportioning self-consolidating concrete*. Materials and Structures, 1999. 32(223): p. 679-686.
35. Sahmaran, M., Yaman, I.O., and Tokyay, M., *Transport and mechanical properties of self consolidating concrete with high volume fly ash*. Cement & Concrete Composites, 2009. 31(2): p. 99-106.

36. Sonebi, M., *Applications of statistical models in proportioning medium-strength self-consolidating concrete*. ACI Materials Journal, 2004. 101(5): p. 339-346.
37. Wu, Z.M., Zhang, Y.G., Zheng, J.J., and Ding, Y.N., *An experimental study on the workability of self-compacting lightweight concrete*. Construction and Building Materials, 2009. 23(5): p. 2087-2092.
38. Ng, I.Y.T., Wong, H.H.C., and Kwan, A.K.H., *Passing ability and segregation stability of self-consolidating concrete with different aggregate proportions*. Magazine of Concrete Research, 2006. 58(7): p. 447-457.
39. Khayat, K.H., Assaad, J., and Daczko, J., *Comparison of field-oriented test methods to assess dynamic stability of self-consolidating concrete*. ACI Materials Journal, 2004. 101(2): p. 168-176.
40. Kwan, A.K.H. and Ng, I.Y.T., *Optimum superplasticiser dosage and aggregate proportions for SCC*. Magazine of Concrete Research, 2009. 61(4): p. 281-292.
41. Nehdi, M. and Ladanchuk, J.D., *Fiber synergy in fiber-reinforced self-consolidating concrete*. ACI Materials Journal, 2004. 101(6): p. 508-517.
42. Sahmaran, M., Yaman, O., and Tokyay, M., *Development of high-volume low-lime and high-lime fly-ash-incorporated self-consolidating concrete*. Magazine of Concrete Research, 2007. 59(2): p. 97-106.
43. Sonebi, M., *Medium strength self-compacting concrete containing fly ash: Modelling using factorial experimental plans*. Cement and Concrete Research, 2004. 34(7): p. 1199-1208.
44. Sonebi, M., Grunewald, S., and Walraven, J., *Filling ability and passing ability of self-consolidating concrete*. ACI Materials Journal, 2007. 104(2): p. 162-170.
45. Domone, P.L., *A review of the hardened mechanical properties of self-compacting concrete*. Cement & Concrete Composites, 2007. 29(1): p. 1-12.
46. Leemann, A., Munch, B., Gasser, P., and Holzer, L., *Influence of compaction on the interfacial transition zone and the permeability of concret*. Concrete and Cement Research, 2006.
47. Zhu, W. and Bartos, P.J.M., *Permeation properties of self-compacting concrete*. Cement and Concrete Research, 2003. 33(6): p. 921-926.
48. Coppola, L., Cerulli, T., and Salvioni, D., *Sustainable Development and Durability of Self-Compacting Concretes*. ACI Special Issue, 2004. 221: p. 29-50.

49. Zhu, W. and Gibbs, J.C., *Use of different limestone and chalk powders in self-compacting concrete*. Cement and Concrete Research, 2005. 35(8): p. 1457-1462.
50. Hossain, K.M.A. and Lachemi, M., *Bond behavior of self-consolidating concrete with mineral and chemical admixtures*. Journal of Materials in Civil Engineering, 2008. 20(9): p. 608-616.
51. Valcuende, M. and Parra, C., *Bond behaviour of reinforcement in self-compacting concretes*. Construction and Building Materials, 2009. 23(1): p. 162-170.
52. Cattaneo, S. and Rosati, G., *Bond between Steel and Self-Consolidating Concrete: Experiments and Modeling*. ACI Structural Journal, 2009. 106(4): p. 540-550.
53. Leemann, A. and Hoffmann, C., *Properties of self-compacting and conventional concrete - differences and similarities*. Magazine of Concrete Research, 2005. 57(6): p. 315-319.
54. Sahmaran, M. and Yaman, I.O., *Hybrid fiber reinforced self-compacting concrete with a high-volume coarse fly ash*. Construction and Building Materials, 2007. 21(1): p. 150-156.
55. Gesoglu, M. and Ozbay, E., *Effects of mineral admixtures on fresh and hardened properties of self-compacting concretes: binary, ternary and quaternary systems*. Materials and Structures, 2007. 40(9): p. 923-937.
56. Roziere, E., Granger, S., Turcry, P., and Loukili, A., *Influence of paste volume on shrinkage cracking and fracture properties of self-compacting concrete*. Cement & Concrete Composites, 2007. 29(8): p. 626-636.
57. Rols, S., Ambroise, J., and Pera, J., *Effects of different viscosity agents on the properties of self-leveling concrete*. Cement and Concrete Research, 1999. 29(2): p. 261-266.
58. Turcry, P. and Loukili, A., *Evaluation of plastic shrinkage cracking of self-consolidating concrete*. ACI Materials Journal, 2006. 103(4): p. 272-279.
59. Turcry, P., Loukili, A., Haidar, K., Pijaudier-Cabot, G., and Belarbi, A., *Cracking tendency of self-compacting concrete subjected to restrained shrinkage: Experimental study and modeling*. Journal of Materials in Civil Engineering, 2006. 18(1): p. 46-54.
60. Golaszewski, J., *Influence of Viscosity Enhancing Agent on Rheology and Compressive Strength of Superplasticized Mortars*. Journal of Civil Engineering and Management, 2009. 15(2): p. 181-188.

61. Bouzoubaa, N. and Lachemi, M., *Self-compacting concrete incorporating high volumes of class F fly ash - Preliminary results*. Cement and Concrete Research, 2001. 31(3): p. 413-420.
62. Shi, C.J. and Wu, Y.Z., *Mixture proportioning and properties of self-consolidating lightweight concrete containing glass powder*. ACI Materials Journal, 2005. 102(5): p. 355-363.
63. Turkmen, I. and Kantarci, A., *Effects of expanded perlite aggregate and different curing conditions on the physical and mechanical properties of self-compacting concrete*. Building and Environment, 2007. 42(6): p. 2378-2383.
64. Fernandez-Gomez, J. and Landsberger, G.A., *Evaluation of shrinkage prediction models for self-consolidating concrete*. ACI Materials Journal, 2007. 104(5): p. 464-473.
65. Heirman, G., Vandewalle, L., Van Gemert, D., Boel, V., Audenaert, K., De Schutter, G., Desmet, B., and Vantomme, J., *Time-dependent deformations of limestone powder type self-compacting concrete*. Engineering Structures, 2008. 30(10): p. 2945-2956.
66. Sukumar, B., Nagamani, K., and Raghavan, R.S., *Evaluation of strength at early ages of self-compacting concrete with high volume fly ash*. Construction and Building Materials, 2008. 22(7): p. 1394-1401.
67. Seng, V. and Shima, H., *Creep and Shrinkage of Self-Compacting Concrete with Different Limestone Powder Contents*, in *Second North American Conference on the Design and Use of Self-Consolidating Concrete and the Fourth International RILEM Symposium on Self-Compacting Concrete*. 2005, Hanley-Wood: Addison, Illinois: Chicago, USA. p. 981-987.
68. Collepardi, M.e.a., *Strength, Shrinkage and Creep of SCC and Flowing Concrete*, in *Second North American Conference on the Design and Use of Self-Consolidating Concrete and the Fourth International RILEM Symposium on Self-Compacting Concrete*. 2005, Hanley-Wood: Addison, Illinois: Chicago, USA.
69. Lowke, D. and Schießl, P., *Effect of Powder Content and Viscosity Agents on Creep and Shrinkage of Self-Compacting Concrete*, in *Proc. of the Eighth International Conference on Creep, Shrinkage, and Durability of Concrete and Concrete Structures*. 2008, CRC Press: Ise-Shima, Japan. p. 655-661.
70. Mazzotti, C. and Ceccoli, C., *Creep and Shrinkage of Self Compacting Concrete: Experimental Behavior and Numerical Model*, in *Proc. of the Eighth International Conference on Creep, Shrinkage, and Durability of Concrete and Concrete Structures*. 2008: Ise-Shima, Japan. p. 667-673.

71. Maia, L.M., Nunes, S., and Figueiras, J.A., *Influence of Paste Content on Shrinkage and Creep of SCC*, in *Proc. of the Eighth International Conference on Creep, Shrinkage, and Durability of Concrete and Concrete Structures*. 2008, CRC Press: Ise-Shima, Japan. p. 675-680.
72. Wustholz, T. and Reinhardt, H.W., *Deformation behaviour of self-compacting concrete under tensile loading*. *Materials and Structures*, 2007. 40(9): p. 965-977.
73. Hwang, S.D. and Khayat, K.H., *Durability characteristics of self-consolidating concrete designated for repair applications*. *Materials and Structures*, 2009. 42(1): p. 1-14.
74. Bažant, Z.P., *Prediction of concrete creep effects using age-adjusted effective modulus method*. *American Concrete Institute Journal*, 1972. 69: p. 212-217.
75. Chiorino, M.A., *A Rational Approach to the Analysis of Creep Structural Effects*. J. Gardner and J Weiss eds., *Shrinkage and Creep of Concrete ACI Special Issue*, 2005. 227: p. 107-142.
76. Dilger, W.H. *Methods of Structural Creep Analysis*. in *Creep and Shrinkage in Concrete Structures*. 1982. New York and Chichester: Wiley.
77. Hanson, J.A., *Report No. SP-38 A ten-year study of creep properties of concrete*. 1953, Concrete Laboratory, US Department of Interior, Bureau of Reclamation: Denver
78. Ketton, J.R., *Study of creep in concrete Technical Reports R 333-I, R 333-II, R 333-III*. 1965, US Naval Civil Engineering Laboratory: Port Hueneme
79. Brooks, J.J. and Neville, A.M., *Estimating long-term creep and shrinkage from short-term tests*. *Magazine of Concrete Research*, 1975. 27(90): p. 3–12.
80. Neville, A.M., Dilger, W.H., and Brooks, J.J., *Creep of Plain and Structural Concrete*. 1983, New York, NY, USA: Longman Inc.
81. Gardner, N.J. and Lockman, M.J., *Design provisions for drying shrinkage and creep of normal-strength concrete*. *ACI Materials Journal*, 2001. 98(2): p. 159-167.
82. Suksawang, N. and Nassif, H.H., *Effect of modulus of elasticity on creep prediction of high strength concrete containing pozzolans*. *ACI Special Issue*, 2005. 227(3): p. 261-284.
83. Mehta, P.K. and Monteiro, J.M., *Concrete Microstructure, Properties, and Materials*. Third Edition ed. 2006, New York, NY, USA: McGraw - Hill.

84. Kovler, K., *A new look at the problem of drying creep of concrete under tension*. Journal of Materials in Civil Engineering, 1999. 11(1): p. 84-87.
85. Barpi, F. and Valente, S., *Creep and fracture in concrete: a fractional order rate approach*. Engineering Fracture Mechanics, 2002. 70(5): p. 611-623.
86. Bažant, Z.P. *Asymptotic temporal and spatial scaling of coupled creep, aging diffusion and fracture process*. in *Creep, Shrinkage and Durability Mechanics of Concrete and Other Quasi Brittle Materials*. . 2001. New York, NY: CRC Press
87. Aïtcin, P.C. in *High Performance Concrete*. 1998. New York, NY: E&FN Spon.
88. Bissonnette, B., Pigeon, M., and Vaysburd, A.M., *Tensile Creep of Concrete: Study of Its Sensitivity to Basic Parameters*. ACI Materials Journal, 2007. 104(4): p. 360-368.
89. Tao, Z. and Weizu, Q., *Tensile Creep due to restraining stresses in high-strength concrete at early ages*. Cement and Concrete Research, 2006. 36(3): p. 584-591.
90. Wustholz, T. and Reinhardt, H.W., *Deformation behavior of self-compacting concrete*. Materials and Structures, 2006. 40: p. 965-977.
91. Trtik, P. and Bartos, P., *Nanotechnology and Concrete: What we can utilise from the upcoming technologies?* American Ceramic Society, 2002. Spec. Vol. (Cement and Concrete Trends and Challenges): p. 109-120.
92. Oliver, W.C. and Pharr, G.M., *An improved technique for determining hardness and elastic modulus using load and displacement sensing indentation*. Journal of Materials Research, 1992. 7(6): p. 1564-1583.
93. Klapperich, C., Komvopoulos, K., and Pruitt, L., *Nanomechanical properties of polymers determined from nanoindentation experiments*. Journal of Tribology, 2001. 123: p. 624-631.
94. Odegard, G.M., Gates, T.S., and Herring, H.M., *Characterization of viscoelastic properties of polymeric materials through nanoindentation*. Experimental Mechanics, 2005. 45(2): p. 130-136.
95. Liu, Y.C., Teo, J.W.R., Tung, S.K., and Lam, K.H., *High-temperature creep and hardness of eutectic 80Au/20Sn solder*. Journal of Alloys and Compounds, 2008. 449(1-2): p. 340-343.
96. Al-Haik, M.S., Garmestani, H., Li, D.S., Hussaini, M.Y., Sablin, S.S., Tannenbaum, R., and Dahmen, K., *Nanomechanical Properties of Magnetically Oriented Epoxy*. Journal of Polymer Science Part B: Polymer Physics, 2004. 42(9): p. 1586-1602.

97. Chawla, N., Singh, D.R.P., Shen, Y.-L., Tang, G., and Chawla, K.K., *Journal of Materials Science*. Indentation mechanics and fracture behavior of metal/ceramic nanolaminate composites, 2008. 43: p. 4383-4390.
98. Fischer-Cripps, A.C., *Nanoindentation*. Second Edition ed. 2004, New York, NY: Springer. 260.
99. Reda Taha, M.M., Soliman, E., Sheyka, M., Reinhardt, A., and Al-Haik, M., *Fracture Toughness of Hydrated Cement Paste Using Nanoindentation*, in *7th International Conference on Fracture Mechanics of Concrete and Concrete Structures*. 2010: Jeju, Korea.
100. Reinhardt, A.K., Tehrani, M., Al-Haik, M., and Reda Taha, M.M. *Nano Scale Characterization of Self-Consolidating Concrete*. in *Third North American Conference on the Design and Use of Self-Consolidating Concrete* 2008. Chicago, IL.
101. Ulm, F.J., Vandamme, M., Bobko, C., and Ortega, J.A., *Statistical indentation techniques for hydrated nanocomposites: Concrete, bone, and shale*. *Journal of the American Ceramic Society*, 2007. 90(9): p. 2677-2692.
102. Ulm, F.J., Constantinides, G., and Heukamp, F.H., *Is concrete a poromechanics material? - A multiscale investigation of poroelastic properties*. *Materials and Structures*, 2004. 37(265): p. 43-58.
103. Ulm, F.J., Vandamme, M., Jennings, H.M., Vanzo, J., Bentivegna, M., Krakowiak, K.J., Constantinides, G., Bobko, C.P., and Van Vliet, K.J., *Does microstructure matter for statistical nanoindentation techniques?* *Cement & Concrete Composites*, 2010. 32(1): p. 92-99.
104. Wang, X.H., Jacobsen, S., He, J.Y., Zhang, Z.L., Lee, S.F., and Lein, H.L., *Application of nanoindentation testing to study of the interfacial transition zone in steel fiber reinforced mortar*. *Cement and Concrete Research*, 2009. 39(8): p. 701-715.
105. Wang, X.H., Jacobsen, S., Lee, S.F., He, J.Y., and Zhang, Z.L., *Effect of silica fume, steel fiber and ITZ on the strength and fracture behavior of mortar*. *Materials and Structures*, 2010. 43(1-2): p. 125-139.
106. Sorelli, L., Constantinides, G., Ulm, F.J., and Toutlemonde, F., *The nano-mechanical signature of Ultra High Performance Concrete by statistical nanoindentation techniques*. *Cement and Concrete Research*, 2008. 38(12): p. 1447-1456.

107. Velez, K., Maximilien, S., Damidot, D., Fantozzi, G., and Sorrentino, F., *Determination by nanoindentation of elastic modulus and hardness of pure constituents of Portland cement clinker*. Cement and Concrete Research, 2001. 31(4): p. 555-561.
108. Jennings, H.M., *Colloid model of C-S-H and implications to the problem of creep and shrinkage*. Materials and Structures, 2004. 37: p. 59-70.
109. Constantinides, G. and Ulm, F.J., *The effect of two types of C-S-H on the elasticity of cement-based materials: Results from nanoindentation and micromechanical modeling*. Cement and Concrete Research, 2004. 34(1): p. 67-80.
110. Su, N., Hsu, K.C., and Chai, H.W., *A Simple Mix Design Method for Self-Compacting Concrete*. Cement and Concrete Research, 2001. 31(12): p. 1799-1807.
111. Reinhardt, A.K., Taha, M.M.R., Al-Haik, M., and Tehrani, M. *Experimental and Numerical Investigation of Nanoindentation of Self-Consolidating Concrete*. in *CD Proc. of the 2009 SEM Annual Conference on Experimental and Applied Mechanics 2009*. Albuquerque, NM.
112. Reinhardt, A.K., Adam, I., Al-Haik, M., and Reda Taha, M.M., *Correlating Nano and Macro Creep Compliance of Cementitious Composites*. Journal of Time Dependant Materials Special Publication. Submitted August 2009.
113. Reda Taha, M.M., Al-Haik, M., Adam, I., A. , Tehrani, M., and Reinhardt, A., *Nano Versus Macro Creep Compliance of Concrete*, in *Proc. of the Eighth International Conference on Creep, Shrinkage, and Durability of Concrete and Concrete Structures 2008*, CRC Press Ise-Shima, Japan. p. 229 -235.
114. Pichler, C. and Lackner, R., *Identification of Logarithmic-Type Creep of Calcium-Silicate-Hydrates by Means of Nanoindentation*. Strain, 2009. 45(1): p. 17-25.
115. Cheng, L., Xia, X., Yu, W., Scriven, L.E., and Gerberich, W.W., *Flat-punch indentation of viscoelastic material*. Journal of Polymer Science: Part B: Polymer Physics,, 2000. 38: p. 10-22.
116. Cheng, L., Xia, X., Yu, W., E., S.L., and Gerberich, W.W., *Spherical Indentation of viscoelastic material*. Mechanics of Materials, 2005. 37: p. 213-226.
117. ASTM, *ASTM C33/C33M -08 Standard Specification for Concrete Aggregates 2008*, ASTM International West Conshohocken, PA.
118. ASTM, *ASTM C128 - 07a Standard Test Method for Density, Relative Density (Specific Gravity), and Absorption of Fine Aggregate*. 2007, ASTM International: West Conshohocken, PA.

119. ASTM, *ASTM C29 / C29M - 07 Standard Test Method for Bulk Density ("Unit Weight") and Voids in Aggregate*. 2007, ASTM International West Conshohocken, PA.
120. Okamura, H., Maekawa, K., and Mishima, T., *Performance Based Design for Self-Compacting Structural High-Strength Concrete*. American Concrete Institute Special Publication, 2005. SP-228: p. 13-34.
121. 209, A.C., *Guide for Modeling and Calculating Shrinkage and Creep in Hardened Concrete*. 2008, American Concrete Institute.
122. ASTM, *ASTM C192 / C192M - 07 Standard Practice for Making and Curing Concrete Test Specimens in the Laboratory*. 2007, ASTM International: West Conshohocken, PA.
123. ASTM, *ASTM C39 / C39M - 05e2 Standard Test Method for Compressive Strength of Cylindrical Concrete Specimens*. 2005, ASTM International West Conshohocken, PA.
124. Adam, I. *Effect of Age at Loading on Creep of High Performance Concrete*. in *International Conference on Performance of Construction Material in the New Millenium - A New Era of Building*. 2003. Cairo, Egypt: Elmaarefa Printing House
125. Schindler, A.K., Barnes, R.W., Roberts, J.B., and Rodriguez, S., *Properties of self-consolidating concrete for prestressed members*. ACI Materials Journal, 2007. 104(1): p. 53-61.
126. Kim, J.J. and Reda Taha, M.M. *Robustness to Uncertainty in Modeling Deflection of Reinforced Concrete Structures*. in *Proceedings of the 12th International Colloquium on Structural and Geotechnical Engineering*. 2007. Cairo, Egypt, December.
127. Reda, M.M., Shrive, N.G., and Gillot, J.E., *Microstructural Investigation of an Innovative UHPC Cement and Concrete Research*, 1999. 29: p. 323-329.
128. Lee, E.H. and Radok, J.R.M., *The contact problem of viscoelastic bodies*. Journal of Applied Mechanics, 1960. 27: p. 438-444.
129. Ting, T.C.T., *The contact stresses between a rigid indenter and a viscoelastic half-space*. Journal of Applied Mechanics, 1966(88): p. 845-851.
130. Lu, H., Wang, B., Ma, J., Huang, G., and Viswanathan, H., *Measurement of Creep Compliance of Solid Polymers by Nanoindentation*. Mechanics of Time-dependent Materials, 2003. 7: p. 189-207.

131. Haecker, C.J., Garboczi, E.J., Bullard, J.W., Bohn, R.B., Sun, Z., Shah, S.P., and Voigt, T., *Modeling the linear elastic properties of Portland cement paste*. Cement and Concrete Research, 2005. 35(10): p. 1948-1960.
132. Hertz, H., *On the Contact of Elastic Solids*. J. Reine Angew. Math., 1881. 92: p. 156-171.
133. Kim, J.J., Reda Taha, M.M., and Al-Haik, M., *A probabilistic approach for extracting load-independent reduced modulus from nanoindentation with example application to cementitious composites*. Materials Characterization, 2009. In Review